Manipulation of fluorescence using low energy electron beams for correlative microscopy

Vos, Y.

DOI
10.4233/uuid:0033593a-9d8e-424f-b2ae-c02645a1036c

Publication date
2022

Manipulation of fluorescence using low energy electron beams for correlative microscopy

Manipulation of fluorescence using low energy electron beams for correlative microscopy

Proefschrift

ter verkrijging van de graad van doctor

aan de Technische Universiteit Delft,

op gezag van de Rector Magnificus Prof.dr.ir. T.H.J.J. van der Hagen,

voorzitter van het College voor Promoties,

in het openbaar te verdedigen op donderdag 6 oktober 2022 om 12:30 uur.

door

Yoram Vos

Natuurkundig ingenieur,
Technische Universiteit Delft, Nederland,
geboren te Rotterdam, Nederland.

Dit proefschrift is goedgekeurd door de

promotor: dr.ir. J.P. Hoogenboom
promotor: dr. C.W. Hagen

Samenstelling promotiecommissie:

Rector Magnificus,	voorzitter
Dr.ir. J.P. Hoogenboom,	Technische Universiteit Delft, promotor
Dr. C.W. Hagen,	Technische Universiteit Delft, promotor
Onafhankelijke leden:	
Prof.dr. B. Rieger,	Technische Universiteit Delft
Prof.dr. A.M. Brouwer,	Universiteit van Amsterdam
Prof.dr.ir. S.J. van der Molen,	Universiteit Leiden
Prof.dr. J. Hernando Campos,	Universitat Autònoma de Barcelona
Prof.dr. L.D.A. Siebbeles,	Technische Universiteit Delft

The work in this dissertation was conducted at the Microscopy Instrumentation and Techniques Group, Department of Imaging Physics, Faculty of Applied Sciences, Delft University of Technology.

Printed by: Ridderprint.

Cover design by: Annika Van Den Heuvel and Yoram Vos

Front & Back: Artist impression of evolving fluorescent squares scanned by an electron beam with a perylene molecule in the background.

ISBN 978-94-6384-372-0

An electronic version of this dissertation is available at
`http://repository.tudelft.nl/`.

Would you believe in what you believe in
if you were the only one who believed it?

Kanye West

Contents

Summary

Combining light and electron microscopy in an integrated system allows for the combination of two different sorts of information in an automated fashion. This type of imaging, called integrated correlative light and electron microscopy (CLEM), is used for imaging of biological specimen and allows us to put the biomolecular context provided by fluorescence microscope into the specimen's ultrastructural context provided by the electron microscope. However, while electron microscopy (EM) creates images at nanometre resolution, fluorescence microscopy (FM) is typically limited by the diffraction limit to hundreds of nanometers of resolution. This leads to a significant discrepancy in resolution when combining both image modalities. Thus, the application of CLEM is limited. This is especially the case for integrated CLEM, as the resolution of FM in non-integrated systems can be increased to tens of nanometres using conventional superresolution (SR) techniques. While there are a few reported cases of SR in integrated systems, overall, the techniques are limited due to a limited amount of space for complex excitation techniques, or stringent limits on the blinking of fluorescent molecules used for localization microscopy (LM) imposed by the vacuum of the EM. Finding new ways to make fluorescent molecules blink in a controlled fashion in the vacuum of an electron microscope would resolve all the issues mentioned above.

The goal of this thesis is to manipulate fluorescent molecules using low energy electrons for superresolution microscopy in the vacuum of a scanning electron microscope (SEM). By manipulating these molecules, and understanding the electron-induced effects, a versatile platform for LM could become available. Using low energy electrons of a few electronvolts, the different electron-induced mechanisms induced would become limited and thus more controlled. For all of this to work, a setup suitable for integrated CLEM, with electron energies available down to a few eV needs to be built. Furthermore, the electron-induced mechanisms for fluorescent molecules, and their effects on the fluorescence should then be understood, characterized, and verified as suitable for LM.

In chapter 2, we show how we modified a commercially available platform for integrated microscopy to achieve electron landing energies down to 0 eV, with 0.3 eV energy spread. For this we use a retarding field by applying a negative voltage to the setup's stage. We show by reflecting the electron beam and detecting it with an in-column detector that we can determine the electron beam's landing energy and energy spread. In addition to this, we show that the setup improves the signal acquired for tissue sections optimized for simultaneous correlative microscopy. These tissue sections often have lower signals than samples optimized for one imaging modality only. For in-resin samples especially, this leads to poor EM signal

for tissue sections of 100 nm thick or thinner. Using the negative stage bias we show that these in-resin CLEM samples can be imaged without extremely long dwell times or high beam currents even for ultrathin (50 nm) sections.

We use the setup presented in chapter 2 to study the effect of different electron landing energies down to a few eV on different fluorescent molecules in chapter 3. We find that fluorescent molecules can act as reporters for different electron-molecule reaction mechanisms. We show how electron irradiation of perylene-diimide (PDI), leads to a remarkable recovery in fluorescence after electron irradiation. We monitor this recovery continuously for different electron landing energies down to 0 eV and find based on the strength of the recovery component that electron-attachment to a transient anionic dark state is the main contributor to this process. This transient dark state can be manipulated by depositing the emitters on a conducting substrate, or by using a different dye of which the anionic dark state can be excited using a different excitation wavelength. With Rhodamine B ITC, we show an instantaneous recovery of the electron-induced dark state close to 0 eV landing energies using a short 405 nm excitation. Finally, we also demonstrate the versatility of low-energy electron irradiation by showing a dye that increases in fluorescence after electron irradiation.

Based on the electron-induced dynamics reported in chapter 3, we aim to determine what sort of strategy would be feasible for superresolution microscopy in the vacuum of a SEM. In chapter 4, we assess the resolution and quality of the reconstructed images of different molecular arrangements using simulations and different localization microscopy analysis techniques. We studied how extended photobleaching lifetimes in vacuum could improve easy-to-implement bleaching assisted localization techniques, or how low energy electron induced fluorescence fluctuations could be distinguished using Haar wavelet kernel filters and used to improve the resolution. We find that the latter approach results in both higher resolution and number of correct localizations, even if the photoswitching is switched off and only photobleaching occurs. We also propose new techniques relying on sparsity in each frame using instantaneous photoswitching of electron-induced dark states, or by temporarily switching emitters on with electrons. In general, we find that these approaches lead to a higher resolution of tens of nanometres, but that the current experimentally available photoswitching parameters are insufficient for resolving small molecular arrangements down to tens of nanometres.

The results presented in chapter 4 show promising prospects for superresolution microscopy in the vacuum of a SEM. However, with the setup presented in chapter 2, and the currently experimentally verified photoswitching parameters, resolutions down to tens of nanometeres are still unfeasible. In chapter 5, we show an integrated microscope modified by having a laser and easy to customize excitation and imaging path. The increased laser power should allow for higher accuracy localizations, but also allows for faster image acquisition. By then introducing a photomultiplier tube in the imaging path, we can monitor the electron induced dynamics down to sub-milliseconds timescales. Using the experimental approach presented in chapter

3, we quantify the fluorescence recovery timescales of perylene diimide for electron landing energies ranging from 1000 eV down to 2 eV. We find that the fluorescence recovery can be described with a double exponential behaviour characterized by time constants varying between 5-150 ms and 0.2–2s, respectively. For 2 eV electron landing energy, close to the resonance energy of electron attachment, we find a reduction in the slower exponential recovery term. Potential mechanisms responsible for these observed dynamics and follow-up experiments are then discussed.

With the results presented throughout this thesis we show how low energy electrons could be used to manipulate fluorescent molecules to achieve higher optical resolutions in an integrated light- and electron microscope. While the first steps have been made, considerable effort needs to be made to (i) understand the electron-induced dynamics and optimize fluorescent dyes, and (ii) to perform the electron-induced dynamics on biological specimen. In our outlook chapter, we discuss experimental approaches for these next steps, and other applications of low-energy electrons outside of superresolution microscopy in integrated microscopy.

Samenvatting

De combinatie van licht- en elektronenmicroscopie maakt het mogelijk om twee verschillende soorten informatie te combineren. Deze manier van afbeeldingen maken, genaamd correlatieve licht- en electronenmicroscopie (CLEM), wordt gebruikt om plaatjes te maken van biologische monsters waarbij de biomoleculaire informatie geleverd door fluorescentiemicroscopie wordt aangevuld met informatie over de ultrastructuur door de electronenmicroscoop. Elektronenmicroscopie (EM) kan plaatjes leveren met nanometer resolutie, maar de informatie van fluorescentiemicroscopie is normaliter gelimiteerd tot resoluties van honderden nanometers door de diffractielimiet. Dit zorgt voor een enorm verschil in resolutie wanneer beide plaatjes gecombineerd worden. De toepassing van CLEM is dus beperkt. Dit is met name het geval voor geïntegreerde CLEM, omdat de resolutie van niet geïntegreerde systemen relatief makkelijk verbeterd kan worden door middel van wijd gebruikte superresolutie (SR) technieken. Alhoewel er een aantal voorbeelden zijn van SR in geïntegreerde systemen, wordt het nog steeds niet veel toegepast om meerdere redenen. Dit komt door de beperkte ruimte in de opstelling waardoor het moeilijk is om complexe excitatietechnieken uit te voeren. Ook is het knipperen van fluorescente moleculen nodig voor localisatiemicroscopie (LM) beperkt door het vacuum van de electronenmicroscoop. Alternatieve methoden om fluorescence moleculen gecontroleerd te laten knipperen in een vacuüm zouden deze eerder genoemde problemen kunnen oplossen.

Het doel van dit proefschrift is om fluorescente moleculen te manipuleren met laag-energetische electronen om superresolutie microscopie te kunnen toepassen in het vacuüm van een raster electronenmicroscoop (SEM). Door enerzijds deze moleculen te manipuleren en anderzijds chemische processen veroorzaakt door electronen te begrijpen kan LM mogelijk beschikbaar worden. Wij doen dit door laag energetische elektronen met een energie van een paar electronvolt te gebruiken, waardoor verschillende electron-geïnduceerde processen onbeschikbaar worden. Hiermee zouden wij dus de geïnduceerde processen kunnen controleren. Om deze energieën te bereiken moet er een opstelling gebouwd worden die geschikt is voor geïntegreerde CLEM met electron landingsenergieën tot aan een paar electronvolt. Daarna moeten de electron geïnduceerde processen voor fluorescente moleculen begrepen worden en hun effect op de fluorescentie moet gekarakteriseerd worden. Daarnaast moet bepaald worden of deze processen geschikt zijn voor LM.

In hoofdstuk 2 laten wij zien hoe een commercieel beschikbaar platform voor geïntegreerde CLEM aangepast kan worden om landingsenergieën tot 0 eV met een spreiding van 0.3 eV te bereiken. Hiervoor gebruiken wij een vertragend elektrisch veld dat de electronen afremt door een negatief voltage aan te leggen aan de stage

van de microscoop. Wij laten zien door de electronenbundel te reflecteren en te detecteren met een in-column detector dat de landingsenergieën en energiespreiding bepaald kunnen worden. Ook tonen wij aan dat onze opstelling het signaal van weefselsecties geoptimaliseerd voor simultane correlatieve microscopie kan verbeteren. Dit soort secties hebben typisch een lager signaal dan wanneer ze geoptimaliseerd zouden zijn voor één soort microscopie. Voor in-resin secties betekent dit dat het EM signaal zeer slecht is voor diktes van 100 nm of dunner. Door het negatieve voltage aan te leggen, laten wij zien dat deze CLEM weefsels in beeld gebracht kunnen worden zonder extreem lange scantijden of hogere bundelstromen te gebruiken, zelfs voor 50 nm dikke secties.

Met de opstelling van hoofdstuk 2 bestuderen wij het effect van verschillende electron landingsenergieën tot een paar electronvolt op verschillende soorten fluorescente moleculen in hoofdstuk 3. Wij nemen waar dat fluorescente moleculen als sensor kunnen dienen voor verschillende electron-molecuul interacties. Wij laten zien hoe de fluorescentie van peryleen-diimide reageert op elektronenbestraling door eerst uit te gaan waarna een langdurig herstelproces van de fluorescentie volgt. Door dit gedrag na elektronenbelichting voor verschillende landingsenergieen tot 0eV, continu te monitoren (na de elektronenbelichting voor verschillende landingsenergieën tot 0 eV) en de sterkte van het herstel te bekijken concluderen wij dat een 'electron-attachment' naar een tijdelijke donkere toestand van het anion verantwoordelijk is voor dit proces. Deze tijdelijke donkere toestand kan gemanipuleerd worden door moleculen te deponeren op geleidende oppervlaktes, of door een molecuul te gebruiken waarbij de donkere toestand geëxciteerd kan worden met een andere excitatiegolflengte. Wij tonen een instantaan herstel van de electron geïnduceerde donkere toestand van rhodamine B isothiocyanaat aan door een korte excitatie met 405 nm golflengte. Als laatste demonstreren wij de brede toepassing van deze methodiek door fluorescente moleculen aan te zetten met bestraling van de electronenbundel.

Gebaseerd op de resultaten gepresenteerd in hoofdstuk 3 proberen wij te bepalen wat haalbare methodes zijn voor superresolutie microscopie in het vacuüm van een SEM. In hoofdstuk 4, bepalen wij de resolutie en kwaliteit van door superresolutie gereconstrueerde plaatjes voor verschillende moleculaire structuren door middel van simulaties en verschillende superresolutie methodes. Wij hebben bestudeerd of langere 'fotobleek' tijden in vacuüm de makkelijk te gebruiken 'bleaching assisted localization' techniek kan verbeteren, en of fluctuaties in de fluorescentie door bestraling met laag energetische electronen individuele moleculen kan onderscheiden door middel van Haar wavelet filters. Wij laten zien dat de laatstgenoemde techniek tot een hogere resolutie en een hoger aantal correcte localisaties leidt. Hiernaast stellen wij nieuwe methodes voor om schaarste van emitters te krijgen in camera frames door middel van het instantaan aanschakelen van electron-geïnduceerde donkere toestand, of door middel van het tijdelijk aanschakelen van de emitters. Voor beiden vinden wij dat de resolutie kan schalen tot tientallen nanometers, maar dat de huidige experimenteel beschikbare fluorescente moleculen onvoldoende zijn om dit te behalen.

De resultaten gepresenteerd in hoofdstuk 4 zijn veelbelovend voor superresolutie microscopie in het vacuüm van een SEM. Echter, met de opstelling van hoofdstuk 2, en de huidig geteste fluorescente moleculen, is de resolutie van tientallen nanometers nog niet haalbaar. In hoofdstuk 5 laten we een geïntegreerde microscoop zien die aangepast is voor laserbelichting en met optische paden die makkelijk aanpasbaar zijn. Het hogere laservermogen zou het mogelijk moeten maken voor hogere localisatie accuratesse, maar ook om sneller plaatjes te schieten. Door ook nog eens een fotomultiplicator te gebruiken tonen wij aan dat electron-geïnduceerde processen tot in de sub-milliseconde schaal gevolgd kunnen worden. Met de methodiek van hoofdstuk 3 kwantificeren wij de tijdschalen van het herstel in fluorescentie van perylene diimide voor electron landingsenergieën van 1000 eV tot 2 eV. Wij observeren dat het herstel beschreven kan worden met een dubbele exponent met tijdsconstantes tussen 5-150 ms en 0.2–2 s. Voor 2 eV landinsenergie, dichtbij het resonante punt van electron-attachment, zien wij een daling in de tijdsconstante van de langzame term. Wij bediscussiëren verschillende mechanismen die verantwoordelijk kunnen zijn voor de geobserveerde dynamica en suggereren experimenten om mee op te volgen.

Met de resultaten, gepresenteert in dit proefschrift, laten wij zien hoe laag energetische electronen gebruikt kunnen worden om fluorescente moleculen te manipuleren om zo hogere optische resoluties te behalen in een geïntegreerde licht- en electronenmicroscoop. Alhoewel de eerste stappen zijn gezet moet er nog verder begrip voor de electron geïnduceerde dynamica verkregen worden. Ook moeten fluorescente moleculen geoptimaliseerd worden en de electron geïnduceerde dynamica moet getest worden op biologische monsters. In het outlook hoofdstuk bediscussiëren wij de verschillende experimentele stappenen andere toepassingen van laag energetische electronen in geïntegreerde microscopen buiten geïntegreerde microscopie.

1

Introduction

Microscopy is an essential technique for many areas of science and technology. As it allows us to see things we cannot discern with the naked eye, it has been a driver for scientific discovery since the very first optical lenses were made. Starting with Antoni van Leeuwenhoek, microscopes allowed the observation of living micro-organisms which eventually led to the emergence of the scientific field of microbiology. Ever since then, microscopes and techniques have been further developed to visualize the intriguing world at the smallest length scales. These tools have been indispensable for our current understanding of the processes underlying life and the origin of various diseases.

Fluorescence microscopy (FM) and electron microscopy (EM) are two well-established imaging modalities for inspecting biological specimen. Fluorescence microscopy relies on optically imaging fluorescent molecules that are labelling specific biomolecules in the specimen. Multiple different fluorescent molecules can be used to target different biomolecules at once and can be distinguished based on different excitation and emission wavelengths. This results in multi-colour images where from the expression of fluorescence one can deduce information about the presence and the whereabouts of these biomolecules within the cell. This may give information, about for example the function of a protein and its involvement in different biological processes. While FM is often used, in some cases it provides the wrong type or insufficient information. In those cases, EM could be an alternative.

The main advantage of EM is its superior resolution in comparison to FM. FM uses visible or near-visible light, which typically limits resolution to a few hundreds of nanometres by diffraction. EM instead relies on the interaction of an electron beam with a sample material to retrieve the needed information. The diffraction limit for electrons is well below a nanometre and in practice, EM is limited by aberrations instead of diffraction. In scanning electron microscopy (SEM), a nanometre focused electron beam scans the sample and generates scattered electrons from the sample [1]. Biological specimen are typically cut in thin sections for inspection with EM, where one or multiple of these sections are then completely or partially scanned. In such a section from a biological specimen, staining agents are used to increase differences in the number of scattered electrons and thus create signal and contrast within the cell. These staining agents typically accumulate in membranes or

specific biological organelles. As a result, SEM provides images displaying the ultrastructure of the cell at nanometre resolution. Both imaging methods thus provide different sorts of information: FM provides information about the whereabouts of biological molecules and SEM provides nanometre-resolution information about the ultrastructure [2].

1.1. Integrated light and electron microscopy

By overlaying FM data on top of the SEM information we can gain insight in the locations of biological molecules within the high-resolution ultrastructural context. This is also known as Correlative Light and Electron Microscopy (CLEM). CLEM has been used for mapping connections between synapses while simultaneously providing information on its bio-molecular composition [3–5] and has been used in research of cancer and viral infections. [6, 7]. CLEM can also be used to find a region of interest for high-resolution EM based on intravital observation or live-cell FM [8, 9]. Especially in recent years, interest in and use of CLEM has been increasing rapidly [2].

CLEM is typically conducted by transferring a sample between FM and (S)EM systems. In the past years, integrated microscopes have been developed that combine the two modalities in a single system [10]. Potential benefits of integrated microscopes are that one does not have to relocate a region of interest observed in one microscope in the other and that there is no risk of sample loss or sample contamination during transfer. Moreover, in an integrated FM and SEM as developed at the TU Delft [11], images from both modalities can be overlaid with nanometre-range accuracy in an automated fashion [12]. Such a high overlay accuracy would be particularly beneficial if one wants to locate the biomolecules visualized with FM very precisely within the nanometre-resolution landscape that is obtained with SEM. However, as conventional FM is limited by diffraction, this benefit for pinpointing molecules becomes blurred out by the limited resolution of FM.

1.2. Superresolution imaging for integrated correlative microscopy

The diffraction limit in optical images can be circumvented using superresolution (SR) microscopy. Here, the hundreds of nanometres-resolution can be improved to resolutions of tens of nanometres by using various techniques. We can divide these techniques into two general types. The first type relies on spatially discriminating fluorescent molecules by non-linear excitation techniques. A popular technique here is Structured Illumination Microscopy (SIM), which utilizes non-uniform illumination patterns that feature sinusoidal intensity variations in 1 or more dimensions to increase the resolution ideally by a factor two [13, 14]. Other more complex techniques, such as STED [15], use an additional donut-shaped illumination profile

that depletes part of the fluorescence via stimulated emission and can thus increase the resolution further up to tens of nanometres. The second general type of SR relies on discriminating different fluorescent molecules in time by creating spatial sparsity in the individual time frames. This allows for localizing each molecule's position by fitting the microscope point spread function. These localization microscopy (LM) techniques, such as PALM or STORM [16, 17], rely on induced or stochastic fluctuations in the fluorescence intensity such that different molecules can be resolved at different points in time. To achieve the highest resolution, a substantial number of fluorophores needs to be 'dark' in each time frame such that you only have a sparse amount fluorescing in each image. This means that molecules should spend a long time in a dark state and spend only a small fraction in an 'on'-state. Furthermore, for high-accuracy fitting of the point spread function you need a maximal amount of signal for the particles that are on. [18] In essence this means that fluorophores should have long-lived dark states but have stable fluorescence during the time that they are on to maximize the yield.

Combining SR with CLEM would be very beneficial as the increased resolution of SR partially lifts the imbalance in resolution between FM and EM. Since the sample preparation for EM generally quenches the fluorescence and creates strong background autofluorescence, SR and EM imaging is often performed sequentially. Here, the SR image is acquired first after which the EM sample preparation steps and imaging are performed. [19] When performing these modalities in separate steps and devices, a good overlay is difficult to obtain since the fluorescence signal cannot be retrieved in the SEM or vice versa. Fiducial markers that generate both FM- as well as SEM-signal can be used. [20–26] However, whenever fiducial markers are sparse in a region it may become more difficult to acquire an accurate overlay or the accuracy may depend on the number of fiducials locally present. Rather, a user may want an accurate or consistent overlay anywhere on the specimen. Furthermore, intermediate sample preparation steps such as dehydration may cause distortions in the sample that can give rise to additional inaccuracies in the final overlay [19]. This can be circumvented by preparing the sample for EM before the SR imaging step [2], but this does not solve the dependency on fiducial markers. Integrated microscopes address this issue, as high accuracy overlays can be achieved without the use of any fiducial markers [12].

SR microscopy is nowadays a feasible approach in conventional optical microscopy but is generally not applicable in integrated CLEM. SIM or STED requires complicated optical setups which are difficult to realize in integrated CLEM since it needs to be integrated within a limited space in a SEM. PALM or STORM, require less complicated setups, but are troubled by controlling the long-lived dark states and high signals required for SR FM. These dark states originate from transitions to the triplet state [27] or radical ion states formed through electron transfer with the environment [28, 29]. In conventional FM, these dark states and high signals are obtained putting the sample in a buffer solution. [30–32] However, for integrated CLEM a buffer wouldn't work due to the vacuum requirement of the SEM. Despite this, there have been a few demonstrations of SR microscopy in integrated CLEM

setups. SR FM has been performed on (i) GFP and YFP by cycling water vapour in an environmental SEM such that blinking occurs [33], and (ii) on Alexa 647 in the vacuum of a TEM [34]. Finally, (iii) SRRF, a technique relying on localization based on fluctuations of molecules for non-sparse emitter densities [35], has been used to improve the resolution in an integrated system [36]. Each of these techniques has different disadvantages such as (i) requiring a specific type of (environmental) SEM, (ii) relying on one specific dye or (iii) having both a 60 nm resolution at best and being prone to reconstruction artefacts [37]. Due to these complications, there is still a large interest in alternative superresolution techniques that are more generally applicable in integrated CLEM.

A first approach that has been pursued to obtain higher optical resolution in integrated CLEM was to locally bleach molecules using the focussed electron beam. The nanometre-sized electron probe will bleach molecules in its close vicinity, due to low energy electrons generated by inelastic scattering events that damage the exposed molecules [38, 39]. By tracking the resulting loss in fluorescence as a function of the electron beam scan position, a higher resolution fluorescence image defined by the interaction range of the focused probe can then be reconstructed. Preliminary demonstrations of this technique have indicated a reconstructed resolution of approximately 100 nm might be reached [40]. This technique does not require any additional optical or SEM components and would therefore be an attractive alternative for SR in integrated CLEM. There are however some disadvantages to this technique. First, application of the technique is irreversible, since the induced bleaching results in a permanent loss of fluorescence signal from the sample. Second, the bleaching-induced differences in intensity are tracked by subtracting consecutive fluorescence images. This image subtraction leads to a square root of 2 reduction in the signal-to-noise ratio and will thus cause more molecules to be drowned in background signal. Third, electron irradiation of biological specimen leads to a dose-dependent increase in background luminescence [41], thus giving rise to an increasing background signal during the measurement. Finally, the resolution obtained so far is still lower compared to techniques like (d)STORM. Therefore, alternative superresolution techniques that could be applied in an integrated light and electron microscope might be needed.

Exploiting the interaction of the (focused) electron beam with the fluorescent sample is arguably the most rewarding approach for novel SR FM techniques for integrated microscopy. Alternative electron beam actions other than plain bleaching, such as induced blinking or preferably a switch-on, would then be needed. Most of the reaction products that follow electron beam irradiation are expected to lead to dissociated or non-fluorescent end products. This makes the local bleaching by a focussed electron beam a natural choice for achieving higher optical resolutions yet has the above-mentioned drawbacks. However, our understanding of the different pathways that contribute to this dissociation in-situ in an electron microscope is still limited, especially for electron beam irradiation in the keV range where it creates a cascade of inelastic scattering processes leading to dissociation. If we could better understand and direct the particular reaction pathways that these organic molecules

undergo, inhibits the potential to manipulate the molecules to switch fluorescence on or off. Somewhat analogously to how buffer solutions control temporary dark states by forming radical anions [28, 29], electron irradiation could then perhaps mediate the switching of fluorescent molecules.

1.3. Electron-induced chemistry for integrated localization microscopy

Dissociation products generated by inelastic electron scattering events have been thoroughly studied for molecules in the gas-phase. By studying the reaction end-products as a function of electron energy, three general mechanisms for electron-induced reactions have been found. Each of these intermediates have different dissociation pathways and have distinct dependencies on the energy E of the incoming electron [42–44], namely:

- **Ionization:** the incoming electron ejects an electron from the molecule leaving behind a positively charged ion (E > 7eV). The ionized molecule can dissociate, depending on the stability of the molecular state.
- **Excitation:** the incoming electron excites the molecule. Depending on the energy transferred, the molecule can dissociate into two oppositely charged fragments (E > 10 - 15eV), dissociate by bond breakage (E > 4 - 6eV), or relax to the ground state by photon or phonon emission.
- **Electron attachment (EA):** an incoming electron is captured by the molecule when the electron energy and a molecular energy level match (typically E < 15eV). This is a resonant process and, depending on the stability of the new molecular state, can either result in dissociation of the molecule, detachment of the electron or relaxation by photon emission or energy transfer to the environment to form a stable negative ion.

An alternative approach to understanding electron-molecule reaction mechanisms is to study the behaviour of fluorescent molecules under electron irradiation. Unlike gas-phase experiments, the main objective here would be to observe the intermediate reaction dynamics and identify the potential long-lived reversible intermediates. This is the starting goal of this thesis. By tuning the energy of the incoming electrons to a few eV we then aim to discern between different events based on the mechanisms mentioned above. The generated intermediates could then be further manipulated with electrons, photons, or the sample substrate. In this way, we hope to shed new light on degradation and reaction dynamics that occur under electron irradiation, which could ultimately help us develop a new superresolution imaging toolbox suitable for integrated CLEM that will allow for high-resolution fluorescence imaging in the context of biological ultrastructure.

1

1.4. Outlook

In this thesis, we explore the possibility of manipulating fluorescent molecules with low-energy electrons for superresolution microscopy in integrated microscopy. To achieve this, we study the electron-molecule reaction mechanisms of fluorescent molecules down to a few eV in an integrated microscope. To obtain low-energy electrons inside the integrated microscope, we apply a negative stage bias between the sample and the electron microscope's objective lens. The setup modified for a stage bias implementation and the calibration method for the electron landing energies close to 0 eV is discussed in chapter 2. We use this setup to irradiate different fluorescent molecules at different electron landing energies. In chapter 3 we show, using low-energy electrons, that long-lived transient anions of perylene diimide can be formed with electron attachment and monitored using fluorescence microscopy. In addition, we show that for the dye Rhodamine B ITC we can instantaneously revert the electron induced dark state with 405 nm excitation and that Alexa Fluor 594, a dye commonly used for labelling of biological specimen, partially switches on after electron irradiation. Next, we simulate the possibilities of LM techniques suitable for integrated microscopy in chapter 4. For this we simulate current easy to implement LM techniques, and potential electron induced techniques based on the results found in chapter 3 of this thesis. Finally, chapter 5 discusses a modified laser integrated setup that generates higher amount of fluorescence signal and allows for lifetime characterization fluorescence dynamics down to the sub-millisecond regime.

2

Retarding Field Integrated Fluorescence and Electron Microscope

We present the application of a retarding field between the electron objective lens and sample in an integrated fluorescence and electron microscope. The retarding field enhances signal collection and signal strength in the electron microscope. This is beneficial for samples prepared for integrated fluorescence and electron microscopy as the amount of staining material added to enhance electron microscopy signal is typically lower compared to conventional samples in order to preserve fluorescence. We demonstrate signal enhancement through the applied retarding field for both 80nm post-embedding immuno-labelled sections and 100nm in-resin preserved fluorescence sections. Moreover, we show that tuning the electron landing energy particularly improves imaging conditions for ultrathin (50nm) sections, where optimization of both retarding field and interaction volume contribute to the signal improvement. Finally, we show that our integrated retarding field setup allows landing energies down to a few electronvolts with 0.3eV dispersion, which opens new prospects for assessing electron beam induced damage by in-situ quantification of the observed bleaching of the fluorescence following irradiation.

This chapter has been published as Vos, Yoram, et al. *"Retarding field integrated fluorescence and electron microscope."* Microscopy and Microanalysis **27.1** (2021): 109-120.

2.1. Introduction

Many different forms of hybrid or integrated light and electron microscopes, which combine the strengths of two different types of microscopy into a single apparatus, have been introduced in recent years [10]. The main purpose of these microscopes is to facilitate the process of correlating data obtained with the two modalities [2, 11, 45, 46]. Alternatively, integrated microscopes can be used to enable new microscopy techniques that can circumvent limitations of either of the stand-alone techniques [47, 48]. A third potential use of integrated microscopes, which so far has received only little attention, is to use the integrated light microscope to in-situ monitor sample changes induced by the electron microscope [49, 50].

In many cases, the integration puts restrictions on the capabilities of one of the integrated modalities as compared to a stand-alone system. We have previously presented an integrated system with fluorescence and scanning electron microscopy (SEM) that, in contrast to several integrated modalities, maintains many of the key characteristics of the stand-alone microscopes. These include high-resolution and magnetic immersion SEM, high numerical aperture fluorescence microscopy (FM) [10], flexibility in fluorescence excitation and detection schemes [51–53] including super-resolution [33, 36], a wide choice of EM detectors, and the possibility of using microfluidic enclosures for observing samples in liquid [54]. However, the use of electrostatic immersion, the application of a retarding or deceleration field between electron objective lens and sample, has so far not been demonstrated in an integrated microscope. Nevertheless, as we will detail below, the application of a retarding electrostatic field may have several key advantages, both for integrated correlative light and electron microscopy (CLEM) and for studying electron-matter interactions with in-situ light microscopy.

In SEM, a retarding field may be applied for several reasons. In low energy (<10 keV) microscopy, electron deceleration is particularly useful as it allows for higher resolution imaging relative to when the primary beam is brought to its final energy as it exits the objective lens [55]. For biological specimens, such as 100 nm or thinner tissue sections, this is particularly important as low energies (1-5keV) are typically preferred to optimize the electron interaction volume to the thickness of the sample. Also, the electron landing energy may be tuned to selectively image at a specific depth in the sample, instead of the entire depth of the tissue section [56, 57]. Another advantage of a retarding field is the acceleration of signal electrons towards detectors underneath the objective lens or in the electron column, which may improve signal collection or allow discrimination between different signals [58, 59]. For (integrated) CLEM, this could be particularly beneficial as the EM contrast in samples prepared for CLEM is typically weaker compared to conventional EM sample preparation due to e.g. the lack of on section post-staining or reduced concentrations of osmium in order to preserve fluorescence [2, 60, 61]. Osmium is used as a fixative and staining agent in biological EM, but it also quenches fluorescence [62, 63]. By improving signal collection, a retarding field could thus help improve signal and contrast in CLEM for samples that have been weakly stained in order to preserve fluorescence.

An additional reason why a retarding field integrated microscope may be beneficial relates to a potential new technique for observing and understanding electron-matter interactions. In CLEM, it is well known that electron beam exposure leads to rapid loss, or bleaching, of fluorescence due to destruction of the organic fluorescent molecules. Therefore, in a CLEM experiment, fluorescence microscopy is always conducted prior to electron microscopy investigation. In addition, electron beam irradiation of organic materials leads to cross-linking, which can in turn induce electron dose-dependent fluorescence in the exposed material [64–67]. Monitoring the sample with fluorescence microscopy during electron irradiation could shed more light on the nature and dynamics of these reactions. The bond scission and cross-linking are predominantly caused by the low-energy secondary electrons [44] that are generated because of inelastic scattering of the higher energy primary electrons. Thus, for this purpose it would be beneficial to be able to reduce the impinging electron energy to the few-eV energy range of the secondary electrons, so that the contribution of a particular electron energy range could be directly studied. Alternatively, imaging with an electron beam energy below 100eV could potentially reduce the number of secondary electrons in the sample and thus reduce sample damage.

Here, we report the implementation of an integrated fluorescence and scanning electron microscope with a retarding field for electron landing energies down to a few eV. We solely bias the sample, thus maintaining the capability of performing high numerical aperture, i.e. low working distance, fluorescence microscopy without the need to entirely bias the fluorescence microscope objective lens or microscope chassis. Using a high numerical aperture lens is important as this translates to higher resolution imaging and higher photon collection efficiency. We show the energy calibration of our integrated fluorescence retarding field set-up at few eV energies and provide initial examples of both contrast improvement in integrated CLEM with a retarding field, and the measurement of electron-energy dependent fluorescence bleaching down to a few eV landing energy.

2.2. Materials and Methods

2.2.1. CLEM samples

Rat pancreas tissue from a BB rat was fixed and immunolabeled as described previously [68]. In brief, tissue was fixed in 4% para-formaldehyde and 0.1% glutaraldehyde followed by a postfixation with 1% osmiumtetroxide/1,5% potassiumferrocyanide. The tissue was embedded in EPON (SERVA). Ultrathin (80nm) sections were cut and collected on ITO glass (Optics Balzers). The sections were incubated with guinea pig anti-insulin antibody (Invitrogen lot #SE2381176) followed by a biotinylated donkey anti-guinea pig secondary antibody (Jackson -IR lot # 137834) and finally a streptavidin conjugated Alexa 594 (Jackson-IR lot# 016-580-084). Subsequently the samples were stained with Hoechst 33258 (Sigma Aldrich lot

BCBF4593v).

Human cervical cancer epithelial (HeLa) cells transfected with GFP-C1 were high pressure frozen, freeze substituted and embedded in HM20 resin as previously described (Peddie et al. 2014a). Serial ultrathin sections of 100 nm and 50 nm thicknesses were cut from the polymerized resin blocks using a 45-degree diamond knife (Ultra Jumbo, Diatome) and collected directly on ITO coated coverslips.

2.2.2. CLEM imaging

All FM and EM imaging was conducted with an integrated microscope (Verios SEM FEI, Eindhoven, the Netherlands) equipped with a SECOM fluorescence microscope (Delmic, Delft, the Netherlands) that was modified to apply a retarding field as described in detail in the corresponding section. All further details of the microscope and its various components can also be found in that section.

FM images were acquired prior to EM to prevent bleaching by the electron beam. Hoechst and Alexa images were acquired sequentially using an excitation wavelength of respectively 405 nm and 555 nm, with a 10 s camera exposure time and using a 60x 0.7NA long working distance objective lens (Nikon CFI S Plan Fluor ELWD 60XC).

EM images on rat pancreas samples were acquired in UHR-mode with the circular backscatter detector (CBS) using a current of 0.4 nA, a dwell time of 3 µs and 5 mm working distance. The primary beam energy was varied such that the landing energy was 1.5 keV with the applied bias. The signal on all four segments of the CBS detector was summed. Throughout the images, the gain of the detector was changed to prevent clipping of the EM signal.

EM images on HeLa cells were acquired also in UHR mode with the CBS detector, a current of 0.4 nA, pixel dwell time of 5 µs and working distance of 5 mm, unless explicitly stated otherwise.

In all EM images, the contrast was inverted to resemble TEM-like contrast as is typical for tissue sections in biological SEM.

2.2.3. Fluorescence samples and bleaching experiments

Microscopy cover glass slides (no. 1 thickness) coated with approximately 10 nm of indium tinoxide (ITO) (Optics Balzers AG, Balzers, Liechtenstein) were used as a sample support. The ITO-surface was coated with 6 nm of Al2O3 via atomic layer deposition to prevent quenching of the fluorescence (Moerland et al. 2016). A 60 µM solution of tetraphenoxy-perylene diimide in toluene was then dispensed on the coated glass slide until it was fully covered and spincoated at 2000 rpm to form a homogeneous layer.

The glass slide coated with the fluorescent dye was then fixed onto the sample carrier ring and mounted in the integrated microscope. FM excitation was done using 555 nm excitation wavelength LED source (Omicron Laserage, Rodgau-Dudenhofen, Germany) and a power of 30mW at the sample plane. A brightline Pinkel filterset optimized for DAPI, FITC, TRITC, & Cy5 was used. Imaging was performed with a 250 ms exposure time using a Zyla 4.2 plus sCMOS camera (Oxford Instruments). For EM a 27x27 μm^2 area was scanned with 1 keV primary electron beam energy, 13 pA current and a 1 µs dwell time. The electron beam monochromator was used, and the stage bias was adjusted to perform experiments with landing energies ranging from 1 keV to 5 eV. Each experiment was repeated 9 times per landing energy.

2.3. Results and discussion

2.3.1. The Retarding Field Integrated Microscope

Our main requirements for the retarding field EM setup with integrated fluorescence microscope are: (i) high efficiency photon detection and high optical resolution, (ii) EM-signal detection at landing energies of a few eV to calibrate the landing energy ,(iii) being able to apply high voltages without electric discharge. For the high efficiency photon detection and light microscopy resolution, we wish to use a high numerical aperture air objective close to our sample. For EM-signal detection close to 0eV we require a detector above the sample that can detect high energy reflected electrons or strongly accelerated near 0 eV electrons. Finally, to prevent electric discharge, distances between biased and grounded regions should be sufficiently large to allow maximum field strengths of 5kV/mm.

We base our microscope on a standard commercially available SEM with an integrated fluorescence microscope. This combination is schematically illustrated in Figure 2.1a. The integrated microscope includes an objective lens, which is located below the sample inside the vacuum. High NA objective lenses have working distances in the range of millimeters which can lead to electric discharge between the objective and sample when subject to a strong electric field. Therefore, different objective lenses are used for different voltages. For voltages below -1 kV, we use a 0.95 NA lens whereas for higher voltages of up to -3kV we use a 0.7NA lens. The remaining optics for the excitation (green) and emission (red) pathways are located outside the vacuum of the SEM. The Verios SEM is equipped with an electron monochromator allowing low energy dispersion, which we will illustrate and characterize later. Also, the SEM is equipped with a circular backscatter (CBS) and in-column detector (ICD). The latter allows EM signal detection high up in the electron column, needed for EM-signal detection close to 0eV. As the fields of view of both microscopes overlap, simultaneous fluorescence and electron microscopy simultaneous with EM are made possible.

To implement a negative stage bias, we modify the sample stage of the integrated microscope. A custom-made top plate is mounted to the sample stage as illustrated

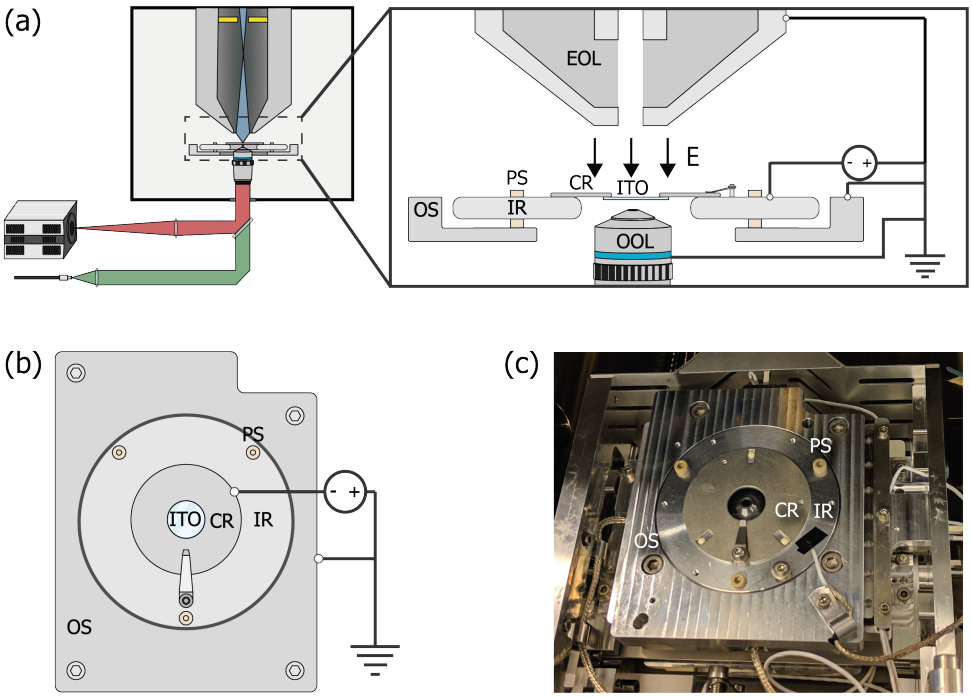

Figure 2.1: (a) Schematic of the integrated light and electron optical microscope. Green and red indicate optical excitation and emission pathways respectively. Blue indicates the trajectories of the primary electrons, the position of the in-column detector is indicated in yellow. Inset shows a schematic view of the sample stage. An inner ring (IR) is electrically insulated from the outer part of the sample stage (OS) by PEEK screws (PS). A negative bias is applied between the sample and electron microscope objective lens (EOL), creating a retarding electric field E. A sample is mounted on an ITO-coated glass slide (ITO), which is fixed, in electrical contact, to a sample carrier ring (CR), which clamped onto the inner ring. An optical objective lens (OOL) allows for photon excitation and detection. (b) Top-down view of the sample stage. (c) Image of the sample stage , showing the location of various components named in b.

in Figures 2.1b and c. This top plate consists of an inner ring that is electrically insulated by PEEK screws from the rest of the stage. This makes it possible to bias the central region of the top plate instead of the entire SEM chassis and makes it safe to handle the door during an applied external high voltage. An external high voltage source (HCN 35-12500) floated by a 300V power source (Delta Elektronica E0300-0.1) is wired to the top plate's inner- and outer region using one of the SEM vacuum feedthroughs. By using a 1:10 voltage divider to measure the applied voltage we can apply negative bias potentials with 0.1 V precision. Conductive ITO-coated glass slides (Optics Balzers) are mounted to a metal ring and clamped to the inner ring of the top plate, thus obtaining the same voltage as the top plate. The fluorescence objective lens images the sample through the central hole in the top plate. Thus, a negative stage bias can be applied while simultaneous optical imaging can be performed with high numerical aperture fluorescence objective lenses.

2.3.2. Electron Landing Energy Calibration

In the previous paragraph, we described how we can set the bias voltage with 0.1 V precision. However, small errors in the voltage divider may lead to deviation of the readout versus the actual set bias. Furthermore, accuracy is not only affected by the precision of our voltage sources. The ripple of the power supply, work function differences between electron source and sample, and energy spread in the electron beam can also affect the final accuracy of the electron landing energy (E_L). For higher landing energies this is not an issue, however for energies close to 0 eV these effects become significant. Therefore, we developed a method to calibrate the actual E_L and the energy spread expected in our measurements. This method is based on the reflection of the electron beam as E_L passes through zero.

For E_L = 0 eV the sample acts like a mirror and electrons are reflected up into the column (fig. 2.2a). The signal from scattered electrons close to 0eV is low, however when all primary electrons are reflected back up into the column, they will hit the ICD. Thus, we expect a steep increase in the signal on the detector when we transition from no reflection to full reflection of the beam. Figure 2.2b shows a series of ICD images taken with a primary beam energy of 1 keV, 25 pA current scanning a bare ITO-glass slide with 3 µs dwell time for different stage bias values. The detector contrast and brightness were set such that neither the reflected nor the background signals were saturated. First, we see a sudden rise in the detector signal starting around -996.2V confirming the reflection of electrons. Second, we see the appearance of several features in the images at different stage bias values, such as a central dark circle in all images, a large gray disk with a surrounding dark background at bias values below electron reflection and a small displaced bright cut-off disk with a barely visible grid-like pattern during electron reflection.

Both the central dark circle and the grid-like pattern are believed to be part of the solid-sate detector. Since the ICD is located inside the electron column, the primary electron beam is required to pass through, which is why we observe the central hole. We believe the grid is part of the solid-state detector possibly used to pull more electrons into the active layer, thus improving the efficiency of the detector. A dark gray disk surrounded by a dark background appears in the images before electron reflection. This is most likely due to electrons scattered from the sample that reach the ICD. Because we used a low magnification, the electron beam gets blocked for larger scanning angles resulting in the observed pattern. This effect can also be observed in a regular SEM without any stage bias involved.

Finally, upon electron reflection we see (i) the dark gray disk disappears in the images and (ii) it is replaced by a bright cut-off disk. This cut-off disk is displaced from the image center and smaller with respect to the dark gray disk it replaced. We attribute the bright cut-off disk to the reflected electrons. Whereas scattered electrons return with various angles to the detector, upon reflection the angle is fixed. Thus, scattered electrons can move in a direction toward the optical axis whereas reflected electrons will always move further from the optical axis than the

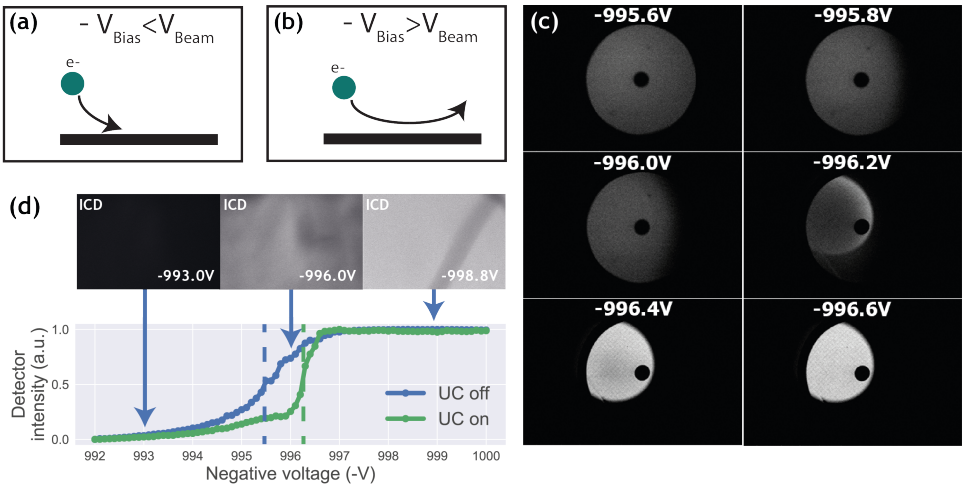

Figure 2.2: (a-b) Illustration of our method to determine the stage potential at which the landing energy equals 0 eV. If $-V_{bias}$ V_{beam} the beam will be reflected upwards causing an increase in signal for the detector high up in the electron column. (c) Images taken with an in-column detector with a 1 keV primary beam energy, electron beam monochromator and varying sample stage bias such that the electron landing energies are close to 0 eV. Starting from -996.2V the detector signal increases caused by primary electron being reflected into the column and consequently hitting the ICD. The central dark spot is the ICD aperture. (d) Average in-column detector intensity for different applied negative stage bias, with and without using the electron beam monochromator (UC). The signal increases from 0 to 1, indicating increasing reflection of the beam when the landing energy passes 0 eV. Arrows indicate the data points corresponding to the depicted images, dashed lines correspond to 50% detector intensity, taken to be $E_L = 0$.

incoming beam. Thus, while all reflected electrons might be blocked from returning in the column at certain beam angles, a fraction of the scattered electrons could still return–explaining the difference in size between the dark gray and the bright cut-off disk. The displacement of the bright disk with respect to the central hole could be due to various reasons. For one, the sample could be slightly tilted, causing the retarding field to be tilted and thus act like a tilted mirror. The location of the detector could also be responsible. The detector is located above the deflection field through which the electrons return. It could be that this deflection field alters the trajectory of returning electrons resulting in a shift. We note that for a full understanding, one would simulate how these electrons pass through the column. However, due to the presence of the deflection field it would become difficult to simulate as well as interpret which electrons will hit the detector where. Moreover, for our purpose of calibrating the electron landing energy, the clear increase in signal intensity locally on the detector when the beam starts to be reflected, serves the purpose as detailed below.

By taking the average intensities of ICD images with a higher magnification and normalizing it to the maximum detector signal, an estimate energy spread in the electron beam can be obtained. We demonstrate this by performing the experiment

with and without the electron beam monochromator (UC). We define the point of reflection (E_L=0eV), where the detector intensity reaches 50% full reflection. Looking at the FW50 of the signal, we extract an energy spread of 1.2 eV (UC off) and 0.3 eV (UC on), respectively. Hence, we are able to determine E_L = 0 eV and extract the expected energy spread in our measurements by reflecting the beam back into the column. We note that electron reflection does not occur at exactly -1 kV bias, but at a slightly lower bias value. This is due to the work function difference between the sample and the Schottky source. The energy spread both with and without UC are higher than expected for a Schottky source which can be for several reasons such as ripple of the power supply and carbon deposition during imaging. Thus, our method is not directly suitable for precisely measuring the beam's energy spread, but is however appropriate for estimating the final energy spread in our measurements.

2.3.3. Signal Enhancement for CLEM Samples

Having established a retarding-field integrated light and electron microscope, we next illustrate its potential benefit in three applications. First, we look at imaging biological tissue sections prepared for both fluorescence and electron microscopy. In Figure 2.3, EM, FM, and the CLEM overlay are shown for 80 nm rat pancreas tissue labeled with Hoechst and Alexa 594 targeting insulin. All EM images are acquired with a 1.5 keV landing energy, while the applied stage bias varies from 0 to -1 kV and the primary beam energy correspondingly from 1.5 to 2.5 kV. All other beam settings such as dwell time and beam current were kept constant. As can be expected, the stage bias does not affect the FM images. However, the implementation of the negative stage bias clearly shows an increase in CBS detector signal. Biological features, such as cell nuclei (stained with Hoechst and visible in blue in the FM images) and insulin granules (labeled with Alexa594 and visible in orange in the FM images) can be discerned in all three EM images (fig. 2.3a,c,e).

Magnified areas of insulin rich regions further illustrate the effect of a stage bias on EM contrast. At a stage bias of 0 V (fig. 2.3b), the granules are nearly indistinguishable from the background. However, by using a stage bias of -500 V (fig. 2.3d) these insulin granules start to appear more clearly in the images. Increasing the bias further to -1 kV (fig. 2.3k,f) shows that the contrast improves even further, making the insulin features crystal clear. To complement information from the visual appearance of the images, we took 10-pixel wide line profiles across insulin granules (fig. 2.3g). In case of a 0 V stage bias, the noise levels are indeed too high to distinguish a feature in the line profile. We see that upon increasing the stage bias, the noise levels are reduced and that features can be recognized in the line profile. It is important to note that the noise levels appear reduced due to lowering the contrast setting of the detector itself to prevent saturation of the signal. Higher signal thus leads to lowering of the contrast and therefore the noise levels seem to be reduced while the signal strength appears to be roughly the same.

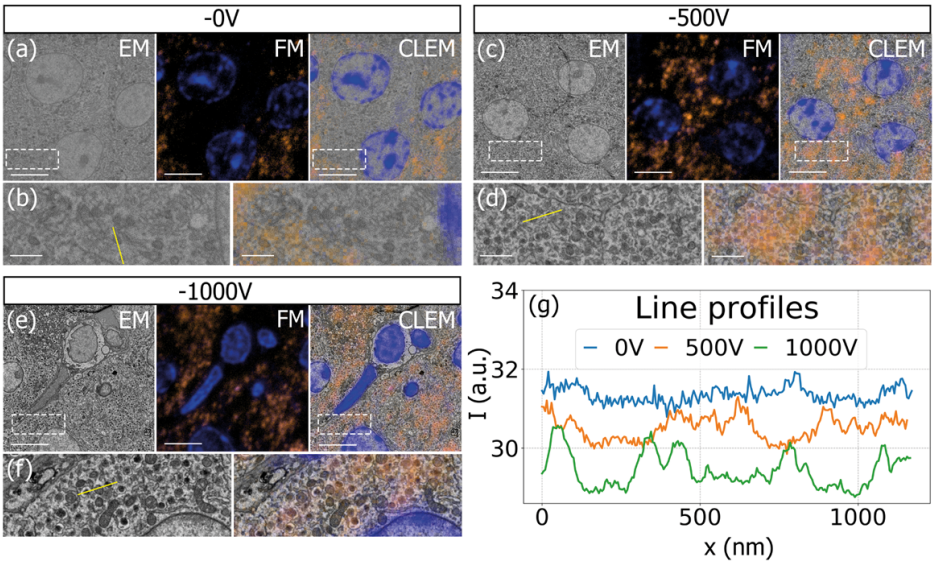

Figure 2.3: EM , FM and correlative images of 80nm rat pancreas tissue with Hoechst (blue) and insulin (orange) labelling for increasing stage bias from 0V (a), -500V (c) and -1000V (e), but with a constant landing energy of 1.5keV. Insets show EM and CLEM (b, d, f) magnified areas of insulin rich regions. 10-pixel wide line profiles (g) were taken across one or multiple insulin granules (indicated by yellow lines in the inset), plotted with an increasing offset of -1.5. Scale bars are 5μm and 1μm for respectively the full-scale images and insets. Increasing the negative stage bias leads to an increase in EM contrast, FM contrast remains the same.

We attribute the improvements in image quality to the acceleration of electrons from the sample to the detector, since the landing energy and thus the electron interaction volume remains constant. This can lead to the visualized improvements in two ways. First, accelerated backscattered electrons hit the solid-state CBS detector with higher energy and can thus generate higher signal per incident electron [69]. Second, the upward acceleration by the stage bias decreases the lateral spread of backscattered electrons, causing more electrons to stay within the solid angle covered by the CBS detector. In both cases the retarding field leads to an increase in detection signal per impinging primary electron and ultimately improves the image quality of EM images.

2.3.4. Improved EM signal for in-resin fluorescence sections

The improvements in signal collection and image contrast for electron microscopy images can be particularly beneficial if a sample preparation protocol is followed that is aimed at preserving fluorescence already present in the sample. In this case, as opposed to the rat pancreas samples used, neither strong fixation with osmium nor the use of relatively high amounts of heavy metals for staining is possible as this

would quench the fluorescence. Also, the procedures for resin embedding need to be modified to prevent full dehydration of the fluorophores, which could also lead to extraction of the hydration shell and a loss of fluorescence. To illustrate, we used a sample of HeLa cells expressing Green Fluorescent Protein (GFP), which were high-pressure frozen and embedded in HM20, following a previously published in-resin fluorescence protocol aimed at preservation of the GFP fluorescence [61, 70] such that even superresolution localization microscopy could still be conducted [33].

After mounting the sample in the integrated microscope, GFP signal from the sample can be clearly identified with the fluorescence microscope (fig. 2.4a,b) at atmospheric pressure, highlighting the position of cells in the section. Recording EM images with the CBS detector with a 1.5 keV landing energy, 30 µs dwell time and the absence of a retarding field as in the example above gives a very weak signal (fig. 2.4c). However, if a retarding field of -1.5 keV is used, again with 1.5 keV landing energy (fig. 2.4d), the image quality is markedly improved. Cell membranes and organelles are now much more easily visible despite a factor six lower dwell time and without any post-processing of the images. We note that the cell membranes appear patchy in the images. This is most likely caused by the cell membranes having heterogenous uranyl acetate staining making fluorescence distribution appear 'patchy'. FM images were obtained before vacuum pump down. Previously, GFP fluorescence was recorded at 200 Pa in an environmental SEM [61], which is not possible in our setup and would also not be advised while simultaneously applying a retarding field. For this reason an automated overlay was not possible, and instead the fluorescence overlay on the -1.5 kV stage bias EM image is done manually (fig. 2.4e,f). The EM images with a retarding field demonstrate, like the pancreas sections, that the signal in the EM images improves by the retarding field. One could even argue that the improvement appears to be stronger compared to the pancreas sections as features of the HeLa cells without a stage bias are hard to distinguish by eye. Based on these results we can conclude that a retarding field improves the EM signal for different types of sample preparation. Hence, the use of a retarding field could provide a way to image samples that under normal circumstances do not generate a sufficient amount of EM signal.

2.3.5. Landing energy optimization for ultrathin sections

The application of a retarding field in a SEM not only allows for improved contrast, but also enables imaging of very thin sections by fine tuning the electron landing energy in the low or sub-keV range. Reducing section thickness is important especially when serial sections are considered for the process of volume reconstruction of a sample—sometimes also referred to as array tomography. The section thickness then directly translates to the resolution in the third (out-of-plane) dimension, which for a correlative experiment is then equal in FM and EM. Using superresolution fluorescence microscopy, lateral FM localization accuracy of 80 nm for the in-resin fluorescence sample described previously has been demonstrated [33] . Decreasing

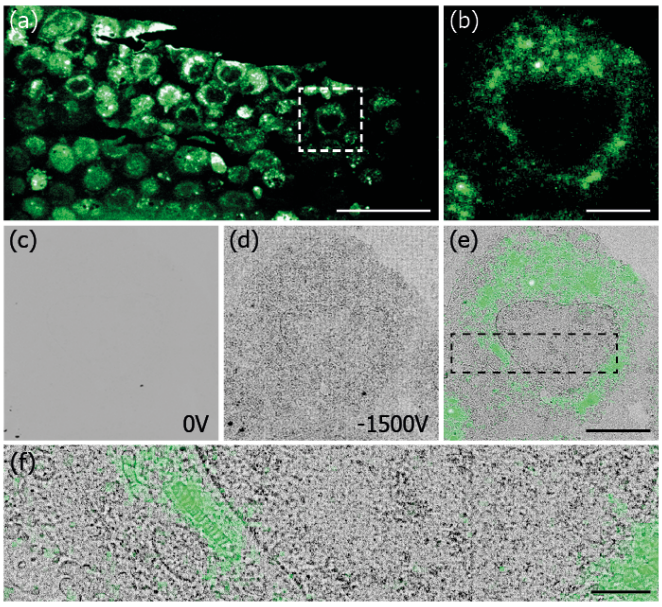

Figure 2.4: Correlative images of in-resin embedded 100nm HeLa cell sections labelled with GFP, (a-b) FM images in ambient conditions. (c-d) EM images using a 1.5keV landing energy and (c) 0V stage bias and 30µs dwell time (d) -1.5kV stage bias and 5µs dwell time. (e-f) Manual correlative overlay. Scale bars: (a) 50 µm, (b-e) 10 µm, (f) 3µm.

section thickness would decrease the amount of fluorophores and thus, increase their sparsity which will ultimately result in a higher FM resolution. Simultaneously, a reduced section thickness will improve the axial resolution. Achieving a 50nm isotropic FM resolution would come close to rivalling the resolution of immunolabelling with primary and secondary antibodies and a gold particle [21]. However, EM imaging of 50nm sections has so far remained a daunting task due to a lack of EM signal even at higher dwell times. Here, we used these 50nm sections of HeLa cells in HM20 to show the benefit of landing energy optimization for very thin sections.

The CBS detector used in each of our CLEM experiments is inserted below the SEM polepiece (fig. 2.5a) and consists of 4 ring segments, which are labelled A through D as indicated in Figure 2.5b. Without a stage bias, these respective ring segments correspond to scattering angles of 163° to 152°, 152° to 140°, 140° to 130° and 130° to 122°. While in the previous results the signal over all four segments was summed, in the following we will use the different rings to distinguish between electron scattering angles and therefore different types of EM signals. To prevent saturation of the signal the detector's brightness was adjusted throughout the images, while the contrast setting remained the same.

The EM signal changes and improves by lowering E_L for the 50 nm sections as

expected. EM images of these sections were taken using a primary beam energy of 3 keV and retarding field strengths of 0 V to -2.5 kV, leading to electron landing energies of 3 keV to 0.5 keV (fig. 2.5c). The EM image at E_L = 3 keV shows numerous effects. First, the EM contrast appears to be weak suggesting the EM signal is weak as well. Second, we recognize features by a bright outline in the image in stark contrast to all results shown so far. Since the penetration depth at 3 keV is expected to be larger than the 50 nm section thickness [59, 71], this could be caused by the electron beam fully penetrating the section combined with strong scattering on the indium tin oxide substrate below. This would effectively give rise to a transmission-like contrast [72]. Finally, we see unidirectional stripes pointing diagonally in the image, most likely these would originate from marks on the diamond knife leading to scratches in the sample that point in the direction of cutting.

Increasing the stage bias to -1 kV, thus lowering E_L to 2 keV, we see that the contrast in the images improves. Yet, both the stripe pattern and the bright appearance of cellular features persist. Further lowering E_L to 1keV reveals a striking change in the EM image as feature contrast in the images now inverts. Finally, at 0.5keV landing energy the stripe pattern also disappears from the images and the image and feature appearance is similar to that observed for the thicker sections in Figure 2.4. Thus, we see that the ability to tune the landing energy to the sub-keV domain drastically improves contrast for ultrathin sections and for detection with the CBS detector also removes the appearance of sectioning artefacts.

We next identify the contribution of the individual segments of the CBS detector to the images for each E_L from Figure 2.5c. Figure 2.5d shows images of the same area for each individual detector ring for E_L ranging from 3 keV to 0.5 keV. For each E_L we can identify different contributions to these detector rings. At E_L=3 keV, we observe an overall weak signal and contrast. Furthermore, we can see that most of the signal is detected on rings B and C. Lowering to E_L = 2 keV causes an overall increase in signal, likely due to acceleration of electrons to the detector. Despite the acceleration of the electrons, causing their lateral spread to be narrowed, we see that most of the signal still appears on rings B and C. At E_L = 1 keV, we can recognize different effects taking place on the different detector segments. First, we see the contrast of the cellular features invert on all segments compared to the images obtained at higher landing energies. However, on both rings A and B, a slight bright outline around these features seems to be present. Second, the striped pattern caused by the cutting-induced surface topography is absent on rings C and D. Finally, for E_L = 0.5 keV, we see that this surface topography is absent on all rings. Furthermore, we see that at this energy most of the signal appears on ring A and B. Thus, the signal has moved radially inwards with respect to E_L = 1 keV. The images of rings C and D consist mostly of noise. Therefore, to reduce the noise in images at E_L = 0.5 keV imaging should be preferably performed only with rings A and B.

Using this information, we can look for optimized conditions for acquiring EM images of the 50nm sections. By varying E_L between 1 keV and 0.5 keV, we found the best setting to be at 0.8 keV. Similar to Figure 2.5d with E_L = 0.5 keV, most of

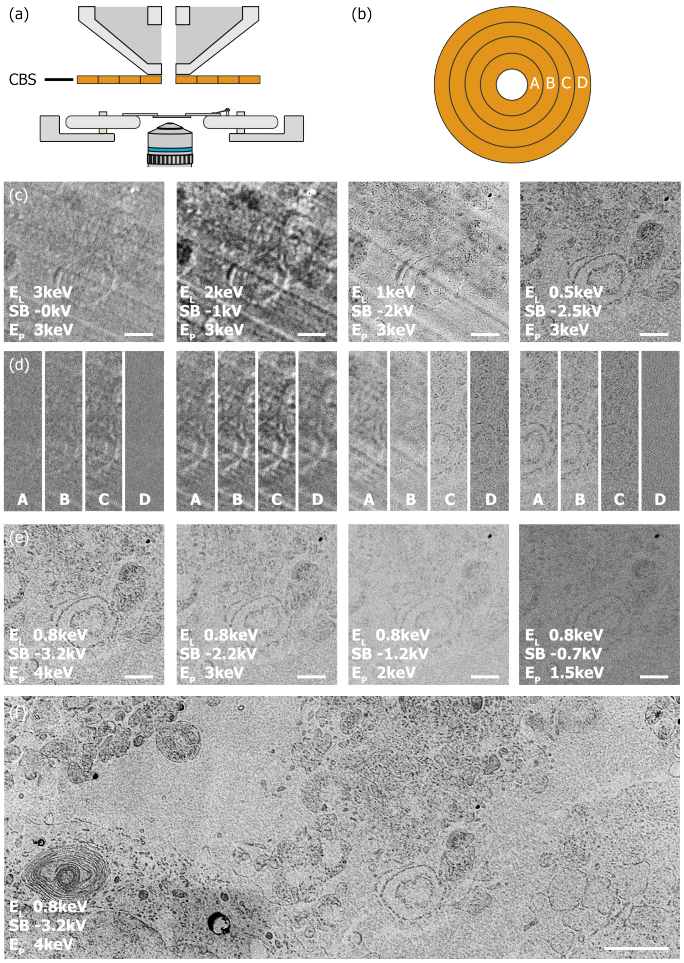

Figure 2.5: (a) Illustration of the insertable CBS-detector located directly below the SEM's polepiece. (b) The CBS consists of 4 rings which allow separate detection per ring, labelled as A, B, C and D. EM images of 50nm sections of HeLa cells were obtained using the CBS detector, a current of 400pA, a 5µs dwell time and various E_P, stage bias (SB) and E_L. (c) EM images with E_P=3keV and E_L ranging from 3keV to 0.5keV. At lower E_L cellular features appear sharper and sample topology disappears. (d) Contributions of the individual CBS rings to the EM images in (c). Lowering E_L creates the possibility to discern between sample topology and cellular features. Furthermore, lowering E_L leads to the signal moving to the central rings. (e) EM images for E_P ranging from 4keV to 1.5keV but constant E_L using CBS ring A&B only. Contrast reduces by reducing SB but features in the image remain unchanged. (f) Large FOV image for E_P=4keV and E_L=0.8keV using ring A&B only. Scale bars are 1 µm in (c-e), 2 µm in (f).

the signal appears on rings A and B, while rings C and D mostly contribute noise. Figure 2.5e shows images obtained at E_L = 0.8 keV with primary beam energy varying from 4 keV to 1.5 keV. At a constant E_L but increasing stage bias we see that the contrast in the images keeps improving. Thus, the optimal setting appears to

be at a primary beam energy of 4 keV with a -3.2 kV stage bias. Figure 2.5f shows the larger area acquisition obtained with these parameters. If we further compare the image series in Figure 2.5e with the other results, we see with constant E_L but different retarding field strength that (i) the type of contrast between features in the image remains the same, and (ii) the striped patterns does not appear even at lower retarding field strength. Thus, the changing visibility of surface topography features and the inversion of contrast of the features of interest in the image are not related to the strength of the retarding field but rather to the landing energy. Therefore, we can conclude that these changes in contrast of the surface topography features are not caused by collimation of either the secondary or backscattered electrons due to the upward acceleration of the retarding field.

Several factors may play a role in the signal dependency on landing energy. First, it should be noted that the sample is highly heterogeneous with a complicated surface morphology. Topographic features, such as the cutting artefacts, are clearly visible in several of the images. In addition, in the composition, stained material alternates with native biological material and a particularly soft embedding polymer, namely acrylic HM20. Besides density differences, this may also give rise to additional height variations at smaller typical length scales than the cutting artefacts. In figure 2.5c, at 2 keV and 1 keV landing energy, contrast inversions around stained features can indeed be observed, pointing to an apparent topography contrast in the images. The landing energy dependence may then come into play via the axial and lateral extent of the interaction volume: if these decrease and become smaller than the typical length scales involved in the surface topography, the topography contrast may disappear from the images, in correspondence with our results. Note that the presence of conductively stained material and insulating polymer may also give rise to a varying electric field distribution. However, we exclude this as a contributing factor to the observed contrast differences as there is only a landing energy and no retarding-field dependency.

Penetration of the primary electron beam through the section material could give rise to contrast inversion, as the strong scattering of electrons on the underlying ITO substrate may give rise to transmission contrast. For landing energies above 2keV, the estimated penetration depth of the electrons would be larger than the on average 50 nm section thickness. For our optimal landing energy, E_L = 0.8 keV, 12 nm would be a reasonable estimate [71]. However, the thickness may vary within the section, e.g. due to the cutting artefacts, and the material density may vary locally, e.g. due to a low polymer filling fraction, and compression of material during cutting. Another factor that could influence the observed contrast inversion when decreasing the landing energy, could be the variation in electron scattering yield going from higher than 1 to lower than 1. This combined with variation of sample composition of stained, biological, and soft polymer material on a microscopic level could lead to an inversion of contrast of certain features. More research, with well-characterized, thin samples, and backed by electron scattering and ray tracing calculations, should be conducted in order to obtain a better understanding of the observed variations in image quality and contrast with landing energy. Lastly,

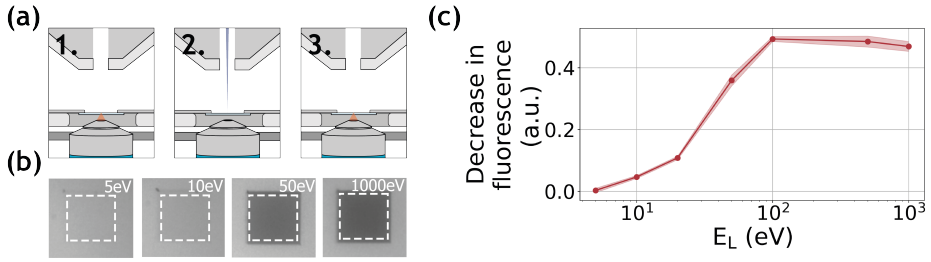

Figure 2.6: (a) Acquisition method for determining electron beam induced damage by fluorescence bleaching. (1) An FM image is taken after which (2) an area of 27x27 µm2 is scanned by the electron beam of a certain landing energy. (3) After scanning an FM image is taken. (b) Resulting final FM images for various electron landing energies. Decreasing the electron landing energy results in a decreasing amount of bleaching. (c) Relative decrease in fluorescence after electron irradiation for landing energies from 1kV to 5eV.

we note that the observations of the segmented detector (Fig. 2.5d) suggest that electrons exiting the sample under a relatively large angle with respect to the surface normal, are least affected by the processes responsible for these variations.

2.3.6. Direct visualization of electron-induced bleaching

As a third example application of our retarding field integrated microscope, we show the direct visualization of electron-induced bleaching of fluorescent molecules. To this end perylene diimide fluorescent molecules are used as a model system. The fluorescent dye is spincoated from a dilute solution to form a homogeneous, thin layer on an alumina-ITO-coated glass slide. The slide is mounted in the integrated microscope and we then monitor the bleaching of the fluorescent dye due to electron irradiation according to the scheme indicated in Figure 2.6a first a FM image is taken, then an area within the FM field of view is scanned with the electron beam, and finally a FM image is taken directly after scanning to record the bleaching induced by the electron beam. We conduct this procedure several times with a fixed dose for different E_L.

A decrease in fluorescence bleaching is observed by reducing the electron landing energy. In Figure 2.6b we show our FM images taken after the electron irradiation for landing energies of 1keV, 50eV, 10eV and 5eV. The irradiated regions can be easily distinguished as these appear darker with respect to non-irradiated regions. This is due to the electron-induced bleaching of the fluorescent molecules, causing the exposed areas to emit less fluorescence. Also, we can see there is a decrease in the bleaching when the landing energy is reduced. This effect is especially pronounced upon going from 50eV to 10eV as the exposed area appears brighter for the latter energy. In Figure 2.6c we show the relative decrease in fluorescence after the electron irradiation for the different landing energies. Each data point is averaged over 9 measurements. Starting with energies ranging from 1keV to 100eV, we see there

is no significant change in the fluorescence bleaching due to electron irradiation. We note that the major contribution to the observed degradation of molecular fluorescence comes from low-energy secondary electrons (SEs). [44] Reducing the electron landing energy from 1keV to 100eV does not alter the molecular degradation processes induced by SEs. However, upon decreasing the landing energy from 100eV to 50eV we see the fluorescence bleaching starts to decrease. In this regime, some molecular degradation pathways induced by SEs may become less accessible. Reducing the landing energy further to 20eV reduces the observed bleaching to only 20%, further to 10% at 10eV and finally only 4% at 5eV. This means that at 5eV the bleaching is 12.5x less compared to beam energies of 100eV to 1keV. To our knowledge this constitutes the first direct visualization of the energy-dependent electron-induced degradation in a film of organic molecules, where in addition we vary the electron energy over orders of magnitude down to only a few eV.

Several effects related to the fact that the primary beam energy approaches and then enters the typical SE energy range can contribute to this decrease. First, when the primary beam energy decreases below 100 eV, the number of generated SEs is reduced and their energy distribution is altered leading to a reduced amount of damage. Second, the penetration depth of the beam changes for different landing energies and is unknown for energies in the range of a few eV [73]. A reduced penetration depth leads to a reduced number of bleached fluorophores as well or, since the dye layer is very thin, the reduced penetration depth could increase the number of events in the dye layer. This would instead give rise to more bleaching at the lower energies. Third, different electron-induced damage processes can occur which may have a different range of energies in which they occur. For instance in organic molecules, direct impact ionization typically halts at about 10eV, while dissociative electron attachment events can occur even when close to 0eV [44]. Thus, when we decrease the electron landing energy from 20 eV down to 10 eV and further to 5 eV, several of these pathways may be gradually switched off, leading to a decrease in the observed damage and thus bleaching. The proposed scheme of using molecular fluorescence to report on the observed damage for specific electron landing energies, may provide a new avenue to study these processes in-situ.

2.4. Outlook and discussion

In this paper we presented a retarding-field integrated microscope, which allows the use of high numerical aperture fluorescence microscopy. The design only requires the user to exchange the top plate of the integrated microscope's sample stage, after which samples can be mounted to a carrier ring and be subjected to a retarding field. The top plate is electrically isolated with the rest of the stage, making the sample stage grounded and thus the entire SEM door as well. Therefore, the SEM is safe to operate during applied biases of several kilovolts. To prevent electric discharge, we limit the bias potential to -1 kV for a 0.95 NA objective lens, while biases up to -3 kV can be achieved via an extra-long working distance 0.7 NA objective. This makes

the stage bias possibilities comparable to setups in other studies used for optimized electron interaction volume and signal collection [58, 59].

Our demonstrated method of detecting reflected electrons up in the column by use of an ICD, a standard asset in a SEM nowadays, allows us to calibrate zero landing energy. This method, combined with a monochromator allows us to detect an energy dispersion of 0.3eV, while still retaining a current in the beam. The energy dispersion here is higher than the dispersion expected from the monochromator. However, other effects such as voltage source ripple and carbon deposition during our image acquisition are expected to increase the measured energy spread further. Thus, our method of calibration does not directly represent the energy spread, but instead is a representation of the expected spread in landing energy during our experiments. More elaborate monochromators are used in TEM, but for SEM, these would require a redesign of the entire microscope. Besides that, using such types of monochromators sacrifices beam current leading to longer acquisition times to achieve the same amount of signal. Furthermore, the measured 0.3 eV energy spread is sufficient for the application examples presented here.

The use of very low energy electrons for imaging has been mostly explored in dedicated microscopes, so-called Low Energy Electron Microscopy (LEEM) [74, 75]. In LEEM the electron beam energy is also reduced by implementing a retarding field between the sample and objective lens. Next, the signal beam is separated from the primary beam by a beam separator and used to reconstruct an image at energies of a few to tens of eV. Due to this beam separator, LEEM setups can be quite complicated. Alternatively, low energy electron microscopy can also be performed in an SEM by tuning the retarding field appropriately. This has been referred to as Scanning LEEM (or SLEEM) [76]. SLEEM does not require the use of a beam separator, making it easier to implement. Our setup with the current detector configuration and landing energy calibration should be able, like SLEEM, to image at these very low energies. We note that such a tool could never obtain the quality of a dedicated LEEM. However, it could be used as a tool for quick inspection of surface properties of materials, as suggested by Mullerova and co-workers [77].

One application example was that the retarding-field bias leads to improved SNR and contrast-to-noise ratio (CNR) in imaging thin biological tissue sections. This is particularly beneficial for CLEM and integrated CLEM as staining and contrasting agents are typically used less in sample preparation to preserve fluorescence [60]. We have mentioned that the retarding field could enhance the signal in two possible ways. Namely, first, by acceleration of electrons to the detector leading to an increase in detected signal per electron, and second, by decreasing the lateral spread of backscattered electrons leading to more electrons hitting the detector. A third possible way in which the signal could be enhanced, but which we did not observe in our experiments, would be via low energy (0 - 20 eV) SEs hitting the CBS detector. For our flat tissue sections, these electrons will only contain information if they are generated by back-scattered electrons on their way out of the sample, and thus a large portion of these only contributes to the background signal. With a stage

bias of a few hundred Volts or more, these secondary electrons will mostly be accelerated straight up into the electron column, through the CBS aperture, leading to a reduction of background in the images. Under different circumstances, such as whole cells, samples with more topography or different SEM configurations, this effect could play a role. Further research, both experimentally and via ray-tracing simulations could be directed at evaluating the stage bias and landing energy for optimal SNR and CNR. This could not only benefit CLEM, but EM on tissue in general and large-scale EM in particular as the latter could allow shorter dwell times for the same SNR/CNR and thus a higher throughput [3, 78, 79].

In our second application example we showed that a retarding field can be used to improve the image quality of very thin sections by reducing the electron landing energy below 1keV while simultaneously increasing the signal on the detector. This can be utilized in serial-section electron microscopy, where going to thinner sections also results in a higher resolution in z of the reconstructed final image. Going to lower electron landing energies leads to a smaller penetration depth of the electron probe and creates the opportunity to measure from shallower surfaces. However, imaging at lower landing energies typically leads to a weak signal. This means that imaging at energies below 1keV landing energies creates images with low contrast. However, we showed that for increasing retarding field strengths the contrast improves. Thus, images at landing energies far below 1keV can be obtained with a sufficiently strong retarding field. This can be used to improve the resolution in z further for deconvolution based subsurface reconstruction algorithms [56, 57]. Typically, EM images at energies between 3keV and 0.8keV are fed to the algorithm through which images have been reconstructed with a z-resolution of 12nm [71]. Lowering E_L further, while still retaining signal using a retarding field creates the potential to image at resolutions of a few nm.

Another application example of the retarding-field integrated microscope was the direct visualization of electron-induced bleaching of fluorescent molecules. By reducing the landing energy below 100eV we have shown that the bleaching of fluorescent molecules also gradually decreases. We mentioned several effects that play a role in this reduction: a reduction in the number of SEs generated at lower beam energy, a changing penetration depth of the electron beam, and relative changes in the population of different electron energy-dependent molecular degradation pathways. Ultimately, at only few eV landing energy, only dissociative electron attachment will be available as a degradation pathways, while all other pathways will be completely switched off. Further research should be directed at distinguishing these different effects so that the observed effects could be quantified in terms of molecular processes. Here, other characteristics of the measured fluorescence could open new possibilities, such as dynamic measurements as well as measuring fluorescence lifetimes or spectral shifts. Such measurements are only possible in an integrated correlative retarding field setup as presented here. This could be particularly interesting for the investigation of electron-molecule interactions where typically only fragmentation products are detected and most of the internal dynamics are obscured. Furthermore, in this field most studies are performed on molecules

in the gas-phase or on clusters [80]. Obtaining information about the processes in organic films or in solid materials could give new insights. Finally, this could also shed more light on the origin of beam damage in the electron microscope and thus lead to novel methods for imaging beam-sensitive materials.

We finally note that the energy range in which we observed reduced bleaching (<100 eV) is still about an order of magnitude smaller than the optimum range found for imaging biological sections (0.8 – 1.5 keV). While imaging under conditions of reduced bleaching could be interesting for correlative microscopy, especially in combination with volume EM, high-resolution imaging at such low electron energies is only possible with a dedicated LEEM instrument as discussed above. Thus, we see the most direct application of this part of our research in the study of electron-induced reactions in organic or solid materials. Ultimately, this could also shed more light on the origin of beam damage in the electron microscope and thus lead to novel methods for imaging beam-sensitive materials such as biological specimen.

2.5. Conclusion

We have presented an integrated fluorescence and scanning electron microscope with the possibility to apply a retarding field between sample and electron objective lens. This allows us to reach electron landing energies of only a few eV with an accuracy of 0.3 eV, which was determined by monitoring the reflection of the electron beam up into the column onto an in-column detector. The retarding field is beneficial for imaging samples prepared for correlative fluorescence and electron microscopy, where it allows significant contrast enhancement for samples that are weakly stained in order to preserve fluorescence. Also, tuning both landing energy and retarding field allows the user to optimize imaging conditions to section thickness which is particularly beneficial for ultrathin sections. We finally presented a first demonstration of how our setup can be used to investigate electron beam induced damage in-situ for electron energies down to a few eV. Further development of this approach may shed light on electron-molecule interactions in the few eV energy regime, the typical range for electrons generated in a sample through inelastic collisions.

3

Fluorescence visualization and manipulation of transient, reversible electron-molecule interactions during electron beam irradiation

Interactions between energetic electrons and organic molecules define the limitations and capabilities in a vast amount of technologically relevant domains including microscopy, lithography, and radiation therapy. Many methods have been developed to evaluate the end products resulting from electron-molecule interactions, but the underlying reaction dynamics and their interplay with the molecular environment have been hard to address. Understanding these dynamics is however essential for directing reaction pathways such that we can ultimately increase resolution and mitigate damage thresholds. Here, we use fluorescent molecules to monitor reactions in-situ using a fluorescence microscope integrated in an electron microscope. We report reversible electron-molecule dynamics occurring over seconds time scale. We control the incoming electron landing energy down to less than 1 electronvolt and show that the amount of reversibility follows characteristic electron energy thresholds described in literature. Using this methodology, we show that the observed reversible dynamics can be attributed to the formation of a dark transient anion followed by environment-mediated neutralization. By then using a fluorescent dye with a near-UV photoexcitable anion we show how photo-stimulation leads to direct reversal of the formed dark transient anions. The versatility of our approach is further demonstrated showing a fluorescent molecule that exhibits electron-induced fluorescence brightening, offering additional prospects for combining electron and superresolution light microscopy. Our strategy thus opens the toolbox of molecular fluorescence spectroscopy, previously instrumental in developing our understanding and use of photon-molecule interaction in science and technology, and enables its application to the comparatively less chartered area of electron-molecule interactions.

3.1. Introduction

Resolution limits in electron and (E)UV microscopy and lithography are defined by structural and chemical damage that occur during irradiation [81–83]. A dominant contributor to the damage mechanisms is formed by low-energy electrons (< 1 keV, mostly 0 – 20 eV) generated in the sample and reacting with organic molecules [84–86]. Also for various forms of radiation therapy, low-energy electron mediated reactions contribute to the selectivity and efficacy of the method [87]. Understanding and visualizing the dynamics of energetic electron-molecule interactions are important steps for directing these reactions towards damage mitigation, resolution enhancement, or biochemical selectivity. Electron-induced molecular damage has been studied under gas phase conditions targeting reaction end products like chemically converted molecules or dissociation fragments. This has revealed phenomena including, electron energy dependent excitation, dissociation, and ionization mediated pathways, but transient dynamics, intermediate species, and especially in-situ interactions with the molecular environment have remained hard to address [42, 44]. Direct observation of electron-molecule transient dynamics in-situ in a sample during irradiation could provide further fundamental insight into reaction dynamics, the involved time-scales, and molecular intermediates, thereby revealing means to manipulate these reactions towards a more desired, damaging or non-damaging outcome.

Here, we use specific, bright and photostable, fluorescent reporter molecules in combination with in-situ fluorescence microscopy during irradiation in an electron microscope to reveal and manipulate reversible electron-molecule reactions and transient dynamics. The fluorescence microscope directly integrated into a scanning electron microscope (SEM) allows continuous excitation of the reporter molecules with visible light and thus measurement of the resulting fluorescence signal (Fig. 3.1A) [11]. At discrete points in time part of the sample is exposed to electrons and fluorescence is monitored before, during, and after this exposure (Fig. 3.1B). Detected temporal changes in the fluorescence signal are then indicative of electron-molecule interactions occurring in the specimen.

Perylenediimides such as N,N'-bis-propyl-1, 6, 7, 12-tetra-(4-tert-butylphenoxy) perylene-3, 4:9, 10-tetracarboxylic diimide (PDI) are well-known, very photo-stable model fluorescent molecules that can serve as both hole and (double) electron acceptors [88]. Both its cation and (di)anion forms do not show fluorescence when exciting at the excitation wavelength of the neutral PDI molecule [89, 90]. Indeed, transient dark states observed in photon-excited single-molecule fluorescence microscopy have been assigned to the presence of charged PDI species formed after tunnelling of the excited electron or hole to or from the direct environment of the PDI molecule [91, 92]. Thus, in our approach, formation of PDI cations or (di)anions due to capture of low-energy electrons or holes generated in the sample during electron irradiation, leads to a decrease or darkening of the fluorescence signal. This darkening may be temporary due to reversibility of the ionization process, or permanent due to either further degradation towards a bleached end product or direct dissociation under

the action of the electron beam.

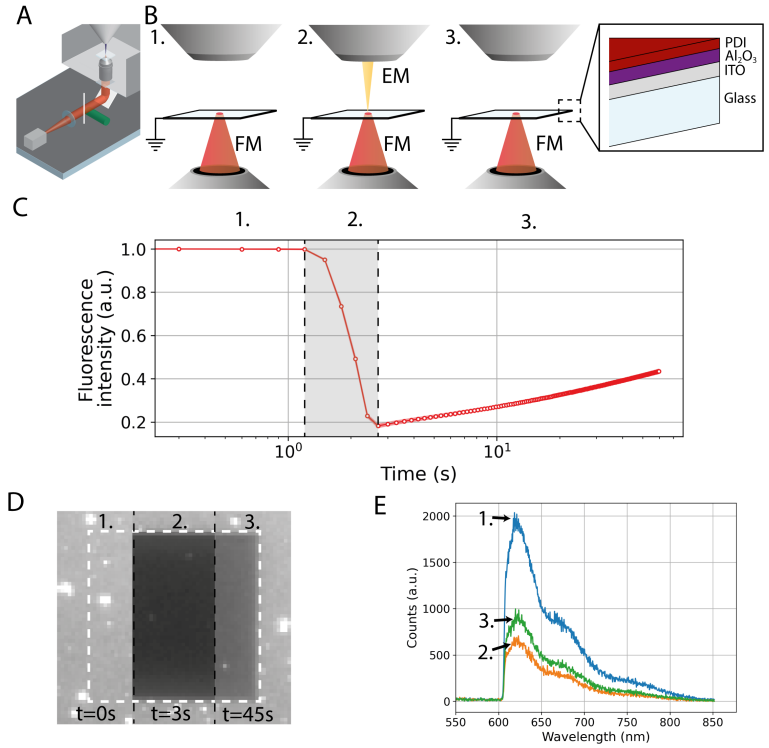

Figure 3.1: In-situ fluorescence imaging during electron irradiation reports on reversibility in electron-molecule reaction kinetics (a) A fluorescence microscope integrated in a scanning electron microscope (b) monitors fluorescence from N,N'-bis-propyl-1,6,7,12-tetra-(4-tert-butylphenoxy)perylene-3,4:9,10-tetracarboxylic diimide (PDI) reporter molecules (1) before, (2) during and (3) after electron irradiation. (b) PDI molecules are spincoated on a microscope cover glass with a 13 nm conductive indium tinoxide layer and a 10 nm dielectric aluminium oxide spacer layer in between. (c) The average fluorescence intensity from the exposed area is tracked in time, showing a clear drop in fluorescence during electron irradiation, followed by a striking, long time scale partial recovery. Grey area indicates the electron exposure duration. (d) Fluorescence images of the exposed area at the start of the measurement (0s), immediately after electron irradiation (3s), and 45s after irradiation. The fluorescence decrease and recovery are uniform over the scanned area of 20x20 μm^2. (e) Fluorescence emission spectra recorded before (blue), directly after (orange), and 113 s after

3.2. In-situ visualization of reversible electron-molecule interactions

To create a poorly conducting sample environment, we first deposit 10 nm of Al_2O_3 on a transparent, conducting ITO-glass slide. We then spincoat a thin layer of tens of nanometres of the PDI molecules on this substrate (Fig. 3.1B). Exposure of this sample with a 1 keV electron beam indeed leads to a marked decrease

in fluorescence signal (Fig. 3.1C). However, over a timescale of tens of seconds after irradiation, we observe a striking recovery of the fluorescence signal. Further inspection of the fluorescence images shows that the darkening and recovery are clearly confined to the exposed area (Fig. 3.1D). Furthermore, no shifts in emission spectra were observed during separate measurements at a lower dose (Fig. 3.1E). This confirms that the partial recovery in fluorescence intensity is related to the molecules switching on again. We attribute this partial recovery of the fluorescence signal to reversibility of the intermediate, charged PDI dark states formed during electron-induced molecular degradation.

3.3. Discerning electron energy dependent pathways

The electron-induced molecular degradation is known to be primarily mediated by low-energy (0 – 20 eV) electrons generated in the irradiated material after inelastic scattering of primary or back-scattered electrons. This degradation can occur via three different types of pathways, characterized by their initial electron-molecule interaction mechanism [44]: (i) ionization, (ii) dissociation by excitation, and (iii) (resonant) electron attachment, each with distinct electron energy-dependent cross sections (Fig. 3.2A). With 1keV irradiation, the primary electrons predominantly scatter in the Al_2O_3, ITO, and glass support layers. Both high-energy elastically scattered and low-energy (secondary) electrons resulting from inelastic collisions in the Al_2O_3 layer escape to the PDI layer if they are generated at a depth shorter than the mean free path. Excitation of the molecule due to inelastic scattering, will result in dissociation into either neutral (>5eV) or polar (>10eV) fragments and thus irreversible bleaching of the excited species. Meanwhile, ionization and electron attachment processes will lead to the formation of non-fluorescent transient PDI (di)an- and/or cations that may be stabilized by interaction with the local, dielectric environment. These transients may further dissociate into permanent non-fluorescent molecules, but exchange of electrons with the environment may also lead to a return to the neutral fluorescent state, evidenced in the partial fluorescence recovery.

We corroborate this picture by assessing fluorescence darkening and recovery throughout the low-energy electron regime, including the typical energy ranges (Fig. 3.2A) associated with each of the three pathways as observed in gas phase experiments. Application of a retarding field to the microscope stage bias in combination with an electron monochromator allows to set the electron landing energy in the few eV regime with 0.3 eV accuracy. The 0 eV reference is obtained by monitoring the intensity of the reflecting beam on an in-column detector [39]. We then observe fluorescence darkening and recovery for all electron energies (Fig. 3.2B, Fig. 3.6), but with key differences in both the relative drop in fluorescence and recovery (Fig. 3.2C, D).

The energy-dependent darkening and recovery reveals four regimes that can be related to the energy dependence of electron-molecule pathways (Fig. 23.2D). Be-

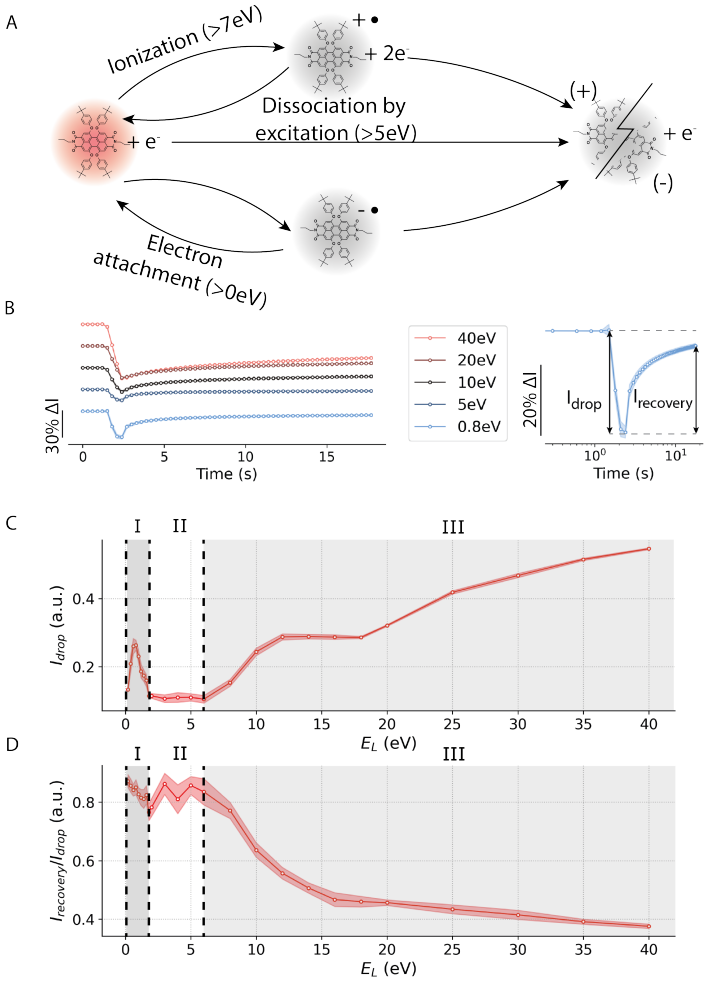

Figure 3.2: Electron energy dependent fluorescence darkening and recovery reveal different electron-molecule interaction regimes. (a) Three distinct pathways for electron-molecule interaction can be distinguished, each with a specific electron energy threshold: ionization (>7 eV), dissociation by excitation (>5 eV) and electron attachment (>0 eV). All three can lead to permanent degradation or bleaching of the fluorescent molecule, but ionization and electron attachment can create an intermediate, reversible, potentially long-lived, non-fluorescent transient ion. (b) Application of an electron monochromator and a retarding field to the specimen stage allows tuning the electron landing energy (E_L) in the low-energy regime. Fluorescence darkening and partial recovery is observed for all landing energies but with striking differences in the relative amount of I_{drop} and $I_{recovery}$ as defined in the right panel. Curves have been shifted vertically for clarity. (c) Both the darkening and (d) recovery show a distinct dependence on electron landing energy reminiscent of the regimes where (I) electron attachment is the only accessible process and exhibits a Feshbach resonance (0 – 2 eV), (II) excitation followed by dissociation into neutrals can occur but has a negligible cross section (2 - 6 eV), (III) ionization pathways gradually become accessible ($\geq$ 7 eV) as will excitation pathways resulting in polar fragments ($\geq$ 10 eV), and interactions are dominated by secondary electrons generated via scattering of the primary electron. Electron attachment is identified as the prime contributor to the fluorescence recovery and thus reversibility in electron-molecule interaction, with about 40% of electron-induced fluorescence darkening being reversible at 40 eV, rising to 80% at sub-5 eV energies.

tween 40 to 16 eV, as we approach lower landing energies in regime III, a decreasing number of secondary electrons generated in the sample decreases the amount of darkening observed, while the recovery only slightly varies. We note that even at 40 eV, 40% of the initial loss of fluorescence recovers, indicating that a considerable amount of generated space charge only dissipates in tens of seconds after irradiation. Later on in regime III (16 - 6 eV), we observe a plateau and then a steep decrease in the darkening, while the recovery steadily increases. We attribute this to irreversible direct ionization pathways and dissociation into polar fragments by excitation that gradually become inaccessible [93–95]. Below 6 eV, the latter pathways no longer contribute, leaving dissociation into neutrals and attachment of inelastically scattered electrons as remaining pathways. This gives rise to a constant minimum in the darkening and a saturation of the recovery in regime II [42, 44]. Finally, between 2 and 0 eV (regime I), we observe a marked peak in the loss of fluorescence, while at the same time recovery also increases. Unlike ionization and neutral dissociation, electron attachment requires specific energies to vacant states in the molecule resulting in the observation of a resonance. This resonance peak and recovering dynamics can also be found for PDI spincoated at lower concentrations (Fig. 3.7). Gas-phase studies for perylene like PDI have shown a peak in the electron-molecule cross-section at 0.7 eV, attributed to anion formation through a long-lived excited Feshbach resonance [96], with the energetic electron exciting the molecule and subsequently being captured. We note that the electron affinity of perylene is worse than for PDI, as PDI bears two imide groups that make the aromatic core more electron deficient and therefore more eager for electrons. This could make the PDI anion more stable, resulting in a longer lifetime of several seconds of the anion. Throughout regime I and II, electron attachment can only occur after energy loss due to scattering and phonon excitation brings the electron energy close to the resonance value. Thus, the overall high degree of recovery in these regimes and the constant minimum in darkening in regime II, indicate electron attachment as the dominant mechanism at the lowest energies and a negligible contribution of neutral dissociation. Furthermore, ionization and excitation into polar fragments appears as the dominant irreversible pathway for molecular damage. We also conclude that in this sample, well over 70% of electron attachment events shows reversibility.

The timescale over which this reversibility and thus recovery of fluorescence take place is determined by the stability of the PDI anion in the sample. On the substrate with the Al_2O_3 top layer, we still observe fluorescence recovery after tens of seconds (Fig. 3.1c, 3.2B). In fluorescence microscopy similarly long-lived PDI dark states have been observed and attributed to electron-tunnelling to and from the environment [91, 92]. In electron scattering, long-lived transient negative ions can be formed via an electron excited Feshbach resonance. The stability of this transient anion may be radically altered on a surface as compared to shorter lifetimes observed in gas phase experiments [42]. We expect these transient dark anions to quickly disappear once a charge transport channel is provided, leading to the absence of the slow recovery and reduced permanent decrease in fluorescence. Indeed, if we replace the insulating substrate and directly spin-coat PDI on conductive ITO, the long-

time scale recovery is lost (Fig. 3.3A, B) and virtually no permanent fluorescence bleaching is observed at electron energies below 7 eV (Fig. 3.3C).

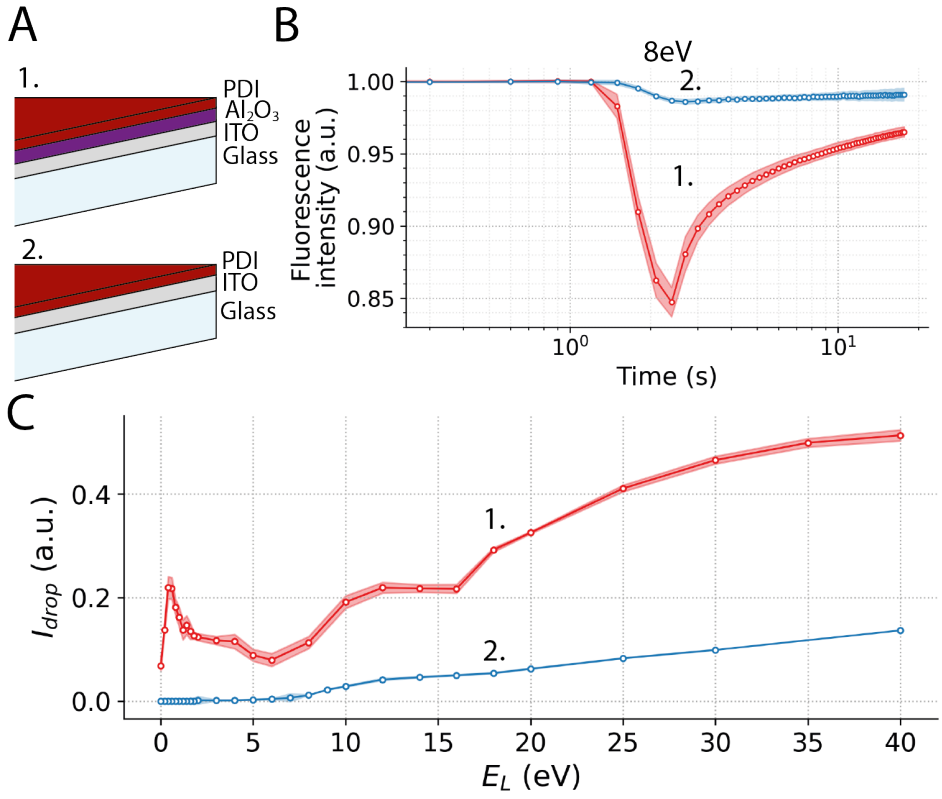

Figure 3.3: Pronounced long time scale dynamics occurs due to transient ion stabilization on an insulating substrate. (a) Comparison of 7 eV electron irradiation of fluorescent PDI spin-coated on conductive ITO versus insulating Al_2O_3 substrate shows that the long time scale recovery is lost on the conducting substrate. (b) For all electron energies, fluorescence bleaching is reduced on ITO as only direct dissociation processes or those faster than electron exchange with the substrate remain. Below the ionization regime (<7 eV), no loss in fluorescence is observed on ITO.

3.4. Manipulation of electron-molecule interactions

The relatively long time scale involved in charge relaxation on the insulating substrate and the chemical nature of the electron-accepting fluorescent molecule provide ways to manipulate the electron-molecule dynamics – e.g., by light irradiation. For this we do not consider the case of PDI whose NIR-absorbing anion is not photoexcitable in our experimental setup [**\cite {wurthner2000highly}**, 97, 98]. Instead, we focus on Rhodamine B isothiocyanate (RITC), a 560 nm excitable molecule with a 405 nm absorption in the anion state [20], we observe a similar decrease and

recovery of fluorescence after electron exposure as for PDI (Fig. 3.4A). In addition, we retrieve the low-energy resonance peak for electron attachment, and the minimum in fluorescence decrease around 5 eV, confirming the formation of an anion. 405 nm excitation of this RITC anion should now allow us to manipulate the electron-molecule dynamics bringing the molecule back to the fluorescent singlet state [99].

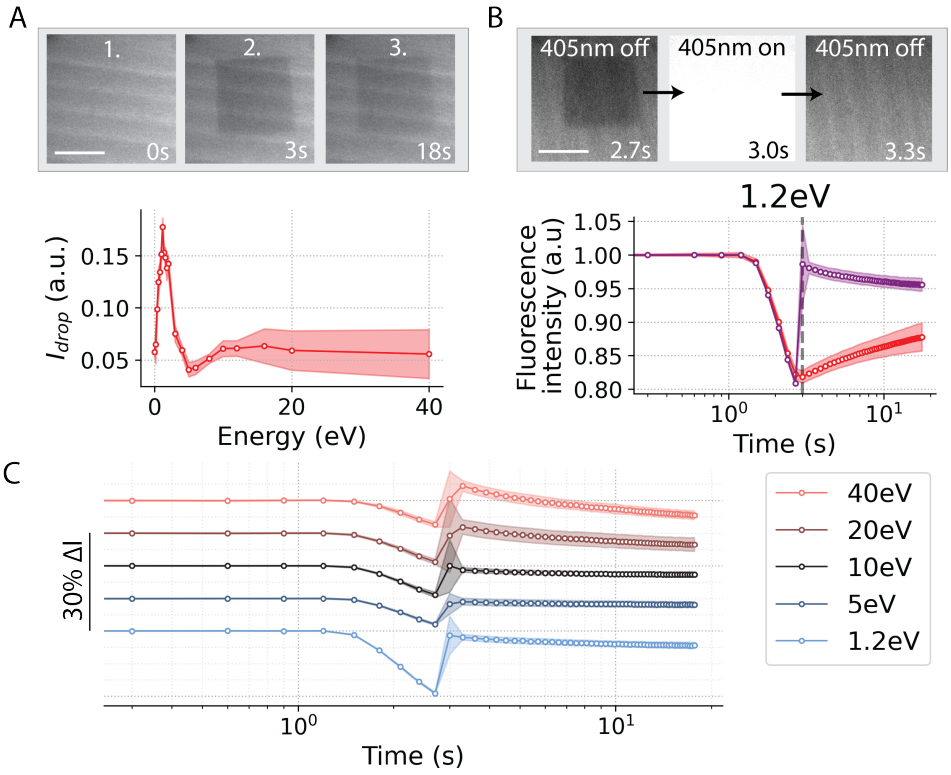

Figure 3.4: Figure 4: Photon excitation of the transient anion formed after electron irradiation accelerates and increases fluorescence recovery. (a) Rhodamine ITC shows similar fluorescence darkening and recovery after electron irradiation as PDI, including a strong electron attachment resonance in the lowest electron energy regime. (b) Optical excitation of the RITC anion with a 405 nm pulse (dashed, grey) after electron irradiation at 1.2 eV leads to an immediate and near-complete recovery of fluorescence (purple). (c) Similar photon-stimulated recovery is observed throughout the 0 – 40 eV energy regime indicating attachment of low-energy electrons after primary electron scattering as the dominant interaction process for RITC. Scale bars: 20 µm

Immediate and nearly complete recovery of fluorescence is indeed observed after excitation with a 405nm pulse (Fig. 3.4B). Thus, excitation of the RITC anion increases the probability for electron transfer to the local environment leading to a return to the RITC fluorescent state and migration of electrons through the sample and substrate. Capture of these electrons by RITC or back-transfer from the Al_2O_3 substrate may cause the gradual decay observed after the stimulated recovery.

Still, over 75% of the initial loss in fluorescence is recovered after 15 s compared to about 30% without the 405 nm photoexcitation, showing how a well-chosen light stimulation can be used to manipulate the course of reactions occurring after electron irradiation (Fig. 3.4C).

Finally, we show that the electron-reporter molecule interaction is not limited solely to darkening. Alexa 594, a sulfonated rhodamine variant that slightly dims in vacuum compared to ambient conditions [100], a remarkable irradiation-induced enhancement of fluorescence (Fig. 3.5A). This enhancement is present throughout the low-energy electron regime (0 – 5 eV; Fig 3.5B) and photobleaches faster than its surroundings during the timeseries (Fig. 3.8). Moreover, spectral measurements confirm that the enhanced signal originates from Alexa594 molecules (Fig. 3.5C). The fluorescence intensity from the exposed area further increases by increasing the electron dose (Fig. 3.8), highlighting the possibilities for an alternative off-on fluorescence reporter scheme that could be exploited in fluorescence microscopy.

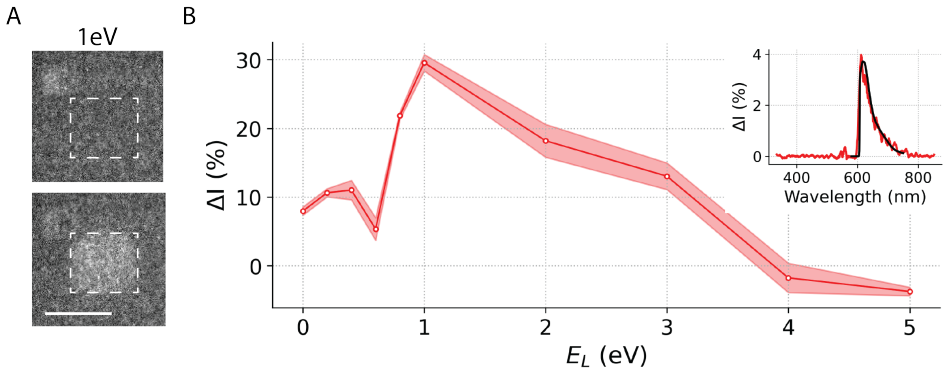

Figure 3.5: Figure 5: Low-energy electron irradiation enhances fluorescence from Alexa Fluor594®. (a) Alexa594, a fluorescent dye commonly used as immuno-label in biophysics, shows enhanced, persistent fluorescence from the exposed area after irradiation. (b) The enhancement is apparent throughout the low-energy electron attachment regime. (Inset) Measured smoothed fluorescence emission spectrum (red) from the exposed area confirms that matches the emission spectrum of Alexa594 in solution

3.5. Conclusion

Fluorescence microscopy has revolutionized our understanding of photon-molecule interactions and excited state dynamics by analysing intensity, lifetime, and spectrum changes in the stream of emitted photons. This has in turn allowed manipulation of excited state dynamics down to the single molecule level, paving the way for superresolution fluorescence microscopy [101]. Our approach opens this fluorescence toolbox to the more uncharted area of energetic electron-molecule interactions providing new windows to study and direct electron beam induced damage. Fluorescent molecules could be embedded in microscopy samples to control or monitor spatial and temporal electron-molecule dynamics or chemical

reaction agents in-situ. Higher excitation power and more sensitive fluorescence detection will give access to higher spatial and temporal resolution, eventually at the single-molecular level.

Reaction and relaxation dynamics can additionally be manipulated with optical stimulation as shown here for RITC. Further schemes may include more complex illumination schemes targeting specific, sequential resonances of (fluorescent) charge acceptors to direct transport in the sample, possibly aided by scavengers or controlled charge carrier accepting gas pulses. Pulsed electron beams in an integrated fluorescence microscope [52], will improve temporal resolution, allow dose rate controlled measurements, or probe after single-electron irradiation.

Our initial observation of fluorescence brightening after electron irradiation makes for even more versatile and sensitive electron-induced degradation probes. Importantly, as Alexa594 is widely used as a biomolecular label in fluorescence microscopy, this also holds thrilling prospects for developing electron-induced fluorescence superresolution schemes in the realm of electron microscopy. Further investigation to the chemical nature of the enhancement process and optimization of dyes towards a larger, or ideally off-on, brightness increase, could allow switching and thus localizing fluorescent molecules with a focused electron beam. Further molecular design, reducing cross sections for direct degradation processes, will thus not only allow single molecule probing of reaction and damage mechanisms under keV focused beams but also pave the way to directly record biomolecular fluorescence probes within electron micrographs with electron beam resolution.

3.6. Acknowledgements

We thank Carel Heerkens for preparation of alumina slides, Ryan Lane for helpful discussions and critically reading our manuscript. This work was financially supported by ECHO grant number 711.016.003 of the Dutch Research Council (NWO). The electron microscopy equipment is further supported by the Netherlands Electron Microscopy Infrastructure (NEMI), project number 184.034.014 of the NWO National Roadmap for Large-Scale Research Infrastructure. J.H. thanks the support from Agencia Estatal de Investigación (PID2019-106171RB-100) and Generalitat de Catalunya (2017 SGR00465).

3.7. Competing interests

Y.V., M.W.H.G., C.W.H, and J.H. declare that they have no competing interests. J.P.H. is a co-founder and shareholder of Delmic B.V., who manufactured the integrated microscope.

3.8. Methods

3.8.1. Samples

Microscopy cover glass slides (no. 1 thickness) coated with approximately 10 nm of indium tin oxide (ITO) (Optics Balzers AG, Balzers, Liechtenstein) were coated with 10 nm of Al_2O_3 via atomic layer deposition, unless stated otherwise. Concentrations ranging from 60 µM to 0.6 µM of tetraphenoxy-perylene diimide in toluene, 2 µM of Rhodamine B isothiocyanate (RITC) in isopropanol (IPA), and 2 µM of Alexa Fluor 594 (AF594) in IPA were used. These concentrations were deposited on the glass slides until it was fully covered and spincoated at 2000 rpm to form a homogeneous layer. Before spincoating, the glass slides were cleaned in an air plasma for 2 minutes at approximately 300mW.

3.8.2. Data acquisition

The prepared glass slides were then fixed to a sample carrier ring and mounted in the electron microscope (Verios SEM Thermo Fischer Scientific, Waltham, Massachusetts, United States) equipped with an integrated SECOM fluorescence microscope (Delmic, Delft, the Netherlands). FM excitation was done using a 555nm excitation wavelength LED source (Omicron Laserage, Rodgau-Dudenhofen, Germany) with a power of 30mW at the sample plane. A brightline Pinkel filterset optimized for DAPI, FITC, TRITC and Cy5 was used for all timetraces. All imaging was performed using a 60x Nikon Plan apochromat air objective and a Zyla 4.2 plus sCMOS camera (Oxford Instruments) using a camera exposure time of 300ms. We used a 4x4 binning for 60 µM and 6 µM of PDI, 8x8 binning for 0.6 µM PDI and no binning for data with RITC and AF594.

The EM was triggered to scan starting at camera frame nr. 5 during acquisitions. A 20x20 μm^2 area of 1024x1024 pixels was scanned using a primary beam energy of 1keV, current of 13pA and dwelltime of 1µs. The electron beam monochromator was used, and a stage bias was applied to the sample using an external high voltage source (HCN 35-12500) floated by a 300V power source (Delta Elektronica E0300-0.1). A detailed description of the stage-bias setup can be found in [39]. Before exposure, the scanned areas were imaged in the FM with a 3s exposure time, and after acquisition of each timeseries a 10 µs dwell electron beam scan was performed, followed by a 3s exposure time camera FM image. After this, we moved 40 µm away from the scanned area and repeated the experiment a total of 9 times. At landing energies below 10eV, we focused the electron beam by minimizing the bleaching spot in FM due to a lack of signal in EM.

Measurements on AF594 were performed by scanning approximately a 10x10 μm^2 area with 10 µs dwelltime, all the other beam settings were kept the same, resulting in a fluence of 8.8 e-/nm^2. Before and after the electron scan, a FM image was taken using 555 nm wavelength excitation and a 1s camera exposure time. We switched

the light source off between those acquisitions to prevent additional photobleaching of the enhanced area, ensuring that the enhanced fluorescence remained stable (Fig. 3.8).

We acquired the PDI spectra separately on a Quanta FEG 200 (SEM Thermo Fischer Scientific, Waltham, Massachusetts, United States) by scanning a 2048x1768 px area using a beam energy of 1 keV, current of 19 pA and dwelltime of 50 ns. We performed optical excitation using a Lumencor Spectra X light engine with an excitation wavelength of 550±15 nm at 1 mW at the sample plane, which was filtered using a 543±10 nm bandpass excitation filter (Thorlabs, Newton, New Jersey, United States). A 40x 0.95 NA Nikon plan apochromat air objective (Nikon, Tokyo, Japan) was used. We filtered the detected emission with a 30/70 beamsplitter (Thorlabs, Newton, New Jersey, United States) followed by a 594 longpass emission filter (Semrock, West Henrietta, New York, United States). The emission spectra were acquired using a PyLoN 100BR eXcelon (TeleDyne Princeton Instruments, Trenton, New Jersey, United States) using an integration time of 300ms. AF594 emission spectra were acquired on the Verios SEM before and after electron irradiation using a 1eV landing energy beam with 25 pA current and by scanning a 4096x3536 px area of 184 µm HFW with 100 µs dwelltime. The light source was switched off during the EM scan.

3.8.3. Data analysis

For the data analysis we first determined the electron-exposed areas from the image series. We typically extracted this region-of-interest by using the images acquired before and after each measurement obtained with a 3s camera exposure time and a 10 µs electron beam dwell time. We subtracted these images for each measurement and summed the resulting subtracted images across all measurement per landing energy. This was not the case for the measurements on 60 µM PDI and RITC without 405nm illumination. Here, we averaged images across the acquired image series before (i.e. until frame nr. 5) and after electron exposure (i.e. after frame nr. 9). These averaged images were then subtracted from each other. This process was repeated for all image series per landing energy after which the resulting subtracted images were added together to a final difference image. As a next step we extract the electron exposed regions from these final difference images. We detect the edges using a canny-edge filter (scikit image), followed by a binary dilation step and a binary fill holes algorithm (scipy ndimage) to close most structures. A final erosion step was then used to remove all non-closed structures. The resulting binary images were then stored locally as a .tif file and used as a mask in the following calculations. In the exceptional case when our algorithm failed, we chose the mask manually.

The reported fluorescence intensity per frame of the measured image series was determined by performing the following steps: (i) calculating the average pixel intensity of the electron-exposed region, (ii) subtracting the background offset, (iii) normalizing the intensity to the intensity in the frames before electron exposure, and

(iv) correcting for photobleaching. For calculating the average pixel intensity of the electron-exposed region in each image we used the masks described in the previous paragraph. Per landing energy, the average intensity of the exposed area per frame was averaged across all 9 measurements. We subtracted background contributions by subtracting pixel values of 300 counts for no binning, 3000 counts for a binning of 4 and 6000 counts for a binning of 8. These background values were estimated based on the saturation value in average intensity when exposing the sample with a high dose and landing energy. After background subtraction we normalized the average pixel intensity per frame by normalizing it to the maximum average pixel value in the first 5 frames. The resulting averaged and normalized pixel intensity per frame then still need to be corrected for photobleaching. To determine the photobleaching of the sample we calculate, perform background correction, and normalize pixel values outside of the electron exposed areas similar as stated above. For most measurements we determined the average intensity of the non-exposed area by averaging across a square edge of 10 pixels wide and 10 pixels displaced from the original mask in x and y. For RITC and AF594 we used the inverse of the mask, i.e. the entire image with exception of the exposed area. The photobleaching occurring during the measurements is then corrected by dividing the average normalized pixel intensity per frame of the electron exposed area with the average normalized pixel intensity per frame of the area analyzed for photobleaching.

We used the average normalized intensity value per frame described in the previous paragraph to determine both the loss in fluorescence signal immediately after electron irradiation (I_{drop}), and the relative fluorescence recovery ($I_{recovery}$). For determining I_{drop} we subtracted the average intensity value at frame nr. 9 for PDI and frame nr. 10 for RITC from the initial average intensity before electron irradiation. The relative recovery in fluorescence was calculated by determining the difference between frame nr. 9 or nr. 10 and the final frame (approximately 15s after electron irradiation). This was then normalized by I_{drop}. For AF594, the relative increase in fluorescence signal was determined by dividing the average fluorescence signal after electron irradiation with the average fluorescence signal before electron irradiation.

The reported errors were determined by calculating the standard deviation of the average pixel intensity values per frame across the 9 different measurements per landing energy. The errors for the photobleaching timetraces were acquired similarly. The total error for the normalized average pixel intensities that were corrected for photobleaching were then calculated as:

$$\sigma = \frac{I}{I_{photobleaching}} \cdot \sqrt{\sigma^2_{intensity} + \sigma^2_{photobleaching}} \tag{3.1}$$

Where I and $I_{photobleaching}$ denote the average pixel intensity per frame of the electron exposed area and of the area used to determine the photobleaching rate. The errors in I_{drop} equal the error of the photobleaching corrected intensities at frame nr. 9 for

PDI and nr. 10 for RITC. The errors in $I_{recovery}$ were calculated by taking the square root of the error in I_{drop} and the error of the average photobleaching corrected intensity in the final frame. This was then multiplied with $I_{recovery}$ to obtain the error in $I_{recovery}$. The errors in the average increased fluorescence intensity of AF594 were determined by calculating the standard deviation between the relative average intensity values across the 9 measurements per landing energy after electron irradiation.

The code used for data-analysis can be found at:
`https://github.com/hoogenboom-group/Vos-electron-dynamics-2021`.

3.9. Additional data

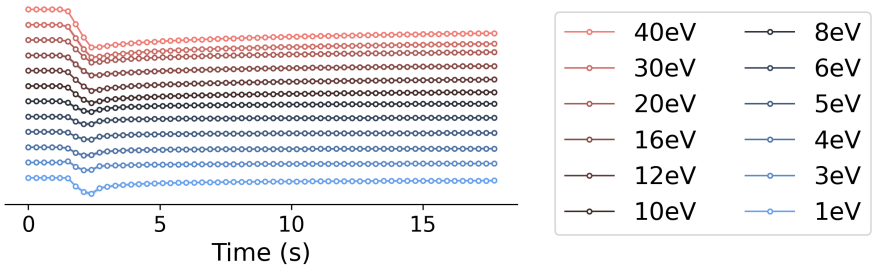

Figure 3.6: The average fluorescence intensity of PDI on a 10 nm thick alumina top layer tracked in time for landing energies ranging from 40 to 1 eV. In all cases, the intensity shows the same trend. An initial decrease in fluorescence caused by scanning the electron beam, followed by a recovery in intensity. The strength of both the initial darkening and recovery show a strong dependence on the landing energy of the electron beam. Curves have been shifted for clarity.

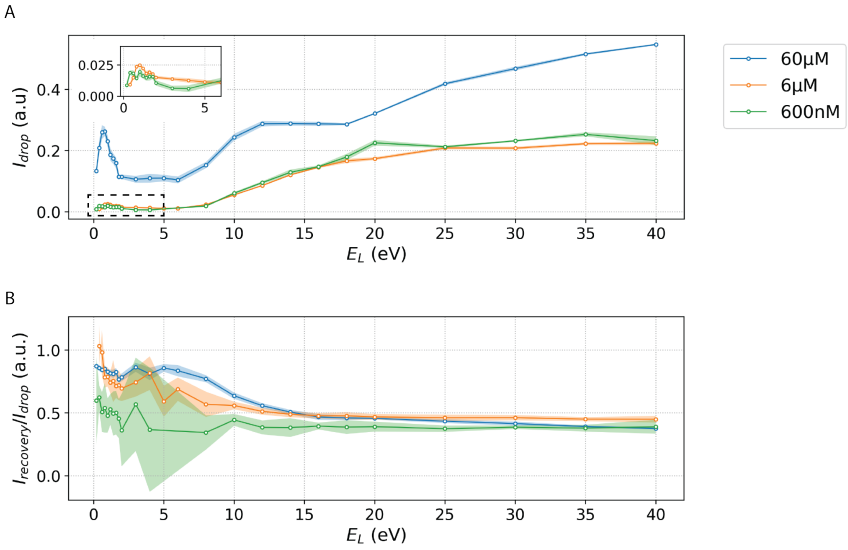

Figure 3.7: PDI shows similar dynamics and energy dependence for lower spincoated concentrations. (a) The average decrease followed after electron irradiation shows a similar trend for all concentrations. The main difference being the general strength of Idrop, the absence of the plateau around 18eV for both 6 µM and 600 nM and (inset) the weaker electron attachment peak around 1eV at lower concentrations. (b) The recovered amount in fluorescence shows a similar strength for all landing energies, however due to a decreasing amount of signal the standard deviations increase. This is especially noticeable for the 600 nm curve between 5 and 2eV.

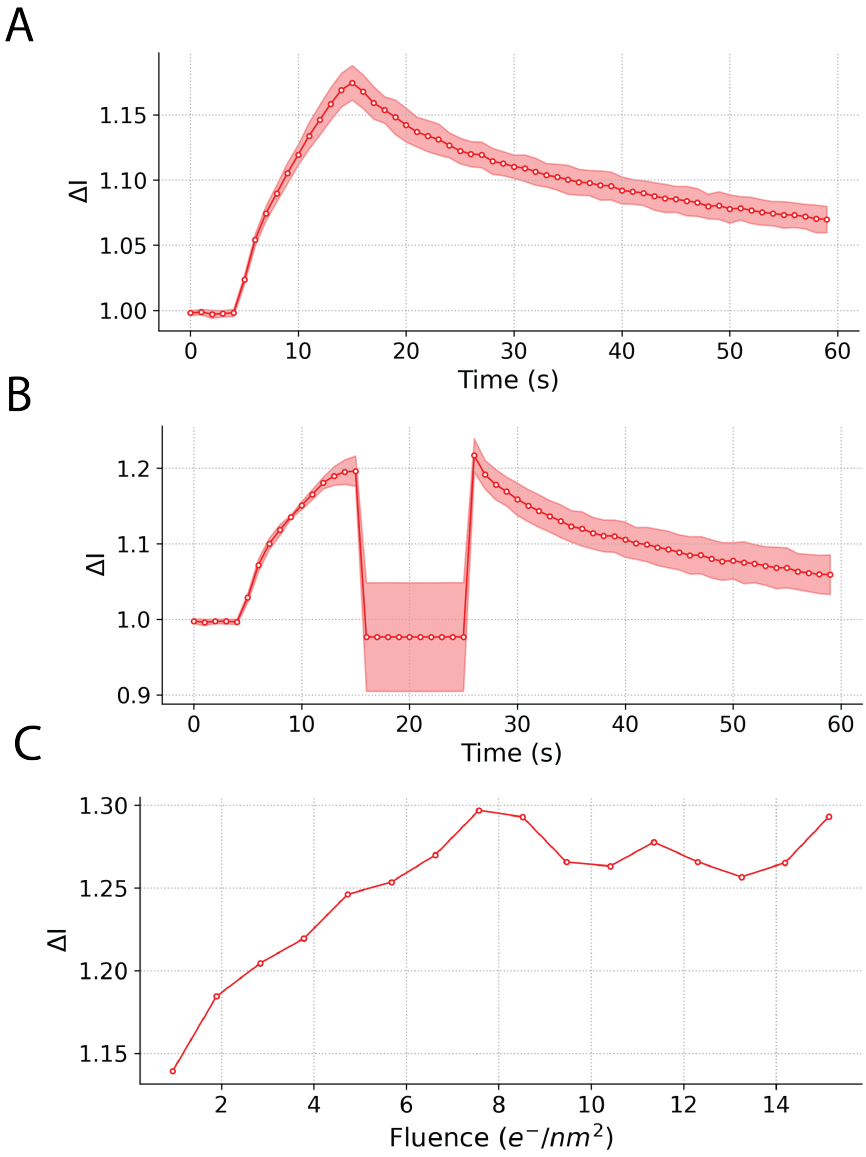

Figure 3.8: AF594 enhanced intensity remains stable when not illuminated and increases with dose. (a) Average fluorescence intensity of AF594 as a function of time. Electron irradiation at 1eV landing energy starts at 4s with a fluence of 35 e-/nm^2. The fluorescence of the exposed area increases until the scan is finished, after which the brightened area slowly loses intensity with respect to the non-exposed area. When the light source is switched off for 10s (b) the increase in fluorescence remains stable until the light source is switched on again. (C) Relative increase in fluorescence for AF594 for increasing dose at 1eV landing energy, the increase in fluorescence stabilizes

4

Superresolution approaches for integrated correlative superresolution microscopy

Correlative light and electron microscopy (CLEM) is able to combine the strength of both image modalities to visualize fluorescently labeled molecules in a detailed high-resolution ultrastructure. Integrating both modalities into a single device eases correlating both images, but is limited in optical resolution due to the limited availability of superresolution (SR) microscopy techniques for integrated setups. Recently, it has been shown that some fluorophores have enhanced photobleaching lifetimes and blinking dynamics, or show temporal intensity fluctuations after low-energy electron irradiation. Here, we explore potential SR schemes suitable for integrated CLEM systems based on these findings using simulations for different molecular arrangements. We study how enhanced photobleaching lifetimes could improve easy-to-implement bleaching-assisted localization techniques, or how low energy electron induced fluorescence fluctuations could improve the final fluorescence image resolution using Haar wavelet kernel analysis. We find that the latter, even when only photobleaching occurs, has a higher final reconstructed image quality due to a higher number of localizations. We also propose and simulate single-molecule localization techniques using instantaneous photoswitching of electron-induced dark states, or by temporary switching emitters on with electrons. Both techniques show improved localization accuracy compared to the bleaching-assisted and fluorescence fluctuation techniques, but also require further optimization of currently available fluorescent dyes to ensure that small molecular arrangements can be resolved with fluorescence microscopy.

4.1. Introduction

Correlative light and electron microscopy (CLEM) combines the strengths of both types of microscopies, for instance to visualize the positions of fluorescently labeled molecules in the context of the detailed sample structure obtained via electron microscopy (EM) refs e.g. de Boer Nat Methods and other CLEM overviews. While CLEM can be performed by shuttling a sample between the different microscopes, integrated correlative microscopy [10] can be an asset for correlative microscopy thanks to the ease with which correlative images can be obtained [11, 45] and the consistent, high overlay accuracy that can be obtained [12]. The latter would be particularly beneficial when the resolution gap between fluorescence microscopy (FM) and EM is bridged by correlating superresolution (SR) fluorescence microscopy to EM, as overlay or registration errors compromise the accuracy of localization with respect to the structural detail. However, SR techniques typically require specific properties of the fluorescent molecules, such as high photon yield, optimized photo-blinking and –bleaching, and photo-activation, which may be hard to preserve during sample preparation for integrated CLEM or in the EM vacuum.

Few groups have nevertheless managed to implement SR FM in integrated microscopy. Peddie et al. have demonstrated integrated stochastic optical reconstruction microscopy (STORM) using green and yellow fluorescent protein (GFP / YFP), where the reduced photon yield and photo-blinking frequency of GFP and YFP in vacuum was circumvented [33] by cycling water vapor in an environmental SEM. They achieved 50 nm fluorescence localization accuracy within the EM structural images. Others have demonstrated localization microscopy using regular fluorescent molecules that sustain blinking in vacuum [34, 36]. Exploitation of the specific conditions in integrated CLEM, i.e. the altered fluorescence properties of molecules in vacuum and the presence of an electron beam, for achieving SR localization microscopy, has so far not been addressed. Nevertheless, Srinivasa Raja et al. have recently demonstrated that some fluorescent molecules show enhanced photobleaching lifetimes in vacuum with respect to ambient conditions [100] and Vos et al. have even shown that temporal intensity fluctuations can be induced using low-energy electron irradiation (Chapter 3). An intriguing open question is thus whether these phenomena allow for new, possibly improved or more generally applicable, possibilities to implement localization microscopy in integrated CLEM.

Besides STORM, many alternative schemes and/or algorithms have been developed to retrieve SR molecular localizations from temporal intensity fluctuations observed in wide-field fluorescence time series. These include bleaching/blinking-assisted localization microscopy (BaLM) [102], superresolution optical fluctuation imaging (SOFI) [103], Bayesian analysis of bleaching and blinking (3B) [104], superresolution radial fluctuations (SRRF) [35] and Haar wavelet kernel (HAWK) analysis with multi-emitter fitting [37]. In general, the difference between these techniques and STORM is that they use multi-emitter fluctuations or correlations between multiple frames in a time series while STORM relies on the occurrence of sufficient sparsity within individual image frames to directly allow single molecule localizations. This

makes that the former techniques are more generally applicable in microscopy since they work at higher densities and do not rely on strict blinking statistics of specific dyes. With the reduced bleaching rate in vacuum and inducible fluorescence blinking by the above mentioned works of Srinivasa Raja et al. [100] and Vos et al. (Chapter 3), distinguishing individual emitters in time at these high densities will become easier. Based on this, we expect higher quality localization reconstructions in integrated microscopy. Hence, we set out to explore the potential for these multi-emitter fluctuation-based localization techniques in integrated CLEM.

4.2. Methods

To assess the performance of different potential SR techniques suitable for integrated microscopy, we simulated series of light microscopy images. For each technique, image series with modified single emitter fluorescence dynamics compared to regular ambient fluorescence dynamics were simulated as discussed in more detail below. The resulting series of images were then fed to ThunderSTORM to localization single emitters [105]. The resolution of the reconstructed high-resolution images was then compared to the ideal scenario where each single emitter is emitting photons in a separate image frame with the same amount of fluorescence signal. We also quantified the different approaches by determining the number of missed or false positive localization events with the ground truth numbers provided by our simulations.

We study the following localization schemes for integrated microscopy. First, we study bleaching-assisted localization microscopy (BaLM), where consecutive image frames are subtracted from each other to discern the individual emitters that photobleach during each frame. As a second approach, we study electron-induced blinking dynamics where a subset of the emitters temporarily switches off due to electron irradiation occurring at regular intervals. To retrieve individual emitters even at high densities we use a Haar wavelet kernel approach proposed by Marsh et al. [37]. Third, we look at a photo-induced recovery after electron-induced darkening. Here, most of the fluorescent emitters are switched off with electron irradiation to obtain a sparse number of fluorescing emitters. Then, the switched off emitters are switched on again using photostimulation and the process is repeated. The final approach involves regularly switching a subset of non-fluorescing emitters temporarily on with electron irradiation. The parameters describing these dynamics are based on values found in literature, or chapter 3 in this thesis.

4.2.1. Simulations

To generate a series of microscopy images we first generated a list of individual fluorescent emitters that are defined by an x,y-coordinate, photon yield per second, point in time where they photobleach, and different timepoints where they switch on/off depending on the SR technique. To convert this data from each individual

emitter, we first define the full width at half maximum (FWHM) of the point spread function (PSF), the camera pixel size, the exposure time and the amount of background noise. We then calculated the individual contribution of each emitter to the signal per pixel per camera frame to obtain an image series. This simulated image series was then loaded into ThunderSTORM [105] to localize the emitters and reconstruct a final SR image. These SR images were then used to determine the final resolution of different exemplary molecular arrangements, and to compare with ground truth data provided by the positions of the emitters as generated at the start. All simulations were implemented using Python 3 and can be found at `https://github.com/hoogenboom-group/SR_simulator`.

All parameters used in our simulations were based on values experimentally observed by us (Chapter 3) or others [100]. The PSF FWHM and camera pixelsize were based on our own setup and were set to 380 nm and 100 nm respectively. The shot noise contribution to the background noise was calculated by taking a random value per pixel from a Poisson distribution of which the mean was set to the total intensity level of that pixel. After that, a background noise with normal distribution of 200 photons/s variance was added. We chose a normal distribution as the contributions to the background noise can come from different independent background contributions such as read noise from the camera and background fluorescence.

We modelled different fluorescent molecules, taking values reported by Srinivasa Raja et al. [100] for respectively tetramethylrhodamine (TRITC) and Alexa Fluor 594 (AF594) in vacuum and ambient conditions. We modelled tetraphenoxy perylene diimide (PDI) and rhodamine isothiocyanate (RITC) in vacuum based on the experimental values found in Chapter 3. The signal strength was set to 1700 photons/s for all molecules, except for AF594 in ambient conditions. AF594 average fluorescence intensity in ambient conditions was increased by 25% to reflect the dimming in vacuum observed by Srinivasa Raja et al. [100]. The signal strength was then multiplied by the camera exposure time and the fraction of time an emitter was on during the camera frame. When comparing our estimates for the background noise and photon yield we find comparable although slightly lower SNR values as to for example Marsh et al. for similar PSF size [37]. However, due to our larger PSF we expect to obtain lower resolution reconstructions as the total signal is spread out across more pixels. Four scenarios for the fluorescence dynamics were implemented as described below.

Photobleaching lifetimes & bleaching assisted localization

The point in time where the simulated emitter photobleaches was drawn from an exponential distribution resembling the reported photobleaching lifetimes. Once photobleached, the emitter intensity was set to zero. Photobleaching lifetimes reported in the literature were based on an excitation intensity of 185 W/cm^2. As we base our simulations on fluorescence intensity and background levels observed for 2 kW/cm^2, we assumed a linear scaling of the photobleaching lifetimes in this

excitation range. This led to fluorescent lifetimes of 10.3 s and 103 s for TRITC and RITC, and 4.96 s and 12.4 s for AF594 in respectively ambient and vacuum. Perylene lifetimes were measured with a light source fluence of 0.03 kW/cm^2 and scaled linearly, resulting in lifetimes of 87.5 s in vacuum (Chapter 3). The number of images of each image series was set to 4 times the photobleaching lifetime given the camera exposure time.

Electron irradiation induced blinking dynamics

Electron irradiation induced blinking was simulated by temporary switching off molecules, across the image field of view followed by gradual recovering. Parameters were based on observations in our previous experimental work using PDI molecules (Chapter 3). In our simulations, electron irradiation across the entire field of view was repeated every 200 ms. After each irradiation, molecules were switched off with probabilities P(O) ranging from 0% - 30% which is based on the data presented in chapter 3 for electron landing energies ranging from 0 eV to 5 eV (Fig. 3.2). A switched off molecule had a 10% probability to be permanently bleached. The non-bleached molecules were switched back to the fluorescent state by drawing dark state residence times from an exponential distribution with an average 1.3 s lifetime, based on figure 3.2. We assumed that emitters in a dark state were unaffected by low-energy electron irradiation. Thus, once an emitter was switched to a dark state, additional electron irradiation would not prolong the dark state or cause the emitter to bleach in our simulations. The timespan of each image series was set to 4 times the photobleaching lifetime, and camera exposure time was set to 600 ms. 10 unique image series were generated per structure for each value for P(O).

Photo-induced recovery after electron-induced darkening

We simulated fluorescence dynamics for molecules switching to dark state caused by electron irradiation, and an instantaneous recovery of fluorescence caused by a photostimulation. We can achieve sparsity in an image frame with the electron irradiation such that we can perform localization on the single emitter. By then switching all the dark emitters on again, we can repeat this process again until a high-resolution image can be reconstructed. For this technique of photo-induced recovery of electron-induced dark states we based our values on our experiments performed on RITC molecules (Chapter 3). In our simulations, we started electron beam exposures at 1.2 s and repeated those at intervals of 3 s. During electron beam exposures the RITC emitters were allowed to switch off with a probability P(O). Emitters that switched to an off-state could either enter a temporary dark state with a probability $P(D \mid O)$ or permanently bleach with probability $P(B \mid O)$ i.e., $P(B \mid O)$ = 1-$P(D \mid O)$. All emitters in a dark state could switch on again after a photo-excitation which started at 3s and repeated at an interval of 3 s. We assumed that emitters in an off-state were unaffected by additional electron beam exposures.

Due to a fraction of the emitters bleaching after every electron iteration, the density of the emitters that can still be switched decreases after every iteration. Therefore, to retain an optimal sparsity after each electron irradiation we scale P(O) after every iteration to have an expectation value of 1 fluorescing emitter after electron irradiation: $P(O)_n = 1 - 1/(N - N_{bleached})$. Where N and $N_{bleached}$ respectively represent the total number of emitters and the number of bleached emitters. For the first electron irradiation (n=0), we regard none of the emitters bleached, i.e. $P(O)_0 = 1 - 1/N$. The number of bleached molecules before electron irradiation at iteration n can then be described as follows:

$$N_{bleached} = (N-1) \cdot (1 - P(D \mid O)^n) \approx N \cdot (1 - P(D \mid O)^n) \tag{4.1}$$

Where N-1 originates from the fact that every iteration we expect 1 emitter to remain on. From the expression of $N_{bleached}$ follows:

$$\begin{aligned} P(O)_n &= 1 - \frac{1}{(N \cdot (1 - (1 - P(D \mid O)^n)))} \\ &= 1 - \frac{1}{(NP(D \mid O)^n)} \\ &= 1 - \frac{(1 - P(O)_0)}{(P(D \mid O)^n)} \end{aligned} \tag{4.2}$$

We use this final expression to scale the probability of switching off fluorescent molecules after every iteration.

We varied the likelihood of bleaching after electron irradiation $P(B \mid O))$ from the experimental value of 25% to up to 1% to see the effect on image reconstruction quality. Since with higher $P(B \mid O))$ values more emitters bleach with fewer electron irradiations we increased the timespan of each image series from 54 s to 1380 s for respectively $P(B \mid O))$ = 25% to 1%. For each image series, we've used a camera exposure time of 600 ms.

Fluorescence brightening after electron irradiation

Finally, we ran simulations on emitters becoming fluorescent after electron irradiation. Here a fraction of fluorescent emitters was switched on, such that these could be localized. After sufficient time, these molecules would switch off again and the process could be repeated. In these simulations of the electron-induced brightening of fluorescent molecules, we used parameters based on our observations for AF594 (Chapter 3). The measured lifetime of the brightened state was 48 seconds for an excitation intensity of 0.03 kW/cm^2. As in the simulations we used photon yields that would match to an experimental situation with 2 kW/cm^2 excitation power, we again assumed linear scaling of the photobleaching lifetime to obtain a simulation value of 0.72 s. Electron exposure was simulated at intervals of 3 s. After electron exposure each emitter had a chance to switch on. These probabilities were set to the inverse of the number of molecules in the PSF for the different structures. Once in

the bright state, the molecule was assumed unaffected by the electron irradiation and emitters were allowed to switch on multiple times, until photobleaching. For the image series we've used a camera exposure time of 200 ms and the number of electron irradiations was varied according to the different molecular arrangement described in detail below. This meant that we used 140 electron irradiations for the spaced circles, 400 for the ring and 1000 for the crossing lines.

4.2.2. Localizations

All localizations were performed using ThunderSTORM [105]. For BaLM and HAWK, data was filtered with 100 nm < σ < 200 nm, for other techniques with 140 nm< σ < 180 nm. Particle detection used a wavelet filter of 'B-Spline order' 3 and 'B-Spline scale' of 2. We used the 'integrated Gaussian' PSF model and maximum likelihood estimation with a fitting radius of 6 pixels. For BaLM and electron-induced blinking, images were processed before performing the localizations. For BaLM, consecutive frames were subtracted to perform localization on the resulting image series. For the electron-induced blinking emitters we first used HAWK [37] using a group level of 5 and separating the negative and positive values. We then used ThunderSTORM with multi-emitter (ME) fitting on the HAWK output limiting the number of emitters per PSF to 2.

4.2.3. Simulated molecular arrangements

For all four scenarios, we used three types of structural arrangements to assess the performance of the localization microscopy algorithms. The first structure consisted of two 128 nm diameter disks at an edge-to-edge separation of 100 nm, each containing 45 randomly distributed molecules. We chose this structure because it resembles the situation we encounter for antibody labelled insulin granules in zebrafish tissue (P. de Boer, B. N. G. Giepmans, personal communication), which could serve later as an experimental validation system. The second structure consisted of ring-like arrangements with diameters ranging from 200 nm to 600 nm and emitter density of 200 emitters per µm along the circumference. As a third structure, we used two lines crossing at an angle of 30°, with separation varying from 0 nm to 400 nm, and a density of 1000 emitters per µm. Finally, for BaLM, additional simulations were carried out with 100.000 emitters randomly distributed across 256x256 pixels giving a density of 153 emitters per μm^2. All these generated molecular positions served as ground truth in the evaluation of localization performance.

4.2.4. Precision and recall

The performance of the localization approaches was quantified using recall, i.e., the ratio of correctly localized versus total emitters, and the precision, i.e., the ratio between correctly localized and in total localized emitters. These were determined

by first filtering per frame both the localizations and their coordinates, and the molecules tthat should be localized because of for example bleaching or blinking during that frame, i.e. the ground truth. Next, we calculated the distances between the localizations and ground truth positions and find the optimal minimal distances between their coordinates of the set using a linear sum assignment algorithm. Finally, we excluded emitters with a distance larger than a tolerance radius of 100 nm for BaLM and HAWK, or 30 nm otherwise. We then calculated the precision and recall and repeat this procedure for 10 image series, after which finally the average recall and precision were calculated.

4.3. Results

We evaluated four scenarios for localization-based SR microscopy exploiting altered molecular fluorescence dynamics that could be achieved in integrated microscopy. These are: (i) altered photobleaching dynamics, specifically prolonged fluorescence lifetimes, under vacuum; (ii) fluorescence reversible switching induced by timed, localized electron exposure, (iii) instantaneous photo-induced fluorescence recovery after electron exposure induced darkening, and (iv) fluorescence brightening induced by electron exposure. Below, we present our simulation results for each of these four scenarios.

4.3.1. Bleaching-assisted localization in vacuum

In bleaching-assisted localization, consecutive image frames are subtracted to generate sparsity due to the subset of molecules photobleaching between the frames (Fig. 4.1A). We used parameters experimentally obtained for Alexa Fluor 594 (AF594), a bright and stable dye often used in biology experiments in ambient conditions and found to exhibit prolonged photostability in vacuum, and tetramethylrhodamine (TRITC), a dye that was observed to be particularly bright and stable in vacuum [100]. We refer these two model cases with the respective molecular dye names. Subtracted image frames at 3x the photobleaching lifetime clearly demonstrate the improved sparsity in vacuum compared to ambient for both AF594 and TRITC (Fig. 4.1B). Note that for AF594 the reduced fluorescence signal in vacuum compared to ambient is also apparent, as is the higher fluorescence intensity per image frame compared to TRITC. For TRITC the dimming between ambient and vacuum does not occur. Yet its 10x and 20x longer photobleaching lifetime in vacuum compared to TRITC and AF594 in vacuum, respectively, leads to an even more sparse distribution. This is also evident upon comparison of the number of molecules that have not photobleached as a function of time (Fig. 4.1C). Hence, we expect for TRITC in vacuum to have a lower amount of overlapping bleaching emitters per camera frame, compared to the other scenarios. This should lead to more localizations compared to the other conditions, while the higher signal per frame for AF594 in ambient conditions favors the likelihood of discerning a molecule over the back-

ground. We therefore assess the quality of the reconstructions for AF594 in ambient versus TRITC in vacuum next.

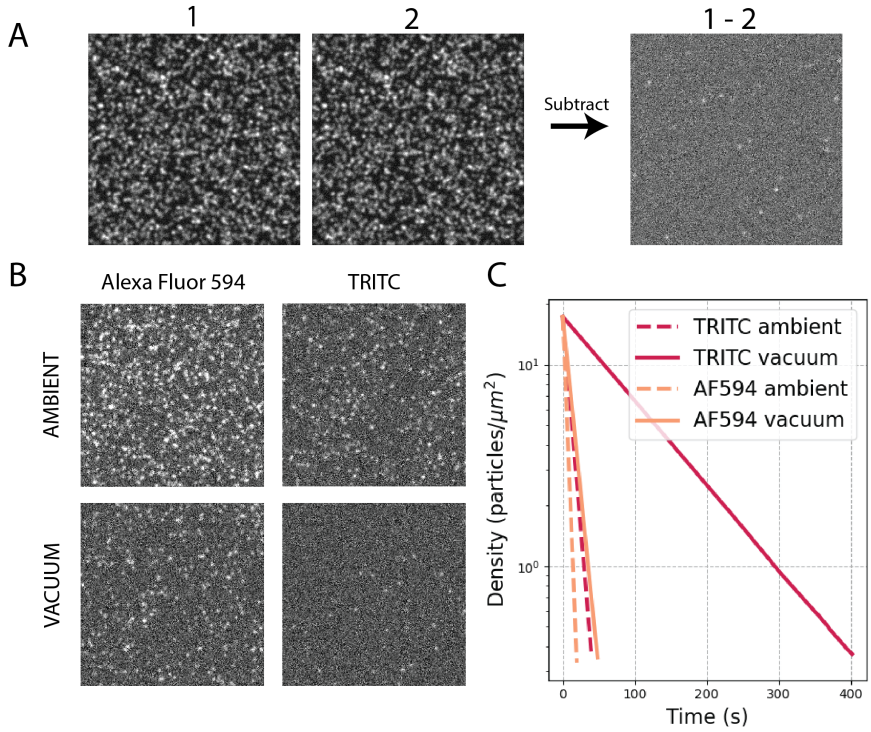

Figure 4.1: (A) Simulated consecutive frames of randomly distributed AF594 molecules are subtracted to obtain a sparse image on which localization can be performed. (B) Resulting subtracted simulated images obtained at t = $3\varnothing_{pb}$ for AF594 and TRITC in ambient and vacuum conditions. AF594 has 25% increased luminescence in ambient conditions compared to vacuum. While in vacuum conditions the photobleaching lifetime increases (C) by 2.5x to 12.4 s for AF594 and 10x to 104 s for TRITC.

Three different structures were simulated and reconstructed based on the subtracted images series: two 128 nm diameter disks with an edge-to-edge separation of 100 nm, a 600 nm diameter ring, and two lines crossing at an angle of 30° (Fig. 4.2A). The first structure was chosen as it could represent an experimental validation system consisting of immuno-labelled insulin granules in zebrafish pancreas tissue which is often used in our lab. The second structure could represent a fluorescence labelled vesicular membrane or membrane protein. The third has varying molecular separation and could represent a pair of crossing microtubules or actin fibers.

Each of these three structures are clearly unresolvable in wide field fluorescence, while ground truth data generated by localizing each simulated emitter individually reveals the input structures (Fig. 4.2A). The images reconstructed with bleaching-assisted localization for AF594 in ambient and TRITC in vacuum show the differ-

ences expected from the result of Fig. 4.1: AF594 shows only very few but clear and high intensity localizations; TRITC shows many more localizations due to the reduced photobleaching rate but with lower intensity and higher uncertainty. For AF594, localizations are too few to discern any of the structures, which is confirmed with cross-sections taken along the center of the structures (Fig. 4.2B). For TRITC in vacuum the structures can be resolved based on the cross-sections, but for the two granular circles it is apparent from the images that this is only the case for this specific row of pixels. For the 600 nm ring with TRITC in vacuum it can be seen that molecules are localized around a ring, but the precise shape and width cannot be determined. Finally, for the crossing lines, the cross section reveals the presence of two lines for 180 nm spacing, which for increasing spacing is also evident upon visual inspection of the reconstructed image. Thus, while AF594 in ambient gives a higher localization accuracy, TRITC in vacuum will lead to a higher number of localizations needed to extract information about underlying structural detail. To better assess how well the input structures are resolved we also conducted a false positives and negatives analysis.

Recall, the ratio of correctly localized and total emitters, and precision, the ratio between correctly localized and total number of localized emitters were calculated and averaged over 10 image series. For recall, we find no significant difference between the separated disks for AF594 and TRITC (Fig. 4.2C). For the other two structures recall is significantly higher for TRITC in vacuum. Since recall represents missed localizations, this is most likely caused by simultaneous bleaching of multiple emitters during a single frame in case of AF594. Both the 600 nm diameter ring and the crossing lines have many emitters in the area of the PSF at the start of image acquisition (respectively 150 emitters and 850 emitters) with respect to the disks (90 emitters per PSF). Thus, for these higher densities we expect a larger amount of overlapping bleaching emitters resulting in a lower recall. For the precision (Fig. 4.2D), we find higher values for AF594 compared to TRITC in case of the disks and crossing lines. Most likely, this is caused by the higher brightness and thus higher signal-to-noise-ratio (SNR) of AF594 in ambient conditions compared to TRITC in vacuum. We cannot draw conclusions for the 600 nm diameter ring structures due to the high uncertainty for AF594, which we expect to be caused by the low number of localizations. To decipher the dependence of recall on the local emitter density, we evaluated localization and recall as a function of the local emitter density.

We tracked the recall and precision for different local emitter density by conducting the averages over the 10 image series for different photobleaching timestamps and emitter locations. For TRITC, data was smoothed using a rolling average window of 50 datapoints. For the 2 disks, recall starts to improve at approximately <20 emitters within a PSF-sized area for both AF594 and TRITC (Fig. 4.3A, B). For the crossing lines, we observe an increase in recall below around 35 molecules in a PSF area for TRITC in vacuum, while for AF594 the recall remains poor. Finally, for the ring structure we find that the recall remains poor for all observed densities. The precision is close to 1 in both cases for the disks and crossing lines, while for the ring structure for TRITC in vacuum we find the precision starting to rise only below 10

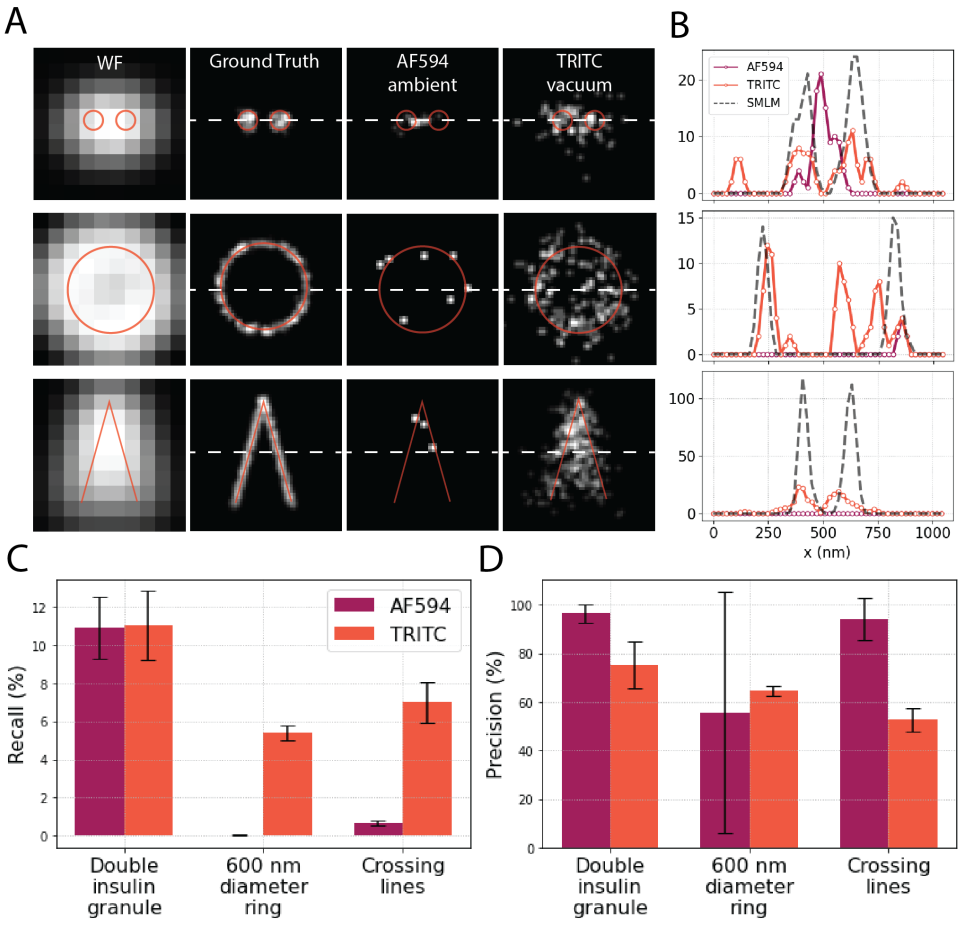

Figure 4.2: (A) Simulated LM data of 2 64 nm radius circles with 100 nm edge-to-edge distance (top), 600 nm diameter ring (center) and crossing lines (bottom). Photobleaching emitters of AF594 in ambient (ø=4.96s) and TRITC in vacuum (ø=103s) were localized using BaLM. TRITCs lower photobleaching rate allows for more localizations. Red lines indicate the ground truth structure. Cross-sections were taken across the dashed lines (B) and show how most structures cannot be resolved. The average recall (C) and precision (D) taken across 10 image series per structure show how TRITC in vacuum has a higher recall for high-density structures, while the precision is generally worse.

emitters in a PSF area. Surprisingly, we find that for the ring the precision initially decreases before it starts to rise again. This may be caused by several molecules bleaching at the same time at the highest densities, which results in there always being a localization close to any of the bleaching molecules.

We now use above established optimized densities for the different structures to see of this improves the final reconstruction image. We thus reconstructed the images after excluding the image frames where the local density was higher than the thresholds established above (Fig. 4.3C). Indeed localizations now appear closer to the ground truth, yet due to the low starting local densities, only few localizations appear. This makes that the structural detail can no longer be resolved using localization microscopy.

Our simulations suggest that TRITC could be used in vacuum to achieve a higher optical resolution for correlative microscopy using BaLM. We even find that it could

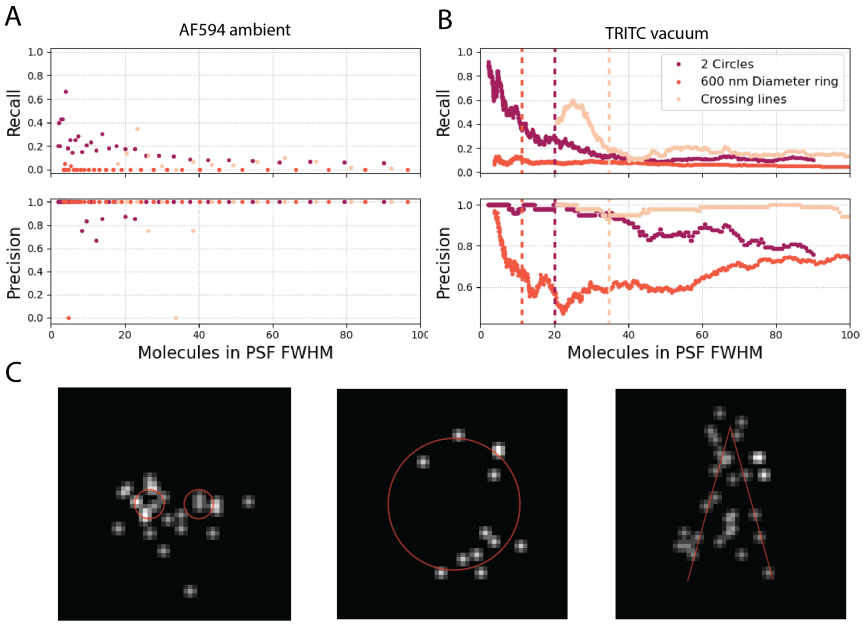

Figure 4.3: The recall and precision of (A) AF594 in ambient and (B) TRITC in vacuum given the average number of emitters in the PSF FWHM with a camera exposure time of 600 ms. For the 2 spaced circles we observe an increase in the recall 20 molecules in the PSF FWHM for both AF594 and TRITC. For the crossing lines we see the recall increase at 40 molecules in the PSF FWHM for TRITC in vacuum only. The recall for the 600 nm diameter ring remains low for both scenarios. The precision is generally high for most cases, except the 600 nm diameter ring with TRITC molecules in vacuum. We note that the number of datapoints for AF594 is significantly less due to the higher photobleaching rate, causing most emitters to be bleached within 32 frames. (C) Localization reconstructions of the spaced circles, 600 nm diameter ring and crossing lines started at frames where the density was approximately 20 emitters, 10 emitters and 35 emitters per PSF FWHM, as indicated by colored dashed lines in (B). Localizations are closer to the ground truth, but the structures themselves can no longer be resolved.

outperform AF594 in ambient conditions. Despite this, we find that the recall of this technique is poor resulting in generally <10% of the total emitters to be detected. Our findings, for ambient conditions, are found to be different from results found in literature [102, 106]. This could be due to the AF594 having a photobleaching lifetime of less than 5 s, while the data from, for example, Simonson et al. suggest lifetimes of hundreds of seconds. This could be explained by their use of oxygen scavenging agents to improve fluorophore stability while our data, based on the findings of Srinivasa Raja et al. [100], were reported without these agents. Another detail that could affect the result is a different estimate of experimental parameters, most notably SNR.

We established optimal emitter densities where, according to simulations, BaLM starts to improve in performance giving higher localization accuracy. However, we also find that the structural layout itself is unresolvable due to lower starting density yielding too few localizations. Yet, for integrated CLEM this does not have to be an issue since the underlying structure will be resolved with EM. Instead with CLEM, interest may primarily be on the location of the fluorescent molecules with respect to the EM structural detail, for which the bleaching assisted localization can give more information compared to the standard wide field FM. It would then simply suffice to record the wide field fluorescence time series until all molecules are bleached.

4.3.2. Electron beam induced reversible switching

We have previously demonstrated that electron irradiation can switch off a fraction of the fluorescent molecules in a sample followed by a gradual recovery on a seconds timescale (Chapter 3). Especially for electron landing energies close to 1 eV, most of the fluorescent molecules will recover their fluorescence. The resulting local intensity fluctuations in time could then be separated after which localization microscopy can be performed. Since, based on the experiments, up to 30% of the fluorophores can be expected to be temporarily switched off after electron irradiation, many local stochastic fluctuations are expected. Several methods have been developed to distinguish high-density stochastic fluctuations in wide field fluorescence time series. We chose to use HAWK in combination with ThunderSTORM multi-emitter (ME) fitting to minimize imaging artefacts during reconstruction [37]. HAWK uses Haar wavelet kernels of multiple orders to bandpass filter pixel fluctuations in time and then separates the positive and negative outputs. The output of the filtering results in sparse images on which the ME fitting can be performed.

Fluorescence emitters were modelled to be exposed to low-energy electron irradiation every 200 ms. After electron irradiation, each emitter was given a chance to temporarily switch off with a probability P(O). Once switched off, the emitter had a 90% probability to recover defined by a single exponential with a lifetime of 1.3 s. Besides these electron-induced fluctuations, fluorophores could photobleach when in the fluorescing on state. Figure 4.4A illustrates the procedure, showing 3

consecutive frames acquired with 600 ms exposure time. Between the first 2 frames electron irradiation occurs, causing a few emitters to switch off. In the final frame, a few emitters have switched on again. Using HAWK, we separate the temporarily switched off emitters from the ones permanently on as demonstrated in figure 4.4A. Here, application of a 1st order Haar wavelet kernel to frame 1 and 2 in figure 4.4A gives a sparse image which can then be used to localize emitters (Fig. 4.4B).

Electron-induced reversible switching in combination with HAWK drastically improves the resolution and quality of reconstructed images compared to BaLM in vacuum. The two disks (Fig. 4.4C) and the crossing lines (Fig. 4.4D) were simulated for P(O) ranging from 0% to 30%. In these reconstructed images we see that the number of localizations appears to increase overall compared to BaLM, even when there is no blinking induced. This could be caused due to using a Haar wavelet of multiple orders, allowing us to discern more photobleaching events then when using image subtraction between consecutive frames only. Interestingly, we seem to observe an inhomogeneity along the profiles of the crossing lines where less localizations appear halfway each line's length. The higher number of localizations at large line spacing could be explained by a lower local density of fluorophores. This results into a lower local SNR resulting in a higher likelihood of detecting a switching emitter. At spacings where the individual lines become unresolvable, more localizations per pixel appear because localizations from both lines will be added together. This could explain why the intensity along the line show a minimum halfway. With the electron-induced switching (P(O) $\geq$ 10%), we additionally observe an improvement in resolution of the reconstructed images. More specifically, we barely observe localizations in between the disks, and the crossing lines can be resolved to closer distances with electron-induced switching.

The resolution improvement with HAWK and electron-induced blinking is quantified by averaging 10 reconstructions per structure and per value for P(O). Cross-sections clearly show how for each switching probability the disks can be separated (Fig. 4.4E), even when P(O) = 0% and only photobleaching occurs. For the two lines, we see that lines down to 180 nm can be resolved for P(O) $\geq$ 10% (Fig. 4.4F).

We next assess reconstruction of the ring structure where in view of the successful results on the other structures, we varied ring diameter from 600 nm down to 200 nm, i.e. well below the diffraction limit. Rings can be resolved down to 300 nm diameter with P(O) = 10% (Fig. 4.5A), which is clearly confirmed in the cross-section profiles (Fig. 4.5B). The 300 nm diameter ring can also be resolved for the other switching probabilities (Fig. 4.5C), but the ratios between peak heights shift. Electron-induced switching lowers unwanted localizations close to the center of the ring compared to 0% switching probability. This all clearly demonstrates how using electron-induced switching in combination with HAWK can drastically improve the resolution fluorescence localization in CLEM.

Using HAWK for photobleaching samples, without electron-induced reversible switching of the emitters, results in higher quality of the reconstructed images

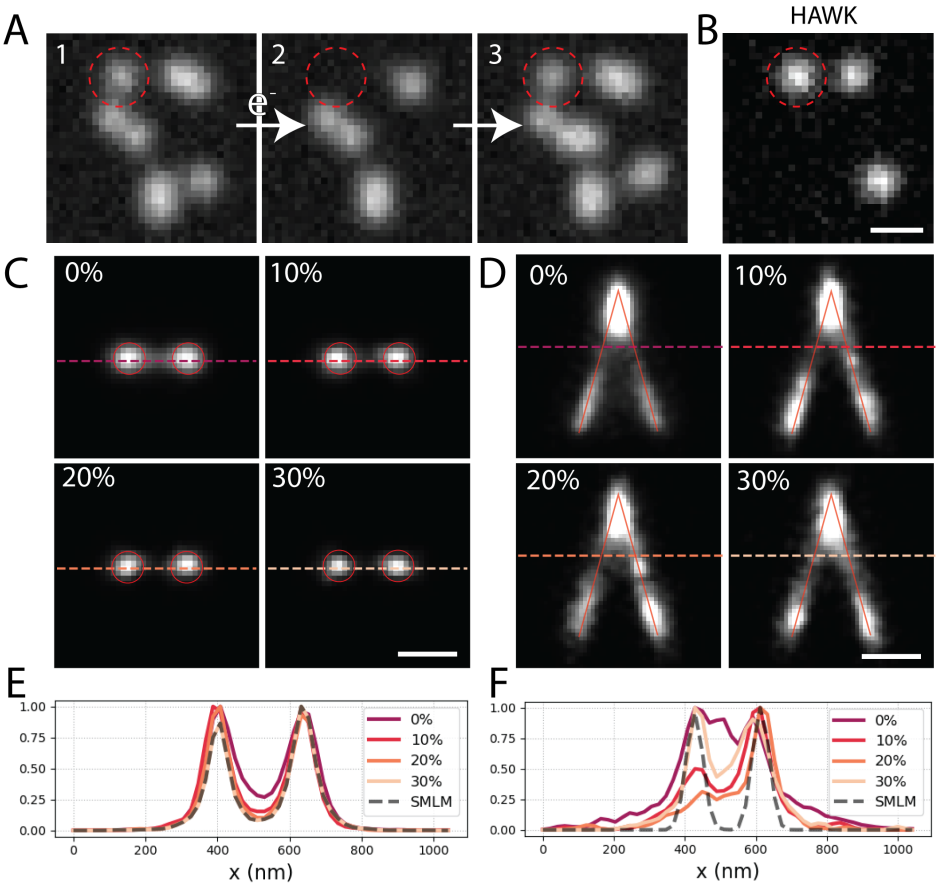

Figure 4.4: Simulation of molecules blinking after electron irradiation. (A) In typical consecutive frames in the simulation, fluorescent molecules such as the highlighted one are irradiated in (2) and recover in the subsequent frame. We use 5 level HAWK to distinguish blinking emitters in time, and perform localization on the output. (B) The level 1 HAWK output shows the blinking molecules between frame 1 and 2 of (A). Reconstruction of (C) two disks and (D) two crossing lines with different probabilities for molecules to switch off (P(O)). (E-F) cross-sections show the improved resolution for blinking emitters, and up to 180 nm resolution for the crossing lines. All reconstructions were averaged over 10 image series. Scale bar: (A-B) 800 nm, (C-D) 300 nm

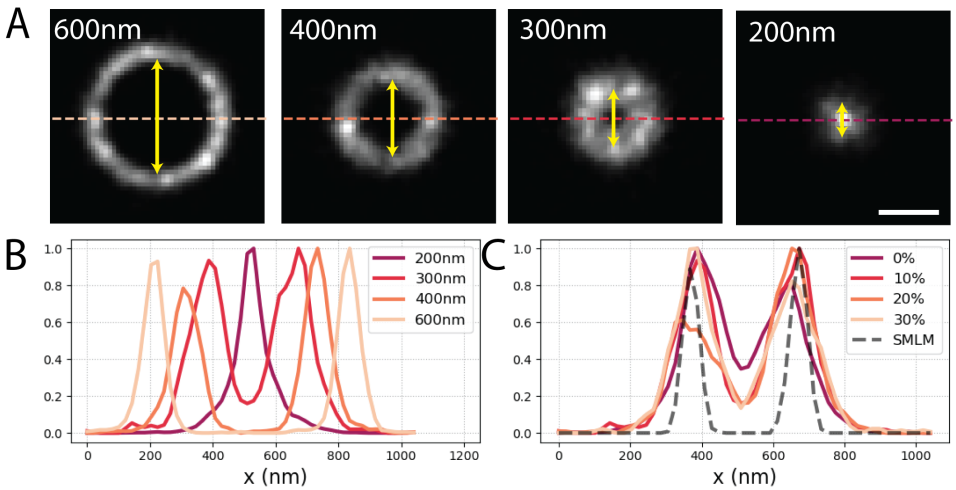

Figure 4.5: HAWK reconstructions of electron-induced blinking perylene molecules in a ring configuration. (A) Reconstruction of ring structures of different diameter with 10% probability for molecules to switch off and (B) cross-sections show that this structure is resolvable to up to 300 nm diameter. (C) Cross-section of 300 nm ring for different P(O) show that 10% gives the highest resolution without shifted intensities in the peaks. All reconstructions were averaged over 10 image series. Scale bar: 300 nm.

than when using the BaLM dataprocessing. This approach using HAWK should be feasible for other dyes as well, including TRITC, due to the generic nature of photobleaching of the emitters. Furthermore, the quality of the reconstruction is expected to improve further in practice since emitters in vacuum also show blinking behavior, resulting in possibly more localizations per emitter [100]. The number of localizations and the resolution of the technique would improve even further when introducing the reversible electron-induced switching. This switching should also prolong the photobleaching lifetime of emitters more prone to photobleaching as these emitters will spend more time in a transient dark state. While HAWK combined with ME-fitting has several advantages over BaLM in the final reconstruction of optical images, we would also like to note that the computational cost is higher due to (i) the use of ME-ftting and (ii) multiple localizations of the same emitter due to the higher order Haar wavelet filter.

Using HAWK, structures can be resolved with higher detail compared to images acquired with wide field imaging. We note however, that for smaller line spacing and rings of 200 nm diameter the technique is unable to resolve the structures in detail. To resolve these structures in more detail, single molecule localization microscopy techniques could be utilized. However, to perform single molecule localization inside an SEM calls for the use of unconventional techniques to switch the emitters on/off. Low-energy electron irradiation at few eV landing energies can help with this, since the lower energy gives a more precise control over which states are induced in the fluorescence. In the next paragraphs, we describe and

verify single-molecule localization techniques that would utilize low-energy electron beams.

4.3.3. Instantaneous photo-induced fluorescence recovery after electron-induced switch-off

We have previously demonstrated that molecules may be photo-stimulated to switch on after being switched to a dark state with low-energy electron irradiation. The reported example for this approach was Rhodamine B isothiocyanate (RITC), which could be photo-switched on again using a 405 nm pulse exciting the radical anion formed after electron irradiation (Chapter 3). Thus, we could temporarily create a sparse number of fluorescent emitters by switching most of the emitters off with electron irradiation (Fig. 4.6A) such that high accuracy localization can be performed on the emitters that are still on. Then, by using the photo-stimulation, all dark particles can be switched on again and the process can be repeated until most emitters are localized. This would bring an advantage over the previous approach since all localizations can be performed with sufficient sparsity to do (near-) single molecule localization which should give higher accuracy. We therefore conducted simulations where at fixed intervals several emitters are first switched to a dark state followed by photo-stimulated recovery of all dark emitters switch on.

In our simulations, electron irradiation and thus molecular fluorescence switch-off occurs every 3 s, and is set such that only 1 emitter remains on. Experimentally, this would mean that the probability to switch off an emitter, P(O), would be tuned at each step by adjusting the electron dose. The initial dose would then be set by an estimate of the local emitter density based on detected fluorescence signal. The switched off emitters are then given a probability to be in the dark state, ($P(D \mid O)$), or to be permanently bleached, $P(B \mid O)$), with $P(B \mid O)) = 1 - P(D \mid O)$. 1.8 s after electron irradiation, the photo-recovery is simulated by switching all dark emitters on again. Thus, after every iteration the total number of fluorescent emitters is reduced by a factor of 1 - $P(B \mid O)$).

Two disks labelled with RITC molecules with dimensions and labelling density like before were modeled according to the above scheme. The probability to permanently bleach from the dark state was varied from $P(B \mid O)) = 25\%$ to $P(B \mid O)) = 5\%$ and $P(B \mid O)) = 1\%$. A 25% likelihood to bleach after electron irradiation corresponds to the average values found for RITC in Chapter 3. Image reconstructions in this case reveal how only a few emitters are localized, which improves considerably for lower bleaching odds (Fig. 4.6B, C). Thus, with 25% of switched emitters bleaching per switching and localization cycle, too many emitters are lost before they can be localized. Furthermore, localizations observed in between the disks suggest that multiple emitters in separate disks remain on after electron irradiation. These artefacts appear to decrease when the odds of bleaching after electron irradiation decrease.

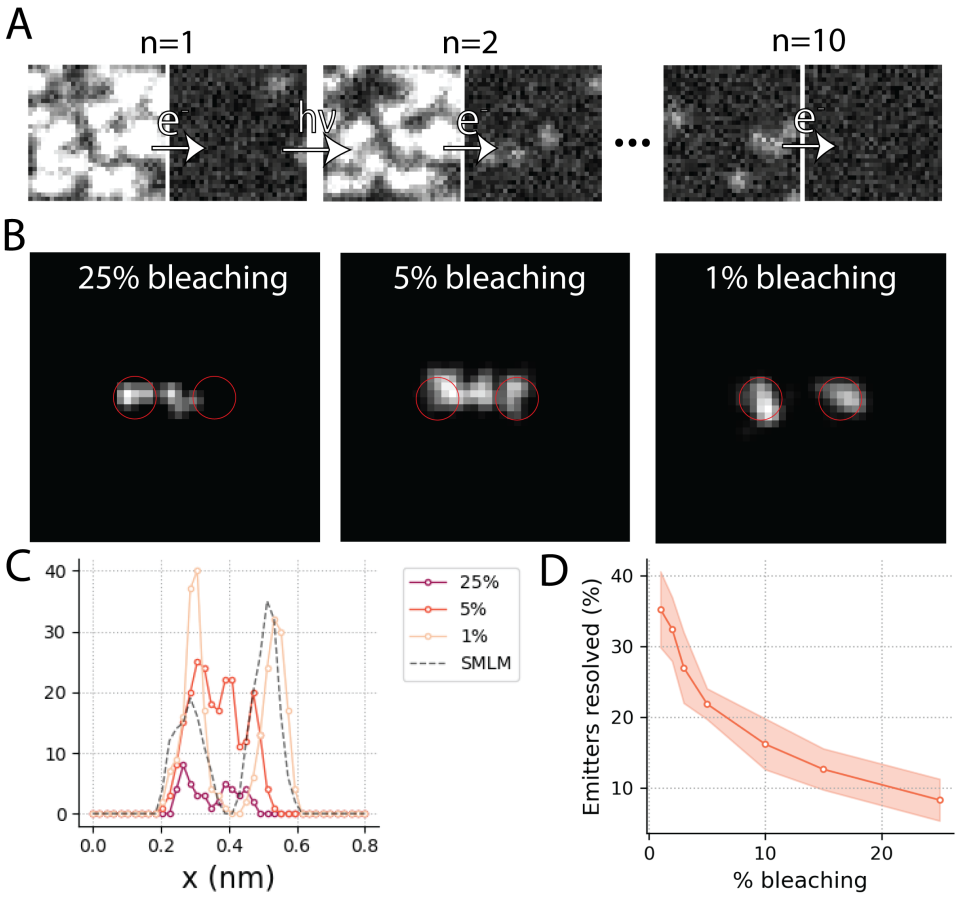

Figure 4.6: Simulations on RITC, localization microscopy is performed by (A) creating sparsity with electron irradiation (e-) until most emitters are switched off given by P(O), followed by a photostimulus (h$^\circ$) such that dark molecules switch on again. This process can be repeated multiple times, but after each electron exposure a number of emitters will bleach with probability $P(B \mid O)$). This leads to a decreasing number of emitters recovering after each iteration as can be observed between n=2 iterations and n=10 iterations. (B) Reconstructions and (C) cross-sections for different percentages of bleaching per electron irradiation demonstrate how the reconstruction quality improved with lower probabilities of bleaching. The quality in reconstruction improves due to an increasing amount of emitters being localized. (D) The fraction of emitters localized (orange) given the probability to bleach after electron irradiation confirms that the fraction of total emitters detected is the main contributor for quality of the image reconstruction.

We verified the importance of emitter bleaching by calculating the fraction of total emitters detected, which was done in a similar way as the recall calculations in the previous sections except for setting the tolerance radius to 30 nm (Fig. 4.6D). Decreasing P(B | O)) from 25% to 1% shows significant improvement of the percentage of emitters resolved. With P(B | O)) = 25%, only 7% of the emitters are localized, which increases to 35% for P(B | O)) = 1%. Note that the latter value is far from the 100% of total emitters. Two factors in particular contribute to this. First, the expectation value of having 1 emitter that remains fluorescing per iteration, implies that also none or more than one emitters can be on after an electron irradiation cycle. Second, individual emitters can be localized multiple times, especially when the density of emitters decreases as the number of cycles increases. Including both effects in a simple probabilistic model is difficult due to the decreasing number of particles affected after each electron irradiation and the changing probability of number of particles switching off after each cycle.

Reduction of the electron-induced bleaching probability to 1% (i.e. P(B | O)) = 1%), gives superior performance for this approach compared to HAWK. This is further illustrated with localization and reconstruction results for a 200 nm diameter ring and the crossing lines structures. For P(B | O)) = 25%, we find only a handful of emitters along the structures due to a large number of emitters that bleach (Fig. 4.7A). Meanwhile, both the 200 nm ring, and the crossing lines down to 100 nm spacing can be resolved (Fig. 4.7B-D). Thus the switching and recovery scenario of photo-induced switching indeed improves resolving spatial layout of molecular labelling over pure blinking approaches bringing this closer to more traditional single molecule localization approaches.

The localization accuracy using the instantaneous photo-induced switching technique is expected to be unaffected by the emitter density if the density is properly estimated a priori. In figure 4.6B we see localizations in between the two spaced circles, explained by multiple emitters in separate circles being on after electron irradiation. The probability of having 2 or more emitters will be given by 1 minus the probability of having 0 or 1 emitter remaining on after electron irradiation:

$$P(N_{on} \geq 2) = 1 - P(O)^N - N(1 - P(O))P(O)^{N-1} \tag{4.3}$$

Since we scale P(O) such that only 1 emitter is expected to remain on (P(O)=1 – 1/N), we obtain:

$$P(N_{on} \geq 2) = 1 - (1 - \frac{1}{N})^N - (1 - \frac{1}{N})^{N-1} \tag{4.4}$$

For N in the range between $N = 1 \cdot 10^2$ to $1 \cdot 10^4$ we then get $P(N_{on} \geq 2) \approx 0.26424$ for all values of N in this range. Thus, the dependency of multiple emitters on after electron irradiation on the local density is negligible if one scales P(O) accordingly. This probability could be reduced even further by decreasing the expectation value to even lower than 1 emitter on. This would come at the cost of the recall, as the expected number of localizations per electron irradiation decreases while the

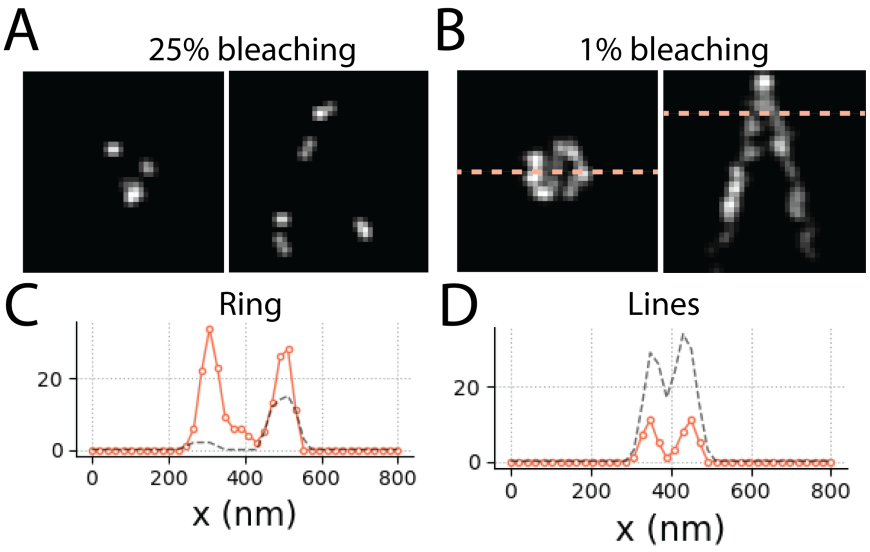

Figure 4.7: Instantaneous photoswitching of electron induced dark states with low odds to bleach after electron irradiation result in high-resolution images. Reconstructed images and cross-sections for the technique where (A) 25% and (B) 1% of the emitters bleach after being electron irradiated for (left) a 200 nm diameter ring and (right) crossing lines. (C-D) Cross-sections show how for the crossing lines (D), a minimal spacing of 100 nm is reached by temporarily creating sparsity with electron irradiation followed by an instantaneous photo-induced recovery.

expected number of bleached emitters will increase. More issues could arise when the emitter density is not known a priori. In this case P(O) and the scaling of P(O) will be off, which could lead to significantly more imaging artefacts if the emitter density is underestimated.

Localization microscopy using instantaneous photoswitching of electron-induced dark states in correlative systems allows for higher localization accuracy compared to methodologies based on photobleaching or blinking of overlapping fluorophores. However, such a technique comes at the cost of recall due to the limiting number of localizations possible. Using commercially available RITC with a 25% probability to bleach after switching dark would mean that only 7% of the emitters are localized for a structure with 90 emitters hidden in the PSF. For the ring and crossing lines we find similar issues, although we still appear to have a high localization accuracy. As mentioned before, the low recall does not always have to be an issue since many structures can be resolved with EM in CLEM. Decreasing the likelihood of bleaching results in a much better-quality reconstructed image. For 1% of the emitters bleaching after electron irradiation, each structure can be discerned with high accuracy. The downside of photo-induced switching technique is that, to obtain sufficient sparsity, one needs to have an estimate of the density of emitters beforehand, which is not always practical. This means that during experiments one needs to optimize the dose beforehand such that only 1 emitter remains on. This

makes it tricky to use this technique if one does not know everything about the sample beforehand and could lead to imaging artefacts. In a practical setting, the electron dose should therefore be calibrated beforehand. This in turn, could lead to high-resolution optical images in CLEM using instantaneous photoswitching of electron-induced dark states.

4.3.4. Electron-induced brightening localization microscopy

Besides an electron-beam induced switch off, we also obtained proof of principle for electron-induced partial switch on with Alexa Fluor® 594 (AF594) (see Chapter 3). An ideal optimized dye would temporarily switch on after electron irradiation, and shortly afterwards return to a non-absorbing or dark state. Sparsity would then be achieved temporarily by switching a fraction of the emitters on with the electron beam, allowing localization and repetition of the procedure after darkening (Fig. 4.8A). In this way, single molecule localization microscopy could be performed similar to traditional techniques such as PALM, but for conditions and dyes compatible with the environment of an electron microscope.

We simulated this scenario starting with an estimated lifetime of the on state of 0.72 s based on the observations described in Chapter 3. Because of this relatively short lifetime, we set the camera exposure time to 200 ms to ensure that each molecule was detected. We then implemented electron exposure with 3 s intervals, switching a fraction of the molecules on. A binomial distribution was implemented for the probability to switch a molecule on after electron irradiation by setting P_{on}, the chance for a emitter to switch on, to approximately the inverse of 3 times the number of molecules in the underlying structure. We chose this probability to ensure that only none or 1 emitter would switch on after the irradiation. This way, imaging artefacts due to multiple emitters at the same time lighting up are minimized. Taking the same sample structures and molecular densities as before, this meant $P_{on} = 1/270$ for the two disks, $P_{on} = 1/375$ for the 200 nm diameter ring, and $P_{on} = 1/2400$ for the crossing lines. Thus, we have approximately 24% chance to switch only 1 particle on for each of the structures. Experimentally. this probability could be controlled with the electron dose. Once in the on state, we assumed that the particles are unaffected by electron irradiation, but they could undergo photobleaching as described in previous scenarios. Finally, emitters were allowed to switch on again after being switched on in previous exposures.

All three test structures can be clearly resolved using this approach with results very similar to the localization ground truth (Fig. 4.8B-D). The crossing lines can be resolved down to a separation of 120 nm. Calculation of the total number of unique localizations in each structure using a tolerance radius of 30 nm reveals 15 ± 4% of emitters in the disks, 18 ± 3% of emitters in the ring, and 11 ± 1% of the emitters in the crossing lines are actually localized. While these numbers may seem low, direct estimation of the expected number of localizations based on the input emitter densities, the 24% probability of switching just one emitter on, and respectively 140,

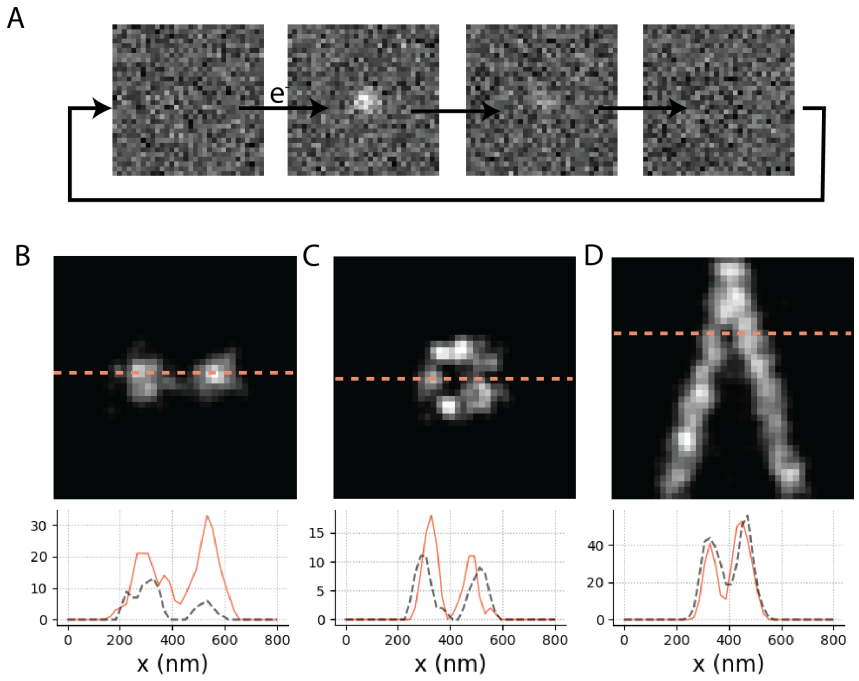

Figure 4.8: Simulations of an emitter that brightens after electron irradiation. Localization microscopy is reached by (A) turning a single molecule on with the electron beam, wait until it returns to a dark state and then the process is repeated. Reconstructions were performed after (B) 140 electron exposures with 1/270 probability to switch a molecule on for two spaced circles, (C) 400 electron exposures with 1/753 probability to switch a molecule on for a 200 nm diameter ring and (D) 1000 electron exposures with a 1/2400 probability to switch a molecule on for two crossing lines. The cross-sections of the reconstruction (orange) and ground truth (dashed, black) taken at the dashed lines in the image show how both the circles and ring can be resolved, and the lines up to 120 nm separation.

400, and 1000 cycles, indicates that only 30%, 32%, and 20 of emitters are expected to be localized for respectively disks, ring, and crossing lines (see Appendix).The lower values found in our simulations may be due to emitters drowned in the background. Indeed, when we determine how many individual emitters light up after electron irradiation in our simulation files which ignores drowning in background noise, we find that 33 ± 4%, 34 ± 3% and 19 ± 1% respectively, light up. Thus we conclude that the above retrieved estimated percentages of molecules actually being localized are correct. Therefore, besides the number of switching cycles and probability to switch only one molecule on, background reduction is key to localizing more molecules more accurately. We also note that these values would not be different for similar techniques where switching is done by other means than low energy electron irradiation. The above numbers could further be improved by increasing the number of cycles. In the experimental situation this number needs to be balanced to the allowed total experiment time when considering experimental factors like drift.

The resolution of 120 nm that we obtained on the crossing lines structure is lower compared to what we observed for the photo-induced recovery. This could be explained by the lower camera exposure time used here, resulting in a lower SNR. We selected our exposure time here based on the experimentally estimated lifetime of the on state. Higher excitation intensity and/or search for molecules with a longer on-state lifetime could further improve the resolution for this approach. Unlike the photo-induced recovery, the local molecular density does not have to be estimated before starting the localization experiments. The relevant prerequisite for this approach is that the electron dose needs to be chosen such that the chance for switching on more than one molecule per PSF-equivalent area is substantially low. Thus, further experimental development and implementation of this approach needs establishing the calibration curves for switching vs electron dose.

4.4. Conclusion

We have proposed three new approaches for superresolution fluorescence microscopy that could be conducted in an integrated fluorescence and scanning electron microscope thanks to altered characteristics of fluorescent molecules in vacuum or under electron irradiation. For each of these approaches, we demonstrated the experimental feasibility using computer simulations based on experimentally observed parameters. The first approach relies on a prolonged photobleaching lifetime in vacuum compared to ambient followed by localization via subsequent image frame subtraction (BaLM) or via higher order correlation of pixel intensity fluctuations (HAWK). HAWK was observed to show superior performance compared to BaLM in terms of resolution and number of resolved molecules, at the cost of computation time. Moreover, application of HAWK would allow for a relatively straightforward implementation of superresolution microscopy in the vacuum of an integrated correlative setup. Evaluation of a wider palette of fluorescent dyes for use in vacuum aiming for prolonged photobleaching lifetime and frequent blinking, may lead to even better results than predicted here.

The other two approaches relied on, respectively, instantaneous photo-induced fluorescence recovery after electron-induced switch-off, and electron-induced switch-on from a dark or dim to a bright fluorescent state. For the first approach, it is essential that the electron dose is set such that the fraction of molecules that remain on allows for application of localization microscopy. Thus, a careful estimation of initial molecular density based on the wide-field fluorescence images is needed together with electron dose calibration. Furthermore, we have found that the fraction of molecules that can be recovered versus those bleached after electron irradiation is a crucial parameter. For currently experimentally established values of 75% recovery, too many molecules are lost to give an improvement over the first approach using HAWK. Only for optimized molecules or recovery conditions leading to 99% or more photo-induced recovery, this approach would be a viable alternative potentially resolving, e.g. a 200 nm ring or 100 nm separated lines.

Electron-induced switch on circumvents the limitations of photo-induced recovery after electron switch off and could allow for results like established implementations of localization microscopy. Currently, only one fluorescent molecule, Alexa Fluor 594, is known to exhibit electron-induced brightening. Further screening for and development of electron-sensitive molecules that could be used as CLEM probes is thus highly recommended. An optimized probe would show a clear off-on switching and a prolonged on-state lifetime compared to the 0.7s used in this study. An alternative to the optimization of single fluorescent molecules for this purpose, would be the development of Förster resonance energy transfer donor-acceptor pairs or photoinduced-electron transfer pairs where the acceptor or quenching pathway is blocked after electron attachment. This would intrinsically lead to the desired dark-bright switching in the donor fluorescence channel and could be guided by screening known molecular pairs for low energy electron affinity.

4.5. Appendix

4.5.1. Expected number of unique localizations for electron-induced brightening localization microscopy

We can estimate the expected number of unique localizations as follows. The probability of localizing an individual molecule in an ensemble of N molecules after k cycles equals:

$$\begin{aligned} P(\text{localize molecule}) &= 1 - P(\text{not localizing the molecule}) \\ &= 1 - \left(\frac{N-1}{N}\right)^k \end{aligned} \tag{4.5}$$

By then using the linearity of expectation we can determine the expected number of unique localizations E[UL] by summing the individual expectation values, giving:

$$E[UL] = N\left(1 - \left(\frac{N-1}{N}\right)^k\right) \tag{4.6}$$

Finally, we should replace k with the expected number of times we switch on only 1 molecule. Thus, we need to multiply k in the formula above with the 24% probability of switching a single molecule on described in the text. For the different structures with 140 iterations for the spaced circles, 400 for the ring and 1000 for the crossing lines we expect respectively 30%, 32% and 20% of the total emitters to be localized.

5

Lifetime characterization of the electron-induced dynamics of perylene-diimide

In-situ fluorescence spectroscopy in a scanning electron microscopy has recently been shown as a powerful new technique to examine energetic electron – organic molecule interaction dynamics during and after electron irradiation. In this technique, fluorescent molecules report the presence of charge carriers in the sample via transitions between the bright, fluorescent, neutral molecule and dark, non-fluorescent, charged intermediates. Initial experiments revealed long lived (> 10 s) anionic intermediates. As these anion intermediates showed reversible charged-to-neutral reaction dynamics, evidenced in dark-bright fluorescence dynamics, further study of the time scales involved is relevant for finding ways to mitigate damage and charging in electron microscopy. Time scales below hundreds of milliseconds were however not accessible due to low excitation power and long camera integration times of the wide-field fluorescence microscope that was integrated in the SEM. Here, we use an adopted microscope set-up that allows higher power laser excitation and faster fluorescence detection using a photo-multiplier tube enabling sub-millisecond timescales. Irrespective of incoming electron energy, we observe an instantaneous drop in fluorescence emitted from perylene-diimide upon electron irradiation, followed by a gradual recovery of fluorescence. This recovery follows a double exponential behaviour characterized by time constants varying between 5-150 ms, and 200 ms – 2 s respectively. For 2 eV incoming electron energy, close to the resonance energy for direct electron attachment, we observe a reduction in the longer lifetime component. We discuss potential mechanisms that could be responsible for the observed double exponential recovery and give prospects for further studies characterizing electron-molecule interactions after electron irradiation.

5.1. Introduction

High energy radiation, such as (extreme) UV, X-ray, and keV electrons or protons, is used in many technological applications to modify or probe a sample via chemical changes induced locally in the sample. Applications include domains like lithography, microscopy, medical diagnosis, or nanofabrication. These chemical changes are often mediated by low-energy electrons (0 – 20 eV) generated in the sample by the impinging radiation through a variety of possible pathways. The vast range of potential pathways can lead to a plethora of end products, limiting the specificity to the desired induced chemical outcome [83–87]. Reactions induced by energetic electrons have been thoroughly studied by irradiating molecules in the gas-phase with electrons of energies up to a few eV. The resulting charged fragmented end-products are then detected and analyzed, providing a detailed map of chemical reaction products as a function of incoming electron energy [42, 44]. However, detection of reaction end-products leaves the underlying dynamics obscured. Furthermore, most of the technological applications including electron and (E)UV lithography, and radiation therapy, do not rely on molecules in the gas-phase. This makes that the surrounding molecular environment can also play a crucial role mediating different types of reactions and altering the course of chemical processes compared to gas-phase experiments [42, 44]. In-situ monitoring electron-molecule interaction dynamics in model samples could bridge the current gap between gas-phase studies and the relevant environment in applications.

Fluorescence microscopy integrated in a scanning electron microscope [11] allows in-situ visualization of the dynamics of electron-molecule interactions. Using a sample containing fluorescent reporter molecules that change their fluorescence emission upon interaction with low-energy electrons, the dynamics following electron irradiation can be monitored in the sample (Chapter 3). In our previous work, we used bright fluorescent molecules that became non-fluorescent upon transition to a charged (anion or cation) state. With this method, we observed reversible dynamics in the electron-molecule interactions taking place over multiple seconds timescale. We then studied the energy dependence of this reversibility by monitoring the initial decrease in fluorescence after irradiation versus the fraction of signal that recovered. We found that by quantifying these ratios as a function of electron energy, the reversible component can be explained by the formation of transient anions that neutralize through charge transfer to the local environment (Chapter 3).

The observed reversibility can have important ramifications for further scientific work. First, intervention with the reaction intermediates, e.g. favoring return back to the neutral state or accelerating charge transfer to quenchers or the ground electrode, could provide ways to mitigate damage, or, vice versa, direct damage to a wanted reaction product. We already obtained proof of principle using a fluorescent molecule with a photo-excitable anion, where anion excitation after electron irradiation was indeed found to accelerate fluorescence recovery. Second, the reversibility of electron-molecule dynamics as evidenced in a fluorescence bright-dark-bright transition could be interesting for developing superresolution fluorescence localiza-

tion techniques that can be combined with electron microscopy. In such techniques, electron beam irradiation would be used to locally switch molecules to a fluorescent dark state, and the gradual recovery of fluorescence could then allow retrieval of the locations of single fluorescent molecules like existing all-optical localization microscopy techniques [16, 17]. For both these applications, determination of the time scales involved in the reversible dynamics is clearly of relevance. Thirdly, determination of the time constant(s) involved in the observed fluorescence dynamics may provide further insight in the precise mechanisms at play. In fluorescence spectroscopy, analysis of time constants involved in fluorescence intensity fluctuations has in itself provided valuable insights in the type and number of processes involved in molecular relaxation after photo-stimulation [29, 107–115]. Quantifying the time constants underlying fluorescence dynamics after electron irradiation could thus gain further fundamental insights in electron-molecule dynamics occurring inside a sample. However, in our previous experimental work the temporal resolution for read-out of the fluorescence recovery after electron irradiation was limited, only allowing us to establish that processes could extend over a time scale of multiple seconds without the resolution to uncover the underlying time constants.

Here, we use a modified version of our integrated fluorescence and electron microscopy setup that includes a laser source and a point-detector to allow faster measurements after electron irradiation. We use this setup to characterize the time constants of the fluorescence recovery of the perylene diimide (PDI) molecule that we also used as a model system in our previous work. We show that we can sample the recovery dynamics down to the milliseconds regime, uncovering two typical exponential time scales involved in the recovery.

5.2. Methods

5.2.1. Fluorescence model sample

As a model fluorescent molecule we use N,N'-bis-propyl-1, 6, 7, 12-tetra-(4-tert-butylphenoxy) perylene-3, 4:9, 10-tetracarboxylic diimide (PDI) for which we've previously demonstrated long-lived fluorescence dynamics after electron irradiation (Chapter 3). We spincoat 10 µL of 60 µM PDI diluted in toluene at 2000 rpm on a microscope glass slide to obtain a homogeneous layer. The expected layer thickness is in the order of tens of nanometers. The side chains of our PDI molecule provide a steric repulsion preventing $\pi - \pi$ stacking and excimer formation. The microscope glass slide is covered by a 13 nm thick ITO layer which is again covered by a 10 nm thick Al_2O_3 layer deposited by ALD.

5.2.2. Integrated laser fluorescence and scanning electron microscope

We modified an existing high-NA fluorescence microscope integrated in a SEM [11] with a laser combiner and point detector to be able to detect millisecond dynamics.

An optical breadboard (Thorlabs) was mounted to a SECOM system (Delmic, Delft) attached to a Verios SEM (Thermo Fisher Scientific). The SECOM stage was modified to allow application of a retarding field for the electron beam with few eV landing energies as described previously [39]. The optical breadboard allows for plug-and-play placement of optical elements. An optical excitation path was added for a CFLEX C4 laser combiner (Hübner Photonics) with 405 nm, 488 nm, 561 nm, and 638 nm excitation wavelengths. For detection, we added a path to a photomultiplier tube (PMT) (Hamamatsu) connected to a DLPCA-200 amplifier (Femto).

Adding these two paths meant that we had to change the existing SECOM optical configuration. Both the fluorescence filters and tube lens were moved further away from the microscope objective lens. This allowed addition of a retractable mirror to select between two detection paths, one for a scientific Zyla 4.2 Plus CMOS camera (Andor) and one for the PMT (Fig. 5.1). The free-space laser is expanded 10x using a beam expander, reflected via a 409/493/573/652 nm quad-edge dichroic mirror (Semrock) and then coupled into the vacuum of the SEM via a mirror and a window separating ambient and vacuum. In the vacuum chamber, a 60x 0.95 NA plan apochromat optical objective (Nikon) focusses the light onto a sample.

Fluorescence is captured by the optical objective and follows the same trajectory back to the dichroic mirror, where it passes through, is filtered by a 600 nm longpass filter (Thorlabs FELH600) and is then focused on either the camera or the PMT. A retractable mirror is used to switch between the two detection paths. If the mirror is

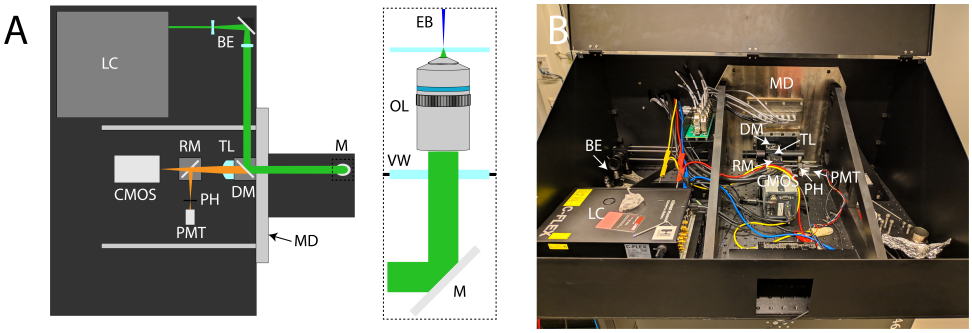

Figure 5.1: We modified a SECOM-door by mounting an optical breadboard to the microscope door for laser excitation and multiple optical imaging paths. (A) Schematic of the optical path used, a laser combiner (LC) of 4 different wavelengths passes through a 10x beam expander (BE) and is reflected by a mirror. A dichroic mirror (DM) is used to reflect the laser light into the conventional SECOM optical module. Here (inset) the light is reflected upwards by a mirror (M) to a vacuum window (VW) and is focused on the sample using a 60x optical objective lens (OL). Inside the vacuum, the sample can be exposed to a focussed electron beam (EB). The emitted fluorescence is caught by the OL, passes through the VW and is reflected by the mirror towards the DM. Here, the light passes through the DM and is focused by the tube lens (TL) on either a CMOS camera or PMT. We switch between these imaging paths using a retractable mirror (RM). We place a 200 µm pinhole (PH) in the optical focus before the PMT to filter most background light. (B) Photograph of the setup with multiple optical components indicated, the optical breadboard is encapsulated in a black box to exclude background light.

retracted, light is focused on the camera. Otherwise, light is focused on a 200 µm diameter pinhole before reaching the PMT to reduce background light. Switching between these two paths allows a combination of optical inspection of the sample, detecting fast fluorescence dynamics, and alignment between the electron beam and PMT.

The electron beam, the PMT and the camera are mutually aligned using cathodoluminescence (CL). CL is generated in the glass slide using a 10kV electron beam with 400 pA current. First, the pinhole is aligned along the optical axis (z-direction), such that the optical focus overlaps the pinhole position. For this, we scanned the electron beam across the sample and mapped the PMT signal to the electron beam location, effectively giving an image. We then moved the pinhole in z until we had a sharp image of the pinhole with the highest photocurrent. Next, we aligned the pinhole in front of the PMT in x and y directions such that the PMT signal corresponds to center of the camera. For this we first parked the electron beam at a single spot, and then moved this position until the corresponding CL spot was centered on the camera. Using this electron beam position, we again map the PMT signal to the electron beam position. We then center the image of the pinhole to the location of the electron beam corresponding to the center of the camera by moving the pinhole in x and y.

When varying the electron landing energy, the position of the electron beam with respect to the fluorescence microscope can shift. Therefore, after every change of electron beam energy, a small area of the fluorescence sample is scanned with the electron beam. This leads to local bleaching in the sample, which is imaged with the camera. We center this bleached area to the camera by moving the objective lens in the xy-plane. Since the PMT is centered to the camera sensor, the PMT and electron beam are aligned to each other as well. We also use this local bleaching at electron landing energies < 20 eV, where EM signal is generally lacking. By minimizing the local bleaching area we are able to focus the electron beam.

5.2.3. Electron exposure and fluorescence detection

Fluorescence dynamics of PDI is detected by continuously monitoring the fluorescence signal while performing a near-instantaneous electron irradiation. For this we continuously excite the fluorescent sample using a 561 nm excitation wavelength at 25 mW laser power while we detect the fluorescence signal using the PMT. The PMT signal is amplified with a DLPCA-200 V/A amplifier, with a 10^7 amplification and 50 kHz bandwidth. The voltage is additionally filtered with a 1st order low pass RC-filter with 50 kHz cutoff frequency. Finally, the voltage was readout using a National Instruments DAQ with a readout rate of 1 MHz.

In the experiments, we want to quickly expose part of the sample to electron irradiation and then detect the fluorescence response. With the 50 kHz bandwidth and MHz readout rate we can detect fast electron induced-dynamics. However, this

also means that the electron beam exposure needs to occur fast, but with sufficient dose to detect changes in fluorescence signal. Since our electron microscope is not equipped with a fast blanker, we cannot obtain a quick single spot exposure centered to the PMT. Instead, we scan a line through the area detected by the PMT. However, as we move across the sample the alignment between the camera, PMT and electron beam might change. To reduce the number of times we need to re-align, we scan 3 equally spaced lines with the electron beam. In case one of the scan lines moves out of the field of view of the PMT, another one moves in.

Scan lines are 10 µm long and scanned with a 1 keV primary beam energy at 3.2 nA current using a 20 nm pixel spacing and 200 ns dwell time. This results in a local dose of approximately 10 e^-/nm^2 where each line takes approximately 100 µs to scan. Considering the 200 µm sized pinhole in front of the PMT and the 60x magnification, the detected electron exposure lasts approximately 33 µs. Besides 1000 eV, landing energies of 50 eV, 20 eV, 10 eV and 2 eV are used by setting a corresponding retarding field on the sample stage. We note that at this high beam current, the electron beam monochromator in our SEM cannot be used, giving us an electron energy spread of roughly 1.2 eV [39]. For all landing energies, we used a 4 µm line spacing except for 2 eV where we used a 5 µm spacing to decrease the likelihood of overlap of neighboring lines in the field of view of the PMT because of additional defocus of such a low-energy electron beam.

5.3. Results

5.3.1. Temporal dynamics of fluorescence recovery after electron exposure

Fluorescence from the PDI sample is continuously monitored before, during, and after electron irradiation (Fig. 5.2A). Camera images acquired with a 10 ms exposure time show the laser-excited area on the sample (Fig. 5.2B-I). Immediately after exposure, the three scan lines of the 1 keV electron beam are clearly visible on the camera due to fluorescence darkening induced by the electron beam (Fig. 5.2B-II). After irradiation, we observe a partial recovery of fluorescence intensity in all three scan lines (Fig. 5.2B-III). The PMT collection area overlaps with the center scan line as indicated in Fig. 5.2B. Indeed, on the PMT, we observe an instantaneous drop in fluorescence signal after electron exposure (Fig. 5.2C) corresponding to our estimated 33 µs exposure time of the PMT collection area. Moreover, confirming the camera observations and our previous results (Chapter 3), a partial recovery of fluorescence is evidenced, which extends over several seconds time scale. Importantly, the PMT measurements show that this long time-scale recovery is comparatively slow and that fastest recovery takes place on the smaller time scales shortly after irradiation. We next focus on characterizing the time scales involved in this recovery.

Before quantifying the temporal evolution of fluorescence recovery, we first correct for photobleaching, which is evidenced in Fig. 5.2C by the gradual decrease in

fluorescence intensity prior to electron exposure. First, we manually determine the time stamp of electron irradiation. We then determine the photobleaching rate by fitting a single exponential term to the fluorescence signal prior to electron irradiation. This typically gives a photobleaching lifetime of about 30 s. To correct for photobleaching, the fluorescence signal is divided by the exponential decay defined by the photobleaching lifetime. We then extract the recovery part of the corrected fluorescence trace for further analysis. For this, we normalize the amplitude of

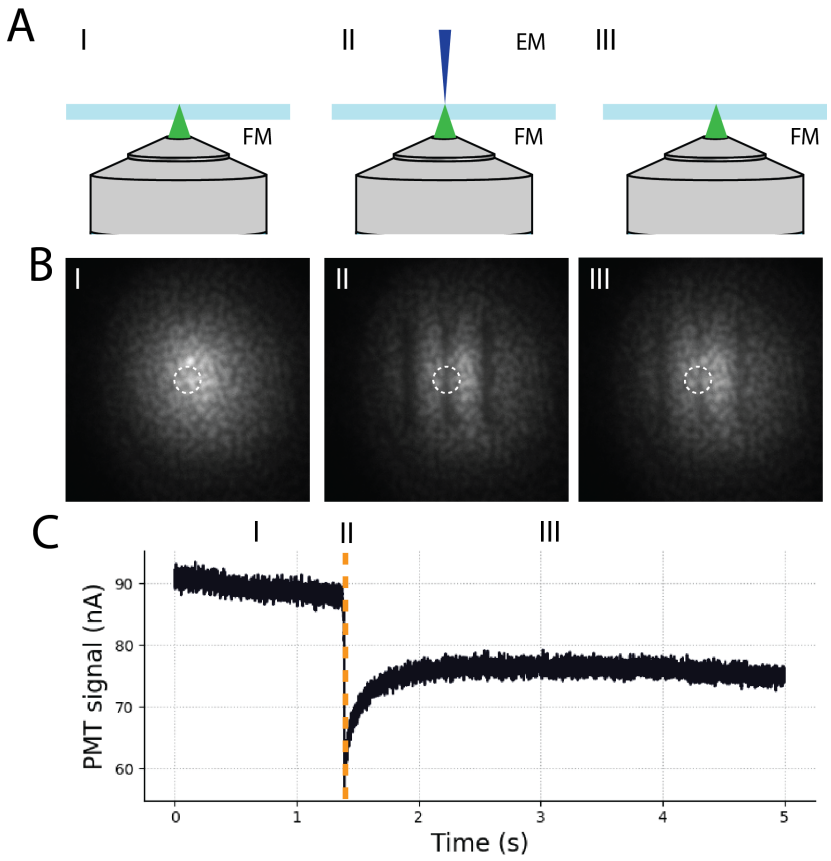

Figure 5.2: (A) We continuously excite and monitor the fluorescence (I) before, (II) during and (III) after electron irradiation. We expose the sample to electrons by scanning 3 spaced lines of 10 µm length with a 3.2 nA electron beam and 200 ns dwell time for a near-instantaneous decrease in fluorescence. (B) Camera images acquired with 10 ms exposure time (I) before, (II) immediately after and (III) 4.1 s after electron irradiation show a recovery in fluorescence signal. A small region (dashed circle) is detected by the PMT. (C) The fluorescence intensity given by the PMT current as a function of time. The detected fluorescence shows a slow decrease caused by photobleaching, followed by a rapid decrease in intensity caused by electron exposure (dashed orange). After the exposure, the fluorescence recovers partially with a seemingly fast and slow component. The data was smoothed using a 3rd order Savitzky-Golay filter of windows size 0.5 ms.

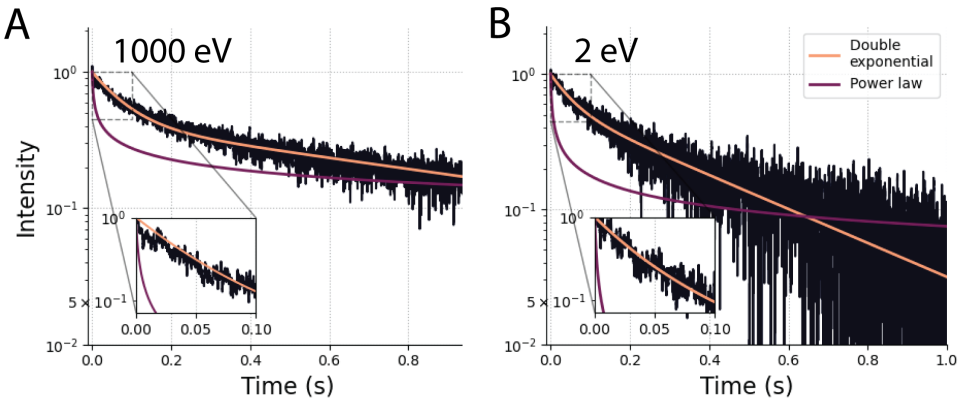

Figure 5.3: We plot the fluorescence recovery after electron irradiation as a decay on a log-lin scale and determine timeconstants for multiple exponential decay functions and power laws for (A) 1000 eV and (B) 2 eV landing energy. For 1000 eV, we observe both a fast and slow component in the fluorescence recovery. We confirm this by fitting two independent exponentials, which fit closely to the data even for the first 100 ms (inset). For 1000 eV we find lifetimes of 78 ms and 1069 ms. At 2 eV, the slow component disappears, yet we still find that the data shows at least 2 exponentials. Here we find lifetimes of 53 ms and 350 ms. Power law fitting of the form $\frac{(t+10^{-3})^x+c_1}{10^{-3}+c_1)}$ was attempted, but does not describe the data. A 1ms delay was based on the averaging window and used to normalize the data. Data is smoothed using a Savitzky-Golay filter.

5

the fluorescence recovery from 0 to 1. After these corrections, the resulting values now no longer show photobleaching and have comparable amplitudes between different measurements. Fitted time constants in the fluorescence recovery can then be quantified such that they can be compared between different measurements.

We observe a double exponential fluorescence recovery after the 1 keV irradiation. (Fig. 5.3A). For the slow recovery component, we find a characteristic time constant τ_2 = 1.069 s. This component is thus responsible for the long timescale behavior observed in our previous work. Next to this, we see that the faster recovery is also characterized by an exponential increase, here with a lifetime of τ_1 = 78 ms. Furthermore, a slight deviation in the first 100 ms can be observed and suggests even faster dynamics are at play. We decided however to not fit a third exponential term since there are too few data points to reliably extract a potential shorter timescale lifetime. In our prior work on PDI, we found the slow recovery to disappear when changing the electron landing energy to the few-eV domain where the number of possible electron-induced reaction pathways becomes limited. Therefore, we next characterize the fluorescence recovery dynamics for landing energies down to a few eV.

5.3.2. Fluorescence recovery at few eV electron landing energy

When the electron landing energy approaches values of only a few eV, the number of possible electron-induced reaction pathways gradually becomes less [42, 44]. Specifically, around 2 eV, only electron attachment remains available as the primary electron-molecule interaction step (Chapter 3). Therefore it is likely to expect a gradual shift in the fluorescence recovery lifetime(s) when reducing the landing energy from 1000 eV to 2 eV. Thus, we lowered the electron landing energy to 2 eV and repeated the experiment to acquire the time-dependent fluorescence recovery. The fluorescence recovery signal after 2 eV exposure (Fig. 5.3B), reveals that the timescales of the recovery shifted and that the lifetime of the slow recovery component is reduced. However, despite the reduced number of pathways, we still observe that the data do not follow pure single exponential behaviour. When fitting a double exponential recovery we find time constants of 53 ms and 346 ms.

We next quantified the fluorescence recovery rate for intermediate electron landing energies of 50 eV, 20 eV, and 10 eV. Figure 5.4 shows the time constants resulting from double exponential fitting of the recovery for all five landing energies. For the fast exponential term (Fig. 5.4A), we find that the time constants range between 10 ms and 125 ms, except for the measurements performed at 1000 eV. Here we find that the time constants are all higher with values ranging from approximately 75 ms to 175 ms. For the slow term in the fluorescence recovery rate, we observe an overall increase in the rate between 1000 eV and 2 eV, but a large range of values for 50 eV to 10 eV. This could be caused by incorrect correction for the photobleaching, leading to an effectively slower fluorescence recovery rate when fitting. This effect can occur at any electron landing energy, but will be more pronounced for 50 eV to 10 eV due to the lower decrease in fluorescence after electron irradiation (Chapter 3). Slight errors in the photobleaching correction are then still relatively large with respect to the decrease in fluorescence resulting in longer extracted recovery lifetimes than those that actually occur. Nevertheless, between 1000 eV and 2 eV we find that the fluorescence recovery rate clearly has increased for the slower term. This transition in recovery rate could mark an overall change in the fluorescence and charge dynamics in the sample.

5.4. Discussion

Our results have indicated a double exponential process in the recovery of fluorescence on the 1 - 10^3 ms time scale after electron-induced darkening. Slight deviations in the double exponential fit for times close to 1 ms after exposure may hint at even faster dynamics taking place at even shorter time scales. The double exponential behavior indicates multiple processes contributing to the physics of fluorescence recovery. In fluorescence microscopy, multiple lifetimes in the recovery from (photon-induced) dark states have been observed and attributed to diverse processes including long lived non-fluorescent triplet states and dark anionic states [29, 108–111, 113, 114, 116]. A few observations need to be made with respect to the

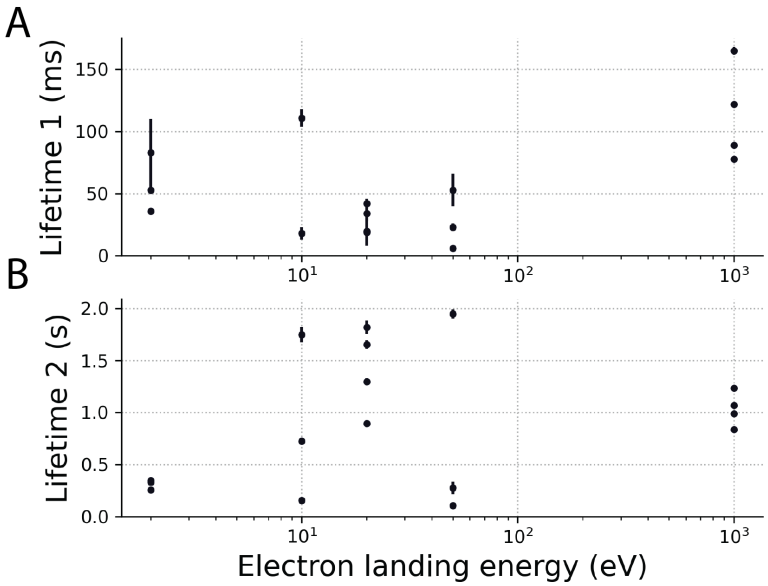

Figure 5.4: Lifetimes of the fluorescence recovery for different electron landing energies found by fitting two independent exponentials. (A) The lifetime of the fast component varies across the electron landing energies, but is generally found to be higher for an electron landing energy of 1000 eV. (B) The lifetime of the slow component decreases between 1000 eV and 2 eV. For 50 eV, 20 and 10 eV we find a large range in the lifetimes. Yet for 2 eV we observe the lifetime to decrease to hundreds of milliseconds.

comparison between our experiments and dark state recovery or blinking dynamics in regular fluorescence microscopy. First, our observations relate to the behavior observed directly after electron exposure, while photon-induced dark states contribute throughout the entire fluorescence time trace. In our previous experiments, we also demonstrated that exposure-induced electron attachment, and thus formation of dark anions followed by charge dissipation, forms a major contributor to the observed darkening and recovery (Chapter 3). Second, in fluorescence microscopy, the molecule is resonantly excited by photons matching the energy gap between specific molecular levels. In our experiment, the incoming electron typically carries much more energy leading to a wider range of potential physical processes taking place in the sample that could affect the fluorescence molecule. Third, in photon-induced dark state population, the fluorescent molecule is directly excited and dark state dynamics relies on internal excited state dynamics and/or interactions of the excited molecule with its local environment. In our experiments, the darkening can occur either via direct interaction of the fluorescent molecule with the incoming electron or indirectly via migrating electron-scattering products generated in the wider sample environment. Finally, we quickly inject charge into the sample or create a cloud of separated charge carriers in the sample due to scattering of incoming high energy electrons, thus creating a temporary out-of-equilibrium situation in the sample that will relax after the electron exposure. Thus, the occurrence of two, or including

smaller timescales potentially even more, processes contributing to the observed recovery, is plausible.

We note that in fluorescence blinking and, e.g., also in the analysis of phosphorescence lifetimes, multi-time scale behavior described by power-law dynamics has also been observed. This is typically attributed to the existence of multiple relaxation pathways occurring on broadly distributed timescales or with time-varying lifetimes that can fluctuate over many orders of magnitude [92, 115, 117]. However, we do not find a clear indication for power law dynamics in our data (Fig. 3) and the inclusion of even smaller time scales would be needed to have a sufficiently broad temporal range to probe potential power-law dynamics. We also do note that temporal averaging, i.e., the observation of multiple exponents because of a time-varying single-exponential process as may occur in long-lasting fluorescence or phosphorence experiments, does not occur in our experiments. On the other hand, spatial averaging, i.e. multi-time scale behavior arising from sampling many molecules which each have a distinct recovery lifetime, does take place in our situation.

For an electron landing close to 0 eV, the situation may be less complex compared to the higher electron energies as in this case only electron attachment and non-damaging excitation of the PDI by inelastic scattering are believed to remain available pathways [42, 44]. Yet even in this regime, multiple relaxation/dissociation paths could be available. Increasing the electron landing energy can lead to additional types of electron-molecule interactions resulting in more complex dynamics. So, the two lifetimes observed for 2 eV electron landing energy could relate to electron detachment of the dark anions formed by electron attachment and de-excitation of a transient dark state formed after inelastic scattering. De-excitation of electronic excitations induced by the incoming electron typically occur in the order of 10^{-16} s, unobservable in our experiments [42, 44]. Excitation to a dark triplet state could occur, and while triplet lifetimes are typically reported in the microsecond regime [107, 108, 111, 112] the absence of oxygen in vacuum could lead to prolonged triplet lifetimes extending to ms time scale [118]. We expect that electron excitations should not change the odds for a forbidden spin transition since these are regulated by molecular oxygen and/or spin-orbit coupling. Both of those factors remain unchanged with electron excitations. Hence, we believe that excitation of the molecule by inelastic scattering is not the cause for the observed effects. Rather, the electron detachment process for dark anions could in itself already give rise to multi-time scale behavior through its interaction with the sample environment.

Anion electron detachment could first of all occur via the sample substrate, i.e. charge transfer at the PDI-Al_2O_3 interface, or at the PDI-vacuum interface (Fig. 5.5A). Depending on the PDI sample thickness, two quite distinct exponentials could be observed each indicative of charge dissipation at either side. Charge transport along the PDI-Al_2O_3 interface would most likely occur through trap states in the Al_2O_3 since the band gap of amorphous Al_2O_3 is expected to be about 6.2 eV [119]. Transfer to these trap states could take a very long time and thus

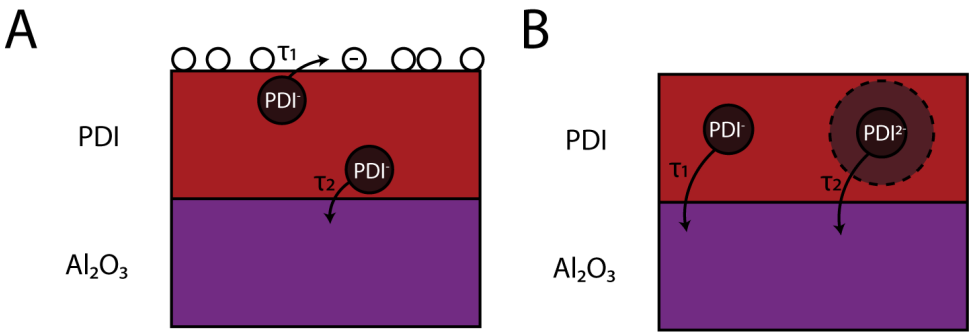

Figure 5.5: here are multiple explanations for the 2 independent exponential terms for the fluorescence recovery at landing energies of 0 eV. (A) Dark PDI anions can neutralize by transferring electrons to adsorbates at the PDI-vacuum interface with lifetime tau_1 and electron transfer at the PDI-Al_2O_3 interface resulting in two different fluorescence lifetime in the recovery. (B) Dark PDI anions and dianions neutralize by electron transfer at the Al_2O_3-interface with different lifetimes τ_1 and τ_2. The PDI dianions absorb the fluorescence of the surrounding neutral PDI molecules. These quenched molecules recover once the dianion transfers a single electron. Furthermore, due to the quenching, the dianion gets excited by the neutral molecules increasing the rate of electron transfer of the dianion.

5

be responsible for the dynamics extending over tens of seconds [120]. Meanwhile, electron transfer between the PDI vacuum interface could be mediated by absorbants or trace water in the SEM vacuum chamber. We note that both transfer rates could be enhanced due to the continuous optical excitation [121]. Thus, the electron transfer mechanisms from PDI anions to the environment could give rise to the observed multi-exponential dynamics.

An alternative mechanism that could give rise to two lifetimes could be electron detachment of the anion and dianion (Fig. 5.5B). Both states are dark but the dianionic state of PDI overlaps with the emission spectrum of the neutral PDI species [89]. This means that (i) the dianion can quench the fluorescence of nearby neutral species and (ii) the dianion is then effectively excited resulting in a faster electron detachment. The dianion to anion transition is a transition between dark states but as the dianion quenches part of its environment neutral PDI molecules may reappear bright resulting in a partial recovery of the ensemble fluorescence intensity. Because of the dianion excitation this process may occur faster than the neutralization of the anion, giving rise to the two distinct lifetimes. Comparative experiments at lower PDI concentrations to prevent neutral dye-dianion energy transfer could investigate this scenario but would require a more sensitive photon detector. Alternatively, experiments with another fluorescent molecule without dianion absorption could also be investigated. This could then lead to a single exponential behaviour if this is the mechanism at work.

With increasing electron landing energy, more electron-molecule interaction pathways and hence more potential excitation or intermediate species become available, more inelastic scattering events will occur, and the penetration depth of the electron beam will increase. This will increase the complexity of the fluorescence recovery

dynamics in the sample. Nevertheless, we find that with increasing beam energy one of the time constants stays roughly around 100 ms. Thus, this process in the recovery dynamics seems unaffected across the different electron landing energies. This could be an electron detachment pathway for the dark transient anions as discussed above. For the seconds time scale process our data seems to indicate a marked difference between the 2 eV results and the 10 eV and higher landing energies. While for 2 eV the second lifetime is consistently around 350 ms, for the higher energies lifetimes in the order of seconds appear. This could be indicative of higher energy scattering mechanisms, of which some can lead to the formation of cationic species in addition to the (di)anions formed at 2 eV. This PDI cation could exhibit a longer relaxation time. Alternatively, the increasing penetration depth of the incoming electron beam could lead to occupation of trap states in the Al_2O_3 layer or different charge distributions within the perylene layer, which could limit electron transfer from PDI anions to Al_2O_3.

One of our main interests in temporarily darkening the fluorescence by electron-beam exposure is in the development of electron-beam induced superresolution fluorescence localization techniques. The long time-scale recovery dynamics is beneficial for localization as ideally only one molecule recovers with a diffraction-limited sample area within a camera observation time. The occurrence of multi-exponential dynamics and the indication that an even faster component than what could be measured here, is present, thus forms a limitation. At electron landing energies above 2 eV the dark state lifetime increases, but this is accompanied by bleaching of the molecules (Chapter 3). Most of the emitters would then be lost before they can be localized. The multiple lifetimes observed at 2 eV suggest that multiple reaction relaxation pathways remain. This could be troublesome, as you would ideally have control over these induced dark states and multiple processes are more difficult to control. On the other hand, the fast setup and laser illumination will also allow for faster detection of switching emitters.

The multi-exponential fluorescence recovery uncovered here is indicative of complex sample and electron-molecule dynamics that should be investigated in more detail. Further examination of the recovery after close to 0 eV electron irradiation is best targeted first. Our work suggests three different ways to obtain a further understanding: (i) improve the setup for detecting even faster fluorescence dynamics, (ii) explore sample preparation parameters like fluorophore concentration and different substrates, and (iii) detect absorption spectra during the dynamics. For detecting faster dynamics with better SNR, we propose to use an avalanche photodiode instead of a PMT. In addition to this, a fast beam blanker could be used to perform electron irradiation in less than a nanosecond to further study molecular dynamics [52]. More sensitive detection will allow reducing the concentration of PDI to a monolayer, preventing the neutral dye quenching by dianions. Moreover, if there are different transfer mechanisms along the vacuum or Al_2O_3 interfaces, such a reduction in concentration would favor the faster process of these two. Thus, the fluorescence recovery would then reduce to a single exponential. The lifetime of this recovery could then be manipulated by either changing the laser power, such that

the conductivity of the Al_2O_3 would be altered or by repeating the experiments on substrates with different conductivity. Alternatively, one could attempt to measure the sample current as a function of time. However, these currents are extremely small and must be measured on millisecond timescales while a kilovolts stage bias is applied, which is extremely challenging. Another parameter that could affect the fluorescence recovery rate would be to excite the anionic PDI species. This could drastically alter the recovery rate, but not for dianions and cations and could thus also be used to investigate the role of cation formation at higher energy irradiation. Manipulation of generated excited states could further be explored with alternative dyes with specific characteristics such as the Rhodamine dye with near-UV excitable anion we used previously. All in all, the wide range of fluorescence techniques, tools, and dyes with specific characteristics that have been developed over the past decades for fluorescence microscopy, offers many possibilities for further investigating and manipulating electron-molecule interaction along the lines of these first experiments.

5.5. Conclusion

In conclusion, we have used a modified version of our retarding field integrated light and electron microscope to perform measurements on fluorescence recovery dynamics after low-energy electron irradiation induced darkening. We performed experiments at different landing energies and found that for all examined electron landing energies in the range of 2-1000 eV the fluorescence recovery follows multi-exponential dynamics with components in the 10-100 ms range and around 1 s. Interestingly, the latter process seems to occur faster at 2 eV landing energy compared to larger energies. We discussed several scenarios that could be responsible for these observations and sketched directions for further research.

6

Conclusion and Outlook

6.1. Conclusions

The goal of this thesis was to explore the possibility of manipulating fluorescent molecules with low-energy electron for superresolution microscopy for integrated microscopy. To realize this, fluorescent molecules had to be monitored in-situ after electron irradiation with few eV landing energies. Using a retarding field, combined with an electron beam monochromator we've shown in chapter 2 how to achieve electron landing energies of only a few eV with an energy spread of 0.8 eV in a commercially available setup.

Using the integrated setup with retarding field, we exposed several fluorescent organic molecules to electrons of a few eV while detecting the fluorescence in-situ using the integrated optical microscope. We found, as presented in chapter 3, that perylene diimide started to show a remarkable return of fluorescence in time after initially switching of caused by electron irradiation. We found that electron-attachment was the main contributor for the reversible dynamics as the fraction of turned off molecules that recovered reached near-unity when the landing energies where close to 0 eV. Using electron attachment, we then demonstrated instantaneous reversible switching of electron-induced dark states on rhodamine B isothiocyanate and on-switching of Alexa Fluor 594. Inducing these temporary states using electron-attachment has key benefits compared to most other electron-induced processes. First, electron attachment is a resonant proces. This means that only at specific electron landing energies we have a large cross-section to induce the desired process. Furthermore, since electron attachment typically occurs at only a few eV, most other dissociation processes are excluded. Thus, the odds of inducing undesired effects should be low. Based on these finding, electron-attachment could be a viable method for stochastically inducing specific dark states in organic fluorescent molecules, which in turn could be used for localization microscopy.

Using the observations found in chapter 3, we studied how low-energy electron irradiation could be utilized for localization microscopy in the vacuum of an electron microscope. In chapter 4, we found that to obtain resolutions of tens of nanometers, fluorescent dyes need to be optimized such that they efficiently switch back and

forth between dark states after electron irradiation. Since, as of yet, there are not many alternative methods available that return the same resolution in the vacuum of an electron microscope [33, 34, 36], the low energy electron-irradiation could become a viable alternative method if dyes could be optimized further.

To further understand the underlying dynamics, we modified our integrated microscope setup further to increase the signal and the detection rate of the optical setup in chapter 5. With this setup we characterized the lifetimes of the fluorescence recovery in the millisecond regime down to 0 eV. Here we found that even close to 0 eV, the electron induced fluorescence dynamics cannot be described by a single type of process. This means that inside the sample, complex dynamics occur post electron irradiation. Studying these dynamics further in different settings can give new promising insights in understanding electron-molecule interactions.

From the work presented throughout this thesis can conclude that low-energy electron irradiation could become an alternative method to stochastically induce fluorescent dark states in vacuum for localization microscopy. However, for the technique to become viable, further research needs to be performed. Suggestions for further research will be discussed in detail in the outlook section below.

Our findings are not necessarily limited in their application to superresolution microscopy for integrated microscopy alone. We have shown in chapter 2 how the application of a retarding field can be a viable method in correlative microscopy, as it significantly enhances the electron microscope's weak signal of tissue sections optimized for correlative microscopy. This retarding field can also be utilized to decrease the acquisition time in large scale electron microscopy by a factor of 20 [79]. In-situ detection of fluorescence dynamics after low-energy exposure could grant new insights in electron-molecule interactions. Typically, electron-molecule interactions are studied by exposing molecules to electrons of a specific energy and detecting the generated charged fragments. This means that (i) the underlying dynamics remain hidden and (ii) neutral fragments cannot be detected. With further development of the method discussed in chapter 3, we could provide information of both. This could in turn have an impact for electron microscopy, EUV lithography and radiation therapy. In conclusion, further research in the subjects presented in this thesis do not have to be limited to superresolution microscopy alone. As we have shown, further research can have an impact in other fields as well.

6.2. Outlook

Throughout this thesis we have shown how low-energy electron irradiation of fluorescent molecules can induce dynamics to the fluorescence that can be utilized for superresolution fluorescence microscopy in integrated correlative light and electron microscopy (CLEM). Some of the approaches presented need further research, while others are closer to implementation. Here, based on the findings of this thesis, we will discuss the next steps that are needed for implementation of electron-beam

induced superresolution microscopy, and considerations for additional research and optimization for electron-beam induced superresolution microscopy in CLEM.

The first step, that is close to implementation, is to build an integrated setup suitable for localization microscopy. The setup discussed in chapter 5 has a powerful laser source and a sensitive camera, but small additional changes to the laser path to reduce laser speckle and to obtain a uniform illumination profile need to be made to achieve an optimal signal-to-noise ratio. Additionally, stage drift and vibrations need to be carefully characterized and minimized. With such a setup, first steps towards localization microscopy could be made by performing superresolution imaging without any electron irradiation using HAWK. With TRITC, being a bright fluorescent dye that shows blinking in vacuum and being a dye used for biological labelling [100], HAWK could be used to improve the resolution of the optical microscope to roughly 100 nm. A sample suitable to demonstrate this could be zebrafish insulin granules labelled with TRITC and can be compared to the simulations performed in chapter 4. By performing this experiment, we would have a first verification of an integrated microscope setup suitable for superresolution microscopy in our lab. To achieve higher resolution, more understanding is needed of the interaction between electrons and organic fluorescent dyes and fluorescent probes for superresolution imaging need to be developed.

6.2.1. Understanding electron-molecule interactions of fluorescent dyes

While we have inspected the changes in the electron-induced fluorescence dynamics of multiple fluorescent dyes, most of the chemical information such as the final reaction products remain hidden. Ideally, we would like to know what the final reaction products are for each electron energy so that we can narrow down the chemical reactions that occur post-electron irradiation. This in turn, could provide information about the chemical groups and reactions that are relevant to the observed dynamics such that fluorescent dyes could be further optimized. By studying the different dyes discussed in chapter 3 using a crossed molecular beam apparatus, or an electron stimulated desorption setup [42], chemical data complementary to the reported fluorescence dynamics can be acquired. This could provide insights into the final bleached or brighter reaction products formed for Rhodamine B ITC (RITC) or Alexa Fluor 594 (AF594), respectively. With this information, fluorescent dyes could be synthesized with a reduced cross-section of the bleached product for RITC or an increased cross-section of the brighter product for AF594.

By studying the fluorescence dynamics after electron irradiation in more detail, we may identify the relevant physical processes occurring at these timescales. Identifying these is important for performing localization microscopy (LM), since the duration of the dark or bright states will define the feasibility of different LM techniques. If we identify the lifetimes of the fluorescence dynamics after electron irradiation, as done in chapter 5, different processes could be distinguished. For

detailed suggestions on how to further identify these processes with experiments we refer to the discussion of chapter 5 in this thesis. Once the relevant physical processes are identified we could think of ways to manipulate these such that they occur at the optimal timescales for LM.

6.2.2. Developing efficient electron-switchable fluorescent probes

In chapter 4 we found that for electron-induced superresolution, the electron induced switching efficiency of different probes needs to be improved. Switching dark molecules with (low energy) electron irradiation would be the strongly preferred method of choice for this. However, as of yet, we have not found an optimal dye where 100% starts off in a dark state and then switches on after electron irradiation. Therefore, an important direction of research is the development of efficient electron-switchable fluorescent dyes.

Quenching dye pairs are ideal candidates for efficient electron-switchable fluorescent probes. If the quenching molecule of the pair is more susceptible to being chemically altered after electron irradiation, we can expect the quenched molecule to light up after electron exposure. For this, processes already studied in detail in fluorescence spectroscopy like Förster resonance energy transfer (FRET) or photoinduced electron transfer (PET) could be used. For chemically changing the molecule, different electron-molecule dynamics could be utilized. We propose to use electron attachment of the quencher-molecule to a transient charged dark state to stop the quenching process. Since electron attachment is a resonant process it can be controlled using the electron landing energy. The negatively charged quencher product could then either neutralize through the environment or dissociate to switch on the molecule temporarily or permanently, respectively. This means that the quencher molecule should have a higher electron affinity than the quenched molecule, to ensure that the quencher becomes negatively charged. Another important requirement is that both molecules should preserve their fluorescence throughout the EM sample preparation. Alternatively, you could use anti-body labeling. In that case, you'd need water solubility or at least the opportunity to bind to an antibody or another 'linker' molecule of which the construct is water soluble.

By in-situ monitoring the change in fluorescence intensity after electron irradiation of different dye combinations we could screen for suitable quenching dye pair candidates. Solutions of two dyes, dissolved in 1:1 ratio, where one should quench the other could be deposited at both high and low concentrations. Since both PET and FRET only occur when the dye combinations are in a vicinity of less than a few nanometres of each other, we would only expect the quenching to occur for samples where high concentrations of the dyes are present. Thus, only for those samples we would expect the quenched dye to light up after low energy electron irradiation. Dyes could then be screened based on relative increase in fluorescence and the reversibility of the on-switching process. To further confirm that quenching is the main cause, the emission spectra before and after electron irradiation should

be measured. If a shift in the peak ratio is observed, where the spectrum of the quenched dye increases and the quenching dye decreases, a halting of the quenching process would be confirmed. Such an experimental approach would be easy to implement in our current setup. Another benefit is that simple solutions would suffice for such a screen, obviating the need for more complicated synthesis of dye pairs for the screening process. In the end, fluorescent molecular pairs could then be developed that would switch on after electron irradiation with high efficiency.

6.2.3. Electron-induced superresolution microscopy on biological specimen

When trying to perform electron-induced superresolution techniques on biological specimen, the specimen itself could impose several issues that should be investigated beforehand. First and foremost, throughout this thesis, we used Al_2O_3 as an insulating spacer separating the fluorescent molecules from the grounded conductive ITO substrate. When trying to perform electron-induced superresolution on biological tissue, which is embedded in plastic, the conductivity of the sample and distribution of trap states could drastically change the lifetime of transient electron-induced states. This in turn, could affect the pathways fluorescent molecules undergo after electron irradiation. Thus, experiments performed on Al_2O_3 for dyes such as RITC or AF594 should be repeated on bare tissue sections to see how the processes change due to the change in conductivity. In addition to this, water molecules that remain after sample preparation of biological specimen could also act as an electron acceptor in the specimen. This might give rise to different induced dynamics, and even chemical processes occurring inside the sample that could further complicate the electron-induced chemistry of fluorescent molecules.

Another issue that might arise is charging of the specimen, causing the electron landing energy to change throughout the experiments. For typical experiments, this charging of the specimen is small compared to the electron landing energies of several keV used in EM imaging of tissues and is therefore negligible. However, at our landing energies close to 0 eV this might drastically change, as charging of only a few volts could have a significant effect on the electron landing energies. We performed some preliminary experiments to detect charging of the specimen at very low electron landing energies using the reflection-based technique discussed in chapter 2. By quickly sweeping the retarding field around the point of reflection, and simultaneously detecting the in-column detector signal for a focused spot, we attempted to detect a shift in the point of reflection for different dose on glass substrates [122, 123]. Our preliminary experiments where however troubled by electrical interference and deflection of the beam away from the in-column detector due to non-uniform charging of the specimen. We note however that on glass substrates a large amount of charging will occur in very short timescales. Therefore, it would still be worthwhile to repeat these experiments on bare tissue sections. If this approach works, and the point of reflection can be accurately determined, charging calibration curves need to be acquired for the charging tissue sections, like

Thete et al. [124]. Then for experiments on tissue sections, the retarding field needs to be dynamically altered to keep the electron landing energy stable.

Finally, we note that at electron landing energies in the range of keVs, tissue sections start to fluoresce due to electron irradiation [41]. This electron-induced fluorescence of the tissue will result in an increasing fluorescence background signal that will worsen the resolution of the localization of emitters. This effect could be significantly less at few eV electron landing energy, since fewer reaction pathways that could cause this fluorescence become available. Therefore, the electron-induced fluorescence of tissue should be investigated at low electron energy as well. In case fluorescence is still induced, even close to 0 eV, dose limitations that could ultimately limit the resolution of the superresolution techniques discussed in chapter 4 have to be considered.

6.2.4. In-situ tracking of chemical changes

So far, we have irradiated fluorescent molecules and tracked their direct response to the electron irradiation. This gave insights in reversible dynamics as discussed in chapter 3, but also in charge migration far beyond the scales of electron scattering models. [40] However, an application of fluorescent probes on the long term would be to track electron-induced chemical changes in different samples cause by high-energy electron irradiation. With different dyes lighting up based on the type of electron-molecule interaction, information can be obtained about the spatial energy distribution of scattered electron inside the sample. Information would even be provided by electrons at energies close to 0 eV, where currently most electron-scattering models have a difficult time to predict the scattering. Thus, similar to how fluorescent molecules have been used in biology to detect local biomolecular information, fluorescent probes could potentially be used to detect specific 'electro-molecular' information.

Electron-induced chemical changes could also be tracked by distinguishing between different electron-induced fluorescence dynamics in time. Similar to the experimental approach presented in chapter 5, temporal dynamics could be distinguished at faster timescales. Using a fast electron beam blanker [52], in combination with an avalanche photodiode, processes can be detected at even faster timescales up to the nanosecond regime. At these timescales, it would be possible to distinguish between different (dissociative) electron attachment events [42, 44]. Furthermore, with a dye where the neutral and anionic species would be detectable in different fluorescence channels, we could be able distinguish between neutral dissociative and dissociative electron attachment events in time. Neutral dissociation would lead to a permanent loss of fluorescence in both channels, while dissociative electron attachment would lead to a permanent decrease in one and temporary increase in another channel until dissociation occurs. With this approach, a further understanding of electron-molecule interactions occurring inside a sample could be achieved.

All in all, first steps in a new field of correlative fluorescence-electron spectroscopy have been made. This experimental approach could lead to breakthroughs in different technological applications, such as superresolution microscopy in integrated CLEM systems. Nevertheless, many more challenges await before an optical resolution of tens of nanometres can be realized in an integrated microscope. A considerable amount of research can be conducted in this direction, but other applications such as understanding electron-molecule interactions in biological specimen await as well as sketched above giving many avenues for future follow-up research.

Acknowledgements

Over the course of almost 5 years, I've been lucky enough to meet tons of people who all helped me in their own way to complete this thesis and create wonderful memories in the process. This might have been by direct contributions to this work or indirect by having discussions about other topics, inspiring me with clever ideas, sports, or late-night adventures. Thank you to who recognizes him- or herself in any of these descriptions.

I am sincerely grateful to have Jacob Hoogenboom as a promotor and supervisor, but also as a mentor. Without your mentorship I wouldn't have been able to have become the researcher I am today. During the PhD you've have been able to push me out of my comfort zone by working on this multidisciplinary research. This was not always easy, but I have learned a lot from this in the process and I like to believe that this will help me a lot in the future. You were also able to keep me motivated by always being excited whenever I would show data of evolving fluorescence after electron beam irradiation, something most readers of these acknowledgements will never understand (but I do). Besides that you've also taught me a lot about scientific writing and (of course) journal keeping. I wish you the best of luck with your future endeavors. Next I would like to thank my second promotor Kees Hagen. Although you were not involved from the beginning, your help was enormous for the progress of the project. To me you always seemed to not only care about the work a PhD-student produces, but also to care about the student personally. This made sure that the project meetings were for 50% about the project and the rest about anything else. I really enjoyed that and I think this a great trait to have as a promotor.

This PhD was impossible without all the help of the technical staff. Thank you Ruud and Joep for the mechanical design and building of the setup in chapter 5. Thank you Dustin, for always quickly repairing the electron microscope whenever it broke. I'll never forget how you quickly fixed a broken detector in one of my last months as a PhD-student. Also thank you to Carel for providing the alumina coating of the ITO slides. I wish you the best of luck at Quantware.

None of this was possible without the help of my colleagues in the Microscopy Instrumentation and Techniques group. I'd like to specifically thank Aditi for getting me started and the discussions we often had about research or life in general. You laid the foundations for the research of this thesis and I will always look up to you als my PhD-elder. You were also essential whenever focusing of the expensive nanometre-resolution electron microscope was required. Thank you to Ryan for all the fruitful discussions, the many hours spent on 'figure time' in the last year and, of course, for the participation in creating the timeless masterpiece 'pre-exposure

magic'. A lot of the work done in this thesis would not have been possible without the help of Mathijs. When discussing anything you were always able to quickly understand the problem at hand and come up with suggestions to solve it. Based on this, I'm confident you'll be a rising star at ASML in no time. Finally, I would like to thank all the other colleagues for all the nice times during the (many) coffee breaks and borrels. In time many of the professional relationships grew to friendships I hope to never lose. I wish all you the best of luck with your life, research and/or next steps in your career.

Thank you for all the friends and teammates I've made along the way who were able to distract me from my research. Especially a big thank you to Annika for helping with designing the front page of this thesis. I would also like to thank Jan-Paul and Christian for being by my side for almost my entire life.

I'm very grateful to my family and my in-laws, who were always a great support by either distracting me from the PhD process or to vent about it. Finally, I want to thank Jolien for her continuing support, great cooking, entertainment and care. While you're sometimes plagued by your own insecurities, I want to take this opportunity to set this in ink and share with the world that you're a truly great person who takes great care of anyone who is important to you. With all your support you've made the PhD a breeze. Thank you.

-Yoram Vos 2022

Curriculum Vitæ

Yoram VOS

01-02-1994	Born in Rotterdam, The Netherlands.

Education

2006–2012	VWO Sint-Laurenscollege, Rotterdam
2012–2015	Bachelor in Applied Physics Delft University of Technology
2015–2018	Master in Applied Physics Delft University of Technology

List of Publications

- Y. Vos, R. Lane, C.J. Peddie, A.H.G. Wolters, J.P. Hoogenboom, *Retarding field integrated fluorescence and electron microscope*, Microscopy and Microanalysis **27(1)**, 109-120 (2020) (Chapter 2 of this dissertation).

- R. Lane, Y. Vos, A.H.G. Wolterse, L. van Kessel, S.E. Chen, N. Liv, J. Klumperman, B.N.G. Giepmans, J.P. Hoogenboom, *Optimization of negative stage bias potential for faster imaging in large-scale electron microscopy*, Journal of Structural Biology: X **5** (2021).

- C.S. Smith, J.A. Slotman, L. Schermelleh, N. Chakrova, S. Hari, Y. Vos, C.W. Hagen, M. Müller, A.B. Houtsmuller, J.P. Hoogenboom, S. Stallinga, *Structured illumination microscopy with noise-controlled image reconstructions*, Nature methods **18(7)**, 821-828 (2021).

- S. Hari, J.A. Slotman, Y. Vos, C. Floris, W.A. van Cappellen, C.W. Hagen, S. Stallinga, A.B. Houtsmuller, J.P. Hoogenboom, *Electron-beam patterned calibration structures for structured illumination microscopy*, submitted.

- Y. Vos, M.W.H. Garming, C.W. Hagen, J. Hernando, J.P. Hoogenboom, *Fluorescence visualization and manipulation of transient, reversible electron-molecule interactions during electron beam irradiation*, In preparation (Chapter 3 of this dissertation).

- **(RETRACTED)** S. Gazibegovic, D. Car, H. Zhang, S.C. Balk, J.A. Logan, M.W.A. de Moor, M.C. Cassidy, R. Schmits, D. Xi, G. Wang, P. Krogstrup, R.L.M. Op het Veld, K. Zuo, Y. Vos, J. Shen, D. Bouman, B. Shojaei, D. Pennachio, J.S. Lee, P.J. van Veldhoven, S. Koelling, M.A. Verheijen, L.P. Kouwenhoven, C.J. Palmstrøm, E.P.A.M. Bakkers, *Epitaxy of advanced nanowire quantum devices*, Nature **548(7668)**, 434-438 (2017) .

Bibliography

[1] Ludwig Reimer. *Scanning electron microscopy: physics of image formation and microanalysis*. Vol. 45. Springer, 2013.

[2] Pascal de Boer, Jacob P Hoogenboom, and Ben NG Giepmans. "Correlated light and electron microscopy: ultrastructure lights up!" In: *Nature methods* 12.6 (2015), p. 503.

[3] Kristina D. Micheva and Stephen J. Smith. "Array tomography: a new tool for imaging the molecular architecture and ultrastructure of neural circuits". In: *Neuron* 55.1 (2007), pp. 25–36.

[4] Forrest Collman et al. "Mapping synapses by conjugate light-electron array tomography". In: *Journal of Neuroscience* 35.14 (2015), pp. 5792–5807.

[5] Yusuke Hirabayashi, Juan Carlos Tapia, and Franck Polleux. "Correlated Light-Serial Scanning Electron Microscopy (CoLSSEM) for ultrastructural visualization of single neurons in vivo". In: *Scientific reports* 8.1 (2018), pp. 1–10.

[6] Matthew RG Russell et al. "3D correlative light and electron microscopy of cultured cells using serial blockface scanning electron microscopy". In: *Journal of Cell Science* 130.1 (2017), pp. 278–291.

[7] Yury S Bykov et al. "Correlative light and electron microscopy methods for the study of virus–cell interactions". In: *FEBS letters* 590.13 (2016), pp. 1877–1895.

[8] Job Fermie et al. "Single organelle dynamics linked to 3D structure by correlative live-cell imaging and 3D electron microscopy". In: *Traffic* 19.5 (2018), pp. 354–369.

[9] Matthia A Karreman et al. "Intravital correlative microscopy: imaging life at the nanoscale". In: *Trends in cell biology* 26.11 (2016), pp. 848–863.

[10] Frank Jan Timmermans and Cornelis Otto. "Contributed review: review of integrated correlative light and electron microscopy". In: *Review of Scientific Instruments* 86.1 (2015), p. 011501.

[11] Nalan Liv et al. "Simultaneous correlative scanning electron and high-NA fluorescence microscopy". In: *PloS one* 8.2 (2013), e55707.

[12] Martijn T Haring et al. "Automated sub-5 nm image registration in integrated correlative fluorescence and electron microscopy using cathodoluminescence pointers". In: *Scientific reports* 7 (2017), p. 43621.

[13] Mats GL Gustafsson. "Surpassing the lateral resolution limit by a factor of two using structured illumination microscopy". In: *Journal of microscopy* 198.2 (2000), pp. 82–87.

[14] Carlas S Smith et al. “Structured illumination microscopy with noise-controlled image reconstructions”. In: *Nature methods* 18.7 (2021), pp. 821–828.

[15] Thomas A Klar and Stefan W Hell. “Subdiffraction resolution in far-field fluorescence microscopy”. In: *Optics letters* 24.14 (1999), pp. 954–956.

[16] Eric Betzig et al. “Imaging intracellular fluorescent proteins at nanometer resolution”. In: *Science* 313.5793 (2006), pp. 1642–1645.

[17] Michael J Rust, Mark Bates, and Xiaowei Zhuang. “Sub-diffraction-limit imaging by stochastic optical reconstruction microscopy (STORM)”. In: *Nature methods* 3.10 (2006), p. 793.

[18] Russell E Thompson, Daniel R Larson, and Watt W Webb. “Precise nanometer localization analysis for individual fluorescent probes”. In: *Biophysical journal* 82.5 (2002), pp. 2775–2783.

[19] Meghan Hauser et al. “Correlative super-resolution microscopy: new dimensions and new opportunities”. In: *Chemical reviews* 117.11 (2017), pp. 7428–7456.

[20] Sergej Masich et al. “A procedure to deposit fiducial markers on vitreous cryo-sections for cellular tomography”. In: *Journal of structural biology* 156.3 (2006), pp. 461–468.

[21] Benjamin G. Kopek et al. “Correlative 3D superresolution fluorescence and electron microscopy reveal the relationship of mitochondrial nucleoids to membranes”. In: *Proc. Natl. Acad. Sci. U. S. A* 109.16 (2012), pp. 6136–6141.

[22] Wanda Kukulski et al. “Precise, correlated fluorescence microscopy and electron tomography of lowicryl sections using fluorescent fiducial markers”. In: *Methods in cell biology* 111 (2012), pp. 235–257.

[23] Kem A Sochacki et al. “Correlative super-resolution fluorescence and metal-replica transmission electron microscopy”. In: *Nature methods* 11.3 (2014), pp. 305–308.

[24] Pascale Schellenberger et al. “High-precision correlative fluorescence and electron cryo microscopy using two independent alignment markers”. In: *Ultramicroscopy* 143 (2014), pp. 41–51.

[25] Martin Schorb and John AG Briggs. “Correlated cryo-fluorescence and cryo-electron microscopy with high spatial precision and improved sensitivity”. In: *Ultramicroscopy* 143 (2014), pp. 24–32.

[26] Jantina Fokkema et al. “Fluorescently labelled silica coated gold nanoparticles as fiducial markers for correlative light and electron microscopy”. In: *Scientific reports* 8.1 (2018), pp. 1–10.

[27] Th Basché, S Kummer, and Ch Bräuchle. “Direct spectroscopic observation of quantum jumps of a single molecule”. In: *Nature* 373.6510 (1995), pp. 132–134.

[28] Tom Vosch et al. “Probing Förster type energy pathways in a first generation rigid dendrimer bearing two perylene imide chromophores”. In: *The Journal of Physical Chemistry A* 107.36 (2003), pp. 6920–6931.

[29] Rob Zondervan et al. "Photoblinking of rhodamine 6G in poly (vinyl alcohol): Radical dark state formed through the triplet". In: *The Journal of Physical Chemistry A* 107.35 (2003), pp. 6770–6776.

[30] Ivan Rasnik, Sean A McKinney, and Taekjip Ha. "Nonblinking and long-lasting single-molecule fluorescence imaging". In: *Nature methods* 3.11 (2006), pp. 891–893.

[31] Jan Vogelsang et al. "A reducing and oxidizing system minimizes photobleaching and blinking of fluorescent dyes". In: *Angewandte Chemie International Edition* 47.29 (2008), pp. 5465–5469.

[32] Jan Vogelsang et al. "Controlling the fluorescence of ordinary oxazine dyes for single-molecule switching and superresolution microscopy". In: *Proceedings of the National Academy of Sciences* 106.20 (2009), pp. 8107–8112.

[33] Christopher J. Peddie et al. "Correlative super-resolution fluorescence and electron microscopy using conventional fluorescent proteins in vacuo". In: *J. Struct. Biol.* 199.2 (2017), pp. 120–131.

[34] Sajjad Mohammadian et al. "Integrated super resolution fluorescence microscopy and transmission electron microscopy". In: *Ultramicroscopy* 215 (2020), p. 113007.

[35] Nils Gustafsson et al. "Fast live-cell conventional fluorophore nanoscopy with ImageJ through super-resolution radial fluctuations". In: *Nature communications* 7.1 (2016), pp. 1–9.

[36] Dorothea Pinotsi et al. "An easy path for correlative electron and Super-Resolution Light Microscopy". In: *Sci. Rep.* 9.1 (2019), pp. 1–9.

[37] Richard J Marsh et al. "Artifact-free high-density localization microscopy analysis". In: *Nature methods* 15.9 (2018), pp. 689–692.

[38] RI Koning et al. "Integrated light and electron microscopy". In: *Correlative Imaging: Focusing on the Future* (2019), pp. 119–135.

[39] Yoram Vos et al. "Retarding field integrated fluorescence and electron microscope". In: *Microscopy and Microanalysis* 27.1 (2021), pp. 109–120.

[40] Aditi Srinivasa Raja. "Electron Behaviour in Insulators Probed by Fluorescence". In: (Manuscript in preparation). ImPhys, Delft University of Technology.

[41] Aditi Srinivasa Raja et al. "Electron-Beam Induced Luminescence and Bleaching in Polymer Resins and Embedded Biomaterial". In: *Macromolecular bioscience* (2021), p. 2100192.

[42] Christopher R Arumainayagam et al. "Low-energy electron-induced reactions in condensed matter". In: *Surface Science Reports* 65.1 (2010), pp. 1–44.

[43] John H Moore et al. "Fundamentals of interactions of electrons with molecules". In: *Nanofabrication using focused ion and electron beams: Principles and applications, ed. P. Russell, I. Utke and S. Moshkalev, Oxford University Press, New York* (2012), p. 184.

[44] Willem F Van Dorp. "Theory: electron-induced chemistry". In: *Frontiers of Nanoscience*. Vol. 11. Elsevier, 2016, pp. 115–133.

[45] Alexandra V. Agronskaia et al. "Integrated fluorescence and transmission electron microscopy". In: *J. Struct. Biol.* 164.2 (2008), pp. 183–189.

[46] Toshio Ando et al. "The 2018 correlative microscopy techniques roadmap". In: *J. Phys. D: Appl. Phys.* 51.44 (2018), p. 443001.

[47] Yasunori Nawa et al. "Multi-Color Imaging of Fluorescent Nanodiamonds in Living HeLa Cells Using Direct Electron-Beam Excitation". In: *ChemPhysChem* 15.4 (2014), pp. 721–726.

[48] Connor G. Bischak et al. "Cathodoluminescence-activated nanoimaging: noninvasive near-field optical microscopy in an electron microscope". In: *Nano Lett.* 15.5 (2015), pp. 3383–3390.

[49] Kuniaki Nagayama et al. "Cathodoluminescence and electron-induced fluorescence enhancement of enhanced green fluorescent protein". In: *J. Phys. Chem. B* 120.6 (2016), pp. 1169–1174.

[50] Haifeng Yuan et al. "Degradation of methylammonium lead iodide perovskite structures through light and electron beam driven ion migration". In: *J. Phys. Chem. Lett.* 7.3 (2016), pp. 561–566.

[51] Angela C. Narváez et al. "Confocal filtering in cathodoluminescence microscopy of nanostructures". In: *Appl. Phys. Lett.* 104.25 (2014), p. 251121.

[52] Robert J. Moerland et al. "Time-resolved cathodoluminescence microscopy with sub-nanosecond beam blanking for direct evaluation of the local density of states". In: *Opt. Express* 24.21 (2016), pp. 24760–24772.

[53] Mathijs W.H. Garming et al. "Nanoparticle discrimination based on wavelength and lifetime-multiplexed cathodoluminescence microscopy". In: *Nanoscale* 9.34 (2017), pp. 12727–12734.

[54] Nalan Liv et al. "Electron microscopy of living cells during in situ fluorescence microscopy". In: *ACS Nano* 10.1 (2016), pp. 265–273.

[55] Ilona Müllerová and Luděk Frank. "Use of cathode lens in scanning electron microscope for low voltage applications". In: *Microchim. Acta* 114.1 (1994), pp. 389–396.

[56] Faycal Boughorbel. *Generation of depth map for an image*. US Patent 8,340,422. 2012.

[57] Michiel De Goede et al. "3D multi-energy deconvolution electron microscopy". In: *Nanoscale* 9.2 (2017), pp. 684–689.

[58] Keisuke Ohta et al. "Beam deceleration for block-face scanning electron microscopy of embedded biological tissue". In: *Micron* 43.5 (2012), pp. 612–620.

[59] James C Bouwer et al. "Deceleration of probe beam by stage bias potential improves resolution of serial block-face scanning electron microscopic images". In: *Advanced structural and chemical imaging* 2.1 (2017), p. 11.

[60] Shigeki Watanabe et al. “Protein localization in electron micrographs using fluorescence nanoscopy”. In: *Nat. Methods* 8.1 (2011), p. 80.

[61] Christopher J. Peddie et al. “Correlative and integrated light and electron microscopy of in-resin GFP fluorescence, used to localise diacylglycerol in mammalian cells”. In: *Ultramicroscopy* 143 (2014), pp. 3–14.

[62] Matthia A. Karreman et al. “Discovery of a new RNA-containing nuclear structure in UVC-induced apoptotic cells by integrated laser electron microscopy”. In: *Biol. Cell* 101.5 (2009), pp. 287–299.

[63] Matthia A. Karreman et al. “Optimizing immuno-labeling for correlative fluorescence and electron microscopy on a single specimen”. In: *J. Struct. Biol.* 180.2 (2012), pp. 382–386.

[64] Hyeok Moo Lee et al. “Fabrication of luminescent nanoarchitectures by electron irradiation of polystyrene”. In: *Adv. Mater. (Weinheim, Ger.)* 20.11 (2008), pp. 2094–2098.

[65] David B Williams and C Barry Carter. “The transmission electron microscope”. In: *Transmission electron microscopy*. Springer, 1996, pp. 3–17.

[66] Meltem Sezen et al. “An investigation on focused electron/ion beam induced degradation mechanisms of conjugated polymers”. In: *Phys. Chem. Chem. Phys.* 13.45 (2011), pp. 20235–20240.

[67] Jiri George Drobny. *Radiation technology for polymers*. CRC press, 2010.

[68] Marijke Scotuzzi et al. “Multi-color electron microscopy by element-guided identification of cells, organelles and molecules”. In: *Scientific reports* 7.1 (2017), pp. 1–8.

[69] A. Sakic et al. “Solid-state backscattered-electron detector for sub-keV imaging in scanning electron microscopy”. In: *Proceedings ICT. Open: Micro Technology and Micro Devices SAFE 2011, Veldhoven, 14-15 Nov. 2011, 1-4* (2011).

[70] Christopher J. Peddie et al. “Integrated light and scanning electron microscopy of GFP-expressing cells”. In: *Methods Cell Biol.* Vol. 124. Elsevier, 2014, pp. 363–389.

[71] Q. He et al. “Biological serial block face scanning electron microscopy at improved z-resolution based on Monte Carlo model”. In: *Sci. Rep.* 8.1 (2018), pp. 1–13.

[72] Helma Pluk et al. “Advantages of indium–tin oxide-coated glass slides in correlative scanning electron microscopy applications of uncoated cultured cells”. In: *J. Microsc. (Oxford, U. K.)* 233.3 (2009), pp. 353–363.

[73] M Pl Seah and WA Dench. “Quantitative electron spectroscopy of surfaces: A standard data base for electron inelastic mean free paths in solids”. In: *Surface and interface analysis* 1.1 (1979), pp. 2–11.

[74] RM Tromp and MC Reuter. “Imaging with a low-energy electron microscope”. In: *Ultramicroscopy* 50.2 (1993), pp. 171–178.

[75] Ernst Bauer. *Surface microscopy with low energy electrons*. Vol. 23. Springer, 2014.

[76] I Müllerová and L Frank. "Very low energy microscopy in commercial SEMs". In: *Scanning* 15.4 (1993), pp. 193–201.

[77] Luděk Frank et al. "Very low energy scanning electron microscopy". In: *Nucl. Instrum. Methods Phys. Res., Sect. A* 645.1 (2011), pp. 46–54.

[78] Irene Wacker and R.R. Schroeder. "Array tomography". In: *J. Microsc. (Oxford, U. K.)* 252.2 (2013), pp. 93–99.

[79] Ryan Lane et al. "Optimization of negative stage bias potential for faster imaging in large-scale electron microscopy". In: *Journal of structural biology: X* 5 (2021), p. 100046.

[80] Oddur Ingólfsson. *Low-Energy Electrons: Fundamentals and Applications*. CRC Press, 2019.

[81] Alberto Bartesaghi et al. "Structure of β-galactosidase at 3.2-Å resolution obtained by cryo-electron microscopy". In: *Proceedings of the National Academy of Sciences* 111.32 (2014), pp. 11709–11714.

[82] Yifan Cheng et al. "A primer to single-particle cryo-electron microscopy". In: *Cell* 161.3 (2015), pp. 438–449.

[83] Takahiro Kozawa and Seiichi Tagawa. "Radiation chemistry in chemically amplified resists". In: *Japanese Journal of Applied Physics* 49.3R (2010), p. 030001.

[84] Justin Torok et al. "Secondary electrons in EUV lithography". In: *Journal of Photopolymer Science and Technology* 26.5 (2013), pp. 625–634.

[85] A Thete et al. "Low-energy electron (0-100eV) interaction with resists using LEEM". In: *Extreme Ultraviolet (EUV) Lithography VI*. Vol. 9422. International Society for Optics and Photonics. 2015, 94220A.

[86] Ivan Pollentier et al. "Unraveling the role of secondary electrons upon their interaction with photoresist during EUV exposure". In: *International Conference on Extreme Ultraviolet Lithography 2017*. Vol. 10450. International Society for Optics and Photonics. 2017, 104500H.

[87] B Boudaıffa et al. "Cross sections for low-energy (10–50 eV) electron damage to DNA". In: *Radiation research* 157.3 (2002), pp. 227–234.

[88] Frank Würthner. "Perylene bisimide dyes as versatile building blocks for functional supramolecular architectures". In: *Chemical communications* 14 (2004), pp. 1564–1579.

[89] Frank Wurthner and Armin Sautter. "Highly fluorescent and electroactive molecular squares containing perylene bisimide ligands". In: *Chemical Communications* 6 (2000), pp. 445–446.

[90] Rafael S Sanchez et al. "Light-and redox-controlled fluorescent switch based on a perylenediimide–dithienylethene dyad". In: *The Journal of Physical Chemistry C* 116.12 (2012), pp. 7164–7172.

[91] Jacob P Hoogenboom et al. “Power-law-distributed dark states are the main pathway for photobleaching of single organic molecules”. In: *Physical review letters* 95.9 (2005), p. 097401.

[92] Masaaki Mitsui, Aki Unno, and Syun Azechi. “Understanding photoinduced charge transfer dynamics of single perylenediimide dyes in a polymer matrix by bin-time dependence of their fluorescence blinking statistics”. In: *The Journal of Physical Chemistry C* 120.28 (2016), pp. 15070–15081.

[93] R Boschi, JN Murrell, and W Schmidt. “Photoelectron spectra of polycyclic aromatic hydrocarbons”. In: *Faraday Discussions of the Chemical Society* 54 (1972), pp. 116–126.

[94] R Boschi, E Clar, and W Schmidt. “Photoelectron spectra of polynuclear aromatics. III. The effect of nonplanarity in sterically overcrowded aromatic hydrocarbons”. In: *The Journal of Chemical Physics* 60.11 (1974), pp. 4406–4418.

[95] Michael S Deleuze. “Valence one-electron and shake-up ionization bands of polycyclic aromatic hydrocarbons. II. Azulene, phenanthrene, pyrene, chrysene, triphenylene, and perylene”. In: *The Journal of chemical physics* 116.16 (2002), pp. 7012–7026.

[96] Seiji Tobita et al. “Polycyclic aromatic hydrocarbons: Negative ion formation following low energy (0–15 eV) electron impact”. In: *Chemical physics* 161.3 (1992), pp. 501–508.

[97] Hai-Xian Gong et al. “Photoexcited perylene diimide radical anions for the reduction of aryl halides: a bay-substituent effect”. In: *Organic Chemistry Frontiers* 5.15 (2018), pp. 2296–2302.

[98] Almaz S Jalilov et al. “Perylene diimide as a precise graphene-like superoxide dismutase mimetic”. In: *ACS nano* 11.2 (2017), pp. 2024–2032.

[99] Sebastian van de Linde et al. “Photoinduced formation of reversible dye radicals and their impact on super-resolution imaging”. In: *Photochemical & Photobiological Sciences* 10.4 (2011), pp. 499–506.

[100] Aditi Srinivasa Raja. In: (Manuscript in preparation). ImPhys, Delft University of Technology.

[101] Jan Vogelsang et al. “Make them blink: Probes for super-resolution microscopy”. In: *ChemPhysChem* 11.12 (2010), pp. 2475–2490.

[102] Dylan T Burnette et al. “Bleaching/blinking assisted localization microscopy for superresolution imaging using standard fluorescent molecules”. In: *Proceedings of the National Academy of Sciences* 108.52 (2011), pp. 21081–21086.

[103] Thomas Dertinger et al. “Fast, background-free, 3D super-resolution optical fluctuation imaging (SOFI)”. In: *Proceedings of the National Academy of Sciences* 106.52 (2009), pp. 22287–22292.

[104] Susan Cox et al. “Bayesian localization microscopy reveals nanoscale podosome dynamics”. In: *Nature methods* 9.2 (2012), pp. 195–200.

[105] Martin Ovesnỳ et al. “ThunderSTORM: a comprehensive ImageJ plug-in for PALM and STORM data analysis and super-resolution imaging”. In: *Bioinformatics* 30.16 (2014), pp. 2389–2390.

[106] Paul D Simonson, Eli Rothenberg, and Paul R Selvin. “Single-molecule-based super-resolution images in the presence of multiple fluorophores”. In: *Nano letters* 11.11 (2011), pp. 5090–5096.

[107] JA Veerman et al. “Time-varying triplet state lifetimes of single molecules”. In: *Physical review letters* 83.11 (1999), p. 2155.

[108] Fabian Köhn et al. “Parameters influencing the on-and off-times in the fluorescence intensity traces of single cyanine dye molecules”. In: *The Journal of Physical Chemistry A* 106.19 (2002), pp. 4808–4814.

[109] Jordi Hernando et al. “Excitonic behavior of rhodamine dimers: a single-molecule study”. In: *The Journal of Physical Chemistry A* 107.1 (2003), pp. 43–52.

[110] Ruchuan Liu et al. “Single-molecule spectroscopy of intramolecular electron transfer in donor-bridge-acceptor systems”. In: *The Journal of Physical Chemistry A* 107.34 (2003), pp. 6522–6526.

[111] Matthias Haase et al. “Exponential and power-law kinetics in single-molecule fluorescence intermittency”. In: *The Journal of Physical Chemistry B* 108.29 (2004), pp. 10445–10450.

[112] Philip Tinnefeld et al. “Higher-Excited-State Photophysical Pathways in Multichromophoric Systems Revealed by Single-Molecule Fluorescence Spectroscopy”. In: *ChemPhysChem* 5.11 (2004), pp. 1786–1790.

[113] Jörg Schuster, Frank Cichos, and Christian von Borczyskowski. “Influence of self-trapped states on the fluorescence intermittency of single molecules”. In: *Applied Physics Letters* 87.5 (2005), p. 051915.

[114] A Nicolet et al. “Intermolecular intersystem crossing in single-molecule spectroscopy: Terrylene in anthracene crystal”. In: *The Journal of chemical physics* 124.16 (2006), p. 164711.

[115] Jacob P Hoogenboom et al. “Power-Law Blinking in the Fluorescence of Single Organic Molecules”. In: *ChemPhysChem* 8.6 (2007), pp. 823–833.

[116] John N Clifford et al. “Fluorescence of single molecules in polymer films: Sensitivity of blinking to local environment”. In: *The Journal of Physical Chemistry B* 111.25 (2007), pp. 6987–6991.

[117] John Turton Randall and Maurice Hugh Frederick Wilkins. “Phosphorescence and electron traps II. The interpretation of long-period phosphorescence”. In: *Proceedings of the Royal Society of London. Series A. Mathematical and Physical Sciences* 184.999 (1945), pp. 390–407.

[118] Christiaan N Hulleman et al. “Polarized stimulated-emission depletion and dark-state lifetime at vacuum and cryogenic temperature conditions”. In: *Physical Review A* 104.6 (2021), p. 063516.

[119] VV Afanas' Ev et al. "Influence of Al2O3 crystallization on band offsets at interfaces with Si and TiNx". In: *Applied Physics Letters* 99.7 (2011), p. 072103.

[120] Jacques Cazaux. "Charging in scanning electron microscopy "from inside and outside"". In: *Scanning: The Journal of Scanning Microscopies* 26.4 (2004), pp. 181–203.

[121] Oliver A Dicks et al. "The origin of negative charging in amorphous Al2O3 films: The role of native defects". In: *Nanotechnology* 30.20 (2019), p. 205201.

[122] R Bosveld. "Developing a reflection-based detection method for charging in a SEM". Bachelor Thesis. Delft University of Technology, 2019.

[123] A Maasland. "Optimization of a reflection-based detection method for charging in a SEM". Bachelor Thesis. Delft University of Technology, 2019.

[124] A Thete et al. "Charge catastrophe and dielectric breakdown during exposure of organic thin films to low-energy electron radiation". In: *Physical Review Letters* 119.26 (2017), p. 266803.